Modelling and Control of Novel Small-Scale Induction Generator Concepts

Zhijia Wang

A thesis submitted in fulfilment of the requirements for the degree of Doctor of Philosophy in Electrical and Electronic Engineering, The University of Auckland, 2020.

Abstract

Small scale single-phase renewable distributed generation system is expected to play an important role in meeting electricity demand. Because, such systems can provide low-cost electricity for homes, businesses and farms in remote areas without burning fossil fuels. The standard 3-phase squirrel cage induction machine (SCIM) is widely used in these systems due to its low unit cost, ruggedness and virtually free maintenance. However, in order to generate single-phase electricity, the standard 3-phase SCIM needs to operate in the single-phase mode. Thus, various techniques of using 3-phase SCIMs for single-phase electricity generation have been widely explored.

Among these techniques, SCIM operated in the two series-connected and one-isolated (TSCAOI) winding arrangement, which provides well-regulated output voltage and frequency with a low cost, has drawn attention. There are, however, three major unsolved difficulties associated with the TSCAOI configured generator. This thesis therefore proposes the following solutions to these three difficulties, contributing to the ongoing research on the TSCAOI configured generator.

The first difficulty is that the TSCAOI configured generator lacks a unified equivalent circuit model, through which the steady-state characteristics of this particular generator can be comprehensively investigated. Therefore, this thesis proposes the steady-state equivalent circuit models of the standalone TSCAOI configured generator, using the method of symmetrical components. Through the investigation of the proposed models, this thesis identifies the impacts of system parameters on its load and excitation characteristics, as well as on its level of unbalanced operation. Simulated and experimental results for a prototype generator are presented to demonstrate both the effectiveness and usefulness of the equivalent circuit models.

The second difficulty is that the integration of the TSCAOI configured generator into a single-phase grid is yet to be proposed. Therefore, after investigating the behaviour of the grid-connected TSCAOI generator, this thesis proposes a control scheme to integrate the TSCAOI configured generators into the single-phase grid. The proposed control scheme can regulate the generator to provide electricity to the grid at near-unity power factor, while, minimising the unbalanced operation of the generator. The feasibility of the concept is demonstrated using both simulations and experiments of a prototype generator.

The last difficulty is that the balanced operation condition and fast dynamic response are difficult to achieve for the TSCAOI configured generator, because of its inherent limited control degrees of freedom. In order to realize the balanced operation and fast dynamic response, this thesis proposes a topological modification to the TSCAOI winding configuration. The modified winding configuration, named NPC-TSCAOI (Neutral-Point-Connected TSCAOI) configuration, connects the neutral-point of the two series-connected winding in the TSCAOI winding configuration to an additional converter leg, thus adding an additional control degree of freedom. This additional control degree of freedom enables the stator flux control, which can realize both the output voltage and frequency regulation under balanced operating condition. The feasibility of this concept is also verified using both simulations and experiments of a prototype generator.

Acknowledgements

Firstly, I would like to express my deepest gratitude to my supervisor Prof. Udaya Madawala for his academic guidance and consistent encouragement. Prof. Udaya Madawala set a great example of an excellent researcher for me and helped me develop critical and independent thinking skills. I also would like to thank him for the many hours he has put in helping me edit conference papers, journal papers and chapters of this thesis.

I would like to thank Dr. Duleepa Thrimawithana, Prof. Tian-Hua Liu and Prof. Mahinda Vilathgamuwa. They provided me many insightful comments and constructive suggestions during my PhD study.

I thank all the members of the department and especially the members of the power electronic group for their friendliness and help over the years.

Finally, I would like to thank my parents Xudong Wang and Lin Ye, and my wife Su Zhang, for their unconditional love and support. I am truly grateful for having such a happy and supportive family.

Contents

List of Figures

List of Tables

Symbols and Acronyms

Symbols

$\tilde{I}_g$	Actual grid current
$\tilde{I}_{s+}$, $\tilde{I}_{s-}$	Phasor variables of positive and negative sequence symmetrical components of stator currents
$\tilde{V}_{s+}$, $\tilde{V}_{s-}$	Phasor variables of positive and negative sequence symmetrical components of stator voltages
$\tilde{V}_{se}$, $\tilde{I}_{se}$	Phasor variables of the actual OI winding voltage and current
$\tilde{V}_{se}^{*}$	Final selected excitation voltage reference
$\tilde{V}_{so}'$, $\tilde{I}_{so}'$	Phasor variables of the referred TSC winding voltage and current
$\tilde{X}_{s+}$, $\tilde{X}_{s-}$	Phasor variables of positive and negative sequence symmetrical components
$\tilde{X}_{\alpha}$, $\tilde{X}_{\beta}$	Phasor variables in the α and β axis
$\tilde{\imath}_{r+}$, $\tilde{\imath}_{r-}$	Rotating vectors of the rotor current symmetrical components
$\tilde{\imath}_{s+}$, $\tilde{\imath}_{s-}$	Rotating vectors of the stator current symmetrical components
$\vec{\Psi}_s$	Stator flux vector
C_{comp}	Compensation capacitor
C_{comp}'	Referred compensation capacitor
L_{lr}	Rotor leakage inductance
L_{ls}	Stator leakage inductance
L_m	Magnetizing inductance
N_s	Per stator phase total number of turns
R_{load}'	Referred load resistance
R_r	Rotor resistance
R_s	Stator resistance
T_e	Electromagnetic torque
T_{ex}	External torque
Z'	Referred impedance
Z_{eq}	Equivalent impedance
$i_{r\alpha}'$, $i_{r\beta}'$	Referred α and β components of the rotor currents

$i_{\alpha r}$, $i_{\beta r}$	α and β components of the rotor currents
$i_{\alpha s}$, $i_{\beta s}$, i_{0s}	α, β and zero components of stator currents
v_{se} , i_{se}	Actual voltage and current of the OI winding
v_{so} , i_{so}	Actual voltage and current of the TSC winding
v'_{so} , i'_{so}	Referred voltage and current of the TSC winding
$v_{\alpha s}$, $v_{\beta s}$, v_{0s}	α, β and zero components of the stator voltages
θ_{grid}	Grid current phasor angle
$\varphi_{\alpha r}$, $\varphi_{\beta r}$	α and β components of the rotor flux linkages
$\varphi_{\alpha s}$, $\varphi_{\beta s}$ φ_{0s}	α, β and zero components of stator currents
ψ'_r , i'_r	Referred rotor flux linkage and rotor current
ω_{grid}	Grid angular frequency
ω_r	Electrical angular frequency of the rotor
ω_r	Electrical angular frequency of the rotor
ω_s	Synchronous angular frequency
ω_{slip}	Slip angular velocity
s	slip
J	Rotor inertia
P	Number of poles
p	differential operator d/dt
$\boldsymbol{S}$	Transformation matrix
γ	delay angle
σ	leakage factor
ϕ	electrical angle with respect to the magnetic axis of the phase 'a' winding

Acronyms

A/D	Analog to Digital
AC	Alternative current
CUF	Current unbalance factor
DC	Direct current
DFC	Direct flux control
DFIG	Doubly fed induction generator
ELC	Electronic load controller
ESS	Energy-storage-system
FEM	Finite element method
FIT	Feed-in tariffs
FOC	Field oriented control
HREG	Hybrid renewable energy generation
MMF	Magneto-motive force
NPC	Neutral-Point-Connected
OI	One-Isolated
P.F.	Power factor
PI	Proportional–integral
PLL	Phase-Locked loop
PMSG	Permanent magnet synchronous generator
PV	Photovoltaic
PWM	Pulse width modulation
RECS	Renewable energy conversion systems
RMS	Root mean square
SCIG	Squirrel cage induction generator
SCIM	Squirrel cage induction machine
SEIG	Self-excited induction generator
SG	Synchronous generator
T&D	Transmission and Distribution
TSC	Two-Series-Connected
TSCAOI	Two-Series Connected and One-Isolated
VAR	Volt-Ampere reactive
VSC	Voltage source converter

VSD	Variable-Speed drive
VSI	Voltage source converter
VUF	Voltage unbalance factor
WECS	Wind energy conversion system
WRSG	Wound rotor synchronous generator

Chapter 1

Introduction

1.1. Background

Sustainable development is a major challenge at present. Every new unit of economic growth is still attained at the expense of depletion of the natural energy resources and degradation of the environment. One of the major reasons for this is the world's heavy reliance on fossil fuels. Fossil fuels are non-renewable energy sources, meaning that there is a finite amount of fossil fuels available and they do not naturally replenish fast enough. In addition, fossil fuels need to be burned to release the stored energy. However, the burning of fossil fuels also releases harmful particles and greenhouse gases into the atmosphere, resulting in adverse environmental effects. At present, for instance, around 91% of the world population live amid unsafe outdoor air pollution, which causes more than 4 million deaths each year [1]. Around 90% of the global greenhouse gases emissions are sourced from the burning of fossil fuels [2].

In order to reduce the reliance on fossil fuels, it has become a consensus among countries of the world to focus more on renewable energy. Unlike non-renewable energy, renewable energy comes from sources that are naturally replenished in a relatively short timeframe. Sources of renewable energy mainly include wind, hydro, solar, geothermal and biomass. Another important advantage is that renewable energy is a clean source of energy. Wind, hydroelectric and solar systems generate electricity without air pollution and greenhouse emissions. Geothermal and biomass systems emit some greenhouse gases, however the emissions are much lower than those of burning fossil fuels.

Unlike the fossil fuels, which heavily relies on the transport lines, renewable energy sources are broadly available and distributed. Distributed generation therefore becomes a promising paradigm for the renewable energy systems. Due to the distributed nature of renewable energy sources, these distributed generation systems are usually small-scale in terms of power rating, thus may not be as efficient as large scale centralised generation systems. However, this disadvantage is offset by the cost reduction of the transmission and distribution grid.

In recent years, renewable distributed generation using small scale generating units of power rating less than 200kW has drawn particular attentions [3, 4]. Because, on one hand, this small scale renewable distributed generating system is quite suitable to provide electricity for homes, businesses and farms in remote areas. On the other hand, the global trend of energy deregulation encourages the development of such systems. More importantly, at present, about 1 billion people still lack access to electricity, and the vast majority of them are living in the rural areas of Africa and Asia-Pacific [5]. The small scale renewable distributed generation system has great potential to help provide basic electricity service to those people who are living without electricity.

The majority of small scale renewable generation systems use electric generators to convert kinetic energy into electrical energy, except the photovoltaic systems. Among these electric generators, squirrel cage induction generators (SCIGs) are the cheapest and most rugged, thus most widely used. In remote and rural areas, the population is sparsely distributed, and the most of electric loads are of single-phase nature. Therefore, single-phase SCIG is preferred over 3-phase SCIG to make the whole system simple and cost-effective. Using single-phase SCIGs means that for a given amount of capital investment, more areas can gain access to electricity.

Single-phase squirrel cage induction machines (SCIMs) can be used for single-phase electricity generation [3, 4], but use of conventional 3-phase SCIMs for single-phase electricity generation is more advantageous over single-phase machines, especially for machines with power ratings above 3kW [5, 6]. This is because 3-phase SCIMs are widely available in the market, and more economical in terms of both size and cost than its single-phase counterparts. Therefore, use of 3-phase squirrel cage induction machines (SCIM) for single-phase electricity generation has been of interest to both academia and industry and consequently been widely explored. However, when a 3-phase SCIM is operated as a single-phase generator, the 3-phase stator currents are generally unbalanced. Therefore, output power degradation is normally inevitable. Furthermore, the adverse effects such as mechanical vibration, poor efficiency, thermal overload and uncontrollable power factor are also concerned [7]. Hence, various phase balancing techniques have been proposed and investigated to mitigate these concerns. In general, all these techniques can be classified into two categories: namely based on passive circuit elements and power electronic converters.

The techniques, which are based on passive circuit elements, have the advantages of low cost, low maintenance and simple configuration. However, these techniques share two common weaknesses. One is the poor output voltage and frequency regulation and the other is the limited

operating range. Conversely, the techniques, which are based on power converters, have better voltage and frequency regulation capabilities and wider operating range but at the expense of higher cost and complicated configurations. In addition, a power conversion stage, comprising either a back-to-back converter or an alternating-current (AC)/direct-current (DC) converter, is often employed on the front-end or back-end of the load, inevitably causing high harmonic distortion.

As an alternative, a new winding configuration, that uses one of the stator phases of a 3-phase SCIM as the excitation winding and the remaining two phases connected in series as the power winding, has been proposed [6-10]. This decoupled winding configuration is named as Two-Series Connected and One Isolated (TSCAOI) and shown in Fig. 1.1. Electricity is generated through the power winding with appropriate excitation. A compensation capacitor is employed to reduce the reactive power requirement of the generator. In contrast to other power converter based techniques, the TSCAOI configured generator also combines the cost advantage of the passive circuit element based techniques, by only using a bi-directional single-phase converter. In addition, it enables direct single-phase electricity generation without using a power conversion stage, thus also having the advantage of low harmonic distortion. However, the study of the TSCAOI configured SCIGs is still not complete and technology gap exists. This thesis intends to address some of these technology gaps.

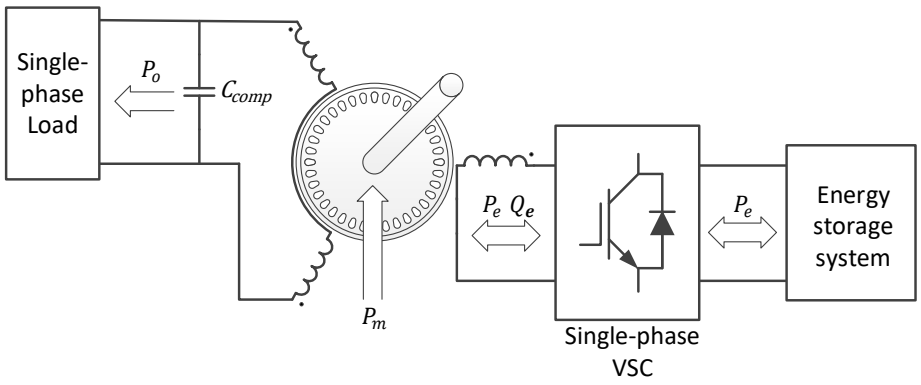

Fig. 1.1 The TSCAOI configuration for 3-phase SCIMs feeding single-phase load

1.2. Research Objectives

A comprehensive review of the TSCAOI configured SCIGs is given in Chapter 2. According to this review, there still exist three major unsolved difficulties, associated with the TSCAOI configured generator. This thesis will be expended by solving these difficulties.

Firstly, the thesis completes the steady-state analysis of the standalone TSCAOI configured generator, by proposing a unified equivalent circuit. Furthermore, the thesis demonstrates that the steady-state load and excitation characteristics of this generator can be effectively investigated through the proposed equivalent circuit.

Secondly, the thesis investigates the behaviour of the grid-connected TSCAOI generator, and proposes a control scheme for integrating the TSCAOI configured generators into the single-phase distributed power system. The thesis demonstrates the feasibility of the proposed concept, using simulation and experimental results of a prototype generator.

Finally, in order to achieve the balanced operating condition and further improve the dynamic response, the thesis proposes a topological modification to the TSCAOI configuration and a novel direct-flux-controlled (DFC) scheme to control the generator configured in the modified configuration. The modified configuration is called NPC-TSCAOI (Neutral-Point-Connected TSCAOI) winding configuration. The thesis demonstrates that by employing DFC scheme, the NPC-TSCAOI configured SCIGs can realize balanced operation and fast dynamic response.

1.3. Thesis Organisation

The chapters of this thesis are arranged as follows:

Chapter 2 – Literature Survey. This chapter presents an overview of the most commonly used electric generators, followed by a detailed comparison of their advantages and disadvantages. Based on this comparison, the squirrel cage induction generator (SCIG) is suitable for the low-cost small scale renewable distributed generation systems. Most of the electric loads are of single-phase nature for such generation systems, and regarding the single-phase electricity generation, the 3-phase induction machine has more advantages over its single-phase counterpart. A survey of publications on using 3-phase induction machines for single-phase electricity generation is therefore presented, with the emphasis on the TSCAOI configured generator. Finally, three major unsolved difficulties of the TSCAOI configured generator are identified, and constituting as research objectives of this thesis.

Chapter 3 – A Steady-State Equivalent Circuit Model for Standalone TSCAOI Configured Induction Generators. This chapter proposes a winding function approach to derive a dynamic model of the TSCAOI configured generator. Based on the derived dynamic model, this chapter then presents the steady-state equivalent circuit models of the standalone TSCAOI configured generator, using the method of symmetrical components. In order to

investigate the load and excitation characteristics pertinently, two different equivalent circuit models are obtained by adopting different transformation matrix. Using these two models, this chapter theoretically investigates the steady-state behaviour of the standalone TSCAOI configured generator and determines the impact of system parameters on the load and excitation characteristics, as well as on the level of voltage unbalance.

Chapter 4 – Performance of Standalone TSCAOI Configured Induction Generators. This chapter investigates both the steady-state behaviour and performance of the standalone TSCAOI configured generator through simulations, implementing the proposed mathematical model in MATLAB/Simulink and experimentally using a prototype generator. Both the simulated and experimental results are in good agreement and exhibit the same trend, further indicating that the characteristics of this particular generator can be accurately predicted by the proposed equivalent circuit models.

Chapter 5 – Grid Integration of TSCAOI Configured Generators. This chapter investigates the steady-state behaviour of the grid-connected TSCAOI generator, and proposes a control scheme to integrate the TSCAOI configured generators into the single-phase distributed power system. The proposed control scheme incorporates a look-up table, and enables the electricity generation at near-unity power factor and limits the unbalanced operation of the generator. In addition, this chapter proposes a slip estimation method, which enables speed-sensorless control of the generator, further simplifying the system. Finally, simulation and experimental results for a prototype generator are provided to validate the proposed concept and control scheme.

Chapter 6 – Direct-Flux-Controlled NPC-TSCAOI Configured Generators for Standalone Applications. This chapter proposes a topological modification to the TSCAOI winding configuration to realize balanced operation of the generator. The modified winding configuration, named NPC-TSCAOI (Neutral-Point-Connected TSCAOI) configuration, connects the neutral-point of the two series-connected winding in the TSCAOI winding configuration to an additional converter leg. The operating principles and control scheme of the standalone NPC-TSCAOI configured generator are presented. Finally, simulation and experimental results for a prototype generator are also provided to validate the proposed concept and control scheme.

Chapter 7 – Conclusions. This chapter summarizes the findings of the thesis and briefly discusses directions for future research.

Chapter 2

Literature Survey

2.1. Introduction

The majority of renewable energy conversion systems (RECS) transform kinetic energy into electrical energy, using an electric generator. Different types of generators, such as squirrel cage induction generators (SCIGs), doubly fed induction generator (DFIGs), and synchronous generator (SGs) etc., have been employed in RECSs. They differ from one another with respect to operating principles, characteristics, complexity, performance, cost, etc. and the right choice depends on the energy sources, power rating, the type of load and the operating speed and environment [11, 12].

Therefore, an overview of most commonly used electric generators is firstly presented in this chapter, emphasizing on their advantages and disadvantages. Based on these specific advantages and disadvantages, a detailed generator selection is then conducted for small scale renewable distributed generation systems. The squirrel cage induction generator (SCIG) is finally selected, because it can better fulfil the low cost and high durable demands of the system.

Small scale renewable distributed generation systems are usually classified into two main categories by the type of loads: one for 3-phase electricity generation and the other for single-phase electricity generation. Accordingly, this chapter provides comprehensive reviews of SCIGs, considering these two different loads respectively. The 3-phase SCIGs and self-excited induction generators (SEIGs), for supplying 3-phase loads, are firstly reviewed in this chapter. Afterwards, a detailed literature survey of 3-Phase SCIGs for supplying single-phase loads is presented. In this section, TSCAOI configured 3-phase SCIG is focused, with the emphasis on its unique attributes for single-phase electricity generation. Finally, three major unsolved difficulties of the TSCAOI configured generator are identified, as the research directions of this thesis.

2.2. Overview of Different Electric Generators

A classification of most common electric generators in energy conversion system is illustrated in Fig. 2.1. Depending on their operating principles and structures, these generators are divided in two main groups: induction generators and synchronous generators.

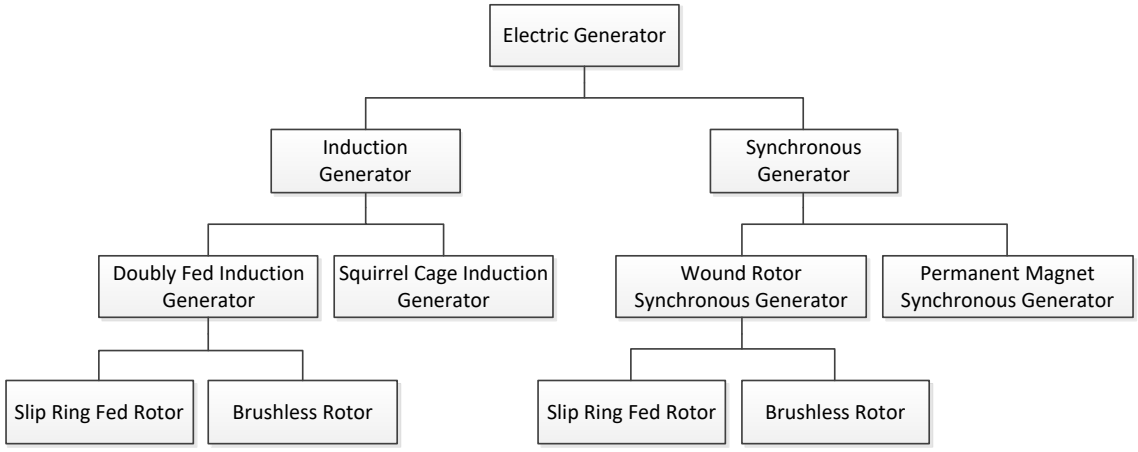

Fig. 2.1 Classification of commonly used electric generators

Both these two groups include generators with wound rotor. The wound rotor induction generator, also named as the doubly fed induction generator (DFIG), is one of the most widely used generators in large scale wind energy conversion system (WECS). The wound rotor synchronous generator (WRSG), with additional control degree of freedom, is also found in many practical applications [13-15]. In general, the wound rotor is fed by slip rings through brushes. However, the additional slip rings and brushes not only make the structure complex but also increase the maintenance cost. In order to reduce the maintenance cost of traditional DFIG and WRSG, brushless wound rotor generator is proposed and widely explored [16-20].

Unlike DFIG and WRSG which are only suitable for medium and large scale power generations, the squirrel cage induction generator (SCIG) and permanent magnet synchronous generator (PMSG) are applicable to almost all types of power generation systems. In addition, from the aspect of rotor structure, the rotor circuits of SCIG are shorted internally and therefore not connected with external circuit. However, in the PMSG, the permanent magnets replace the rotor circuits to generate the rotor magnetic flux.

Table. 2.1 lists the various generators mentioned above and outlines the advantages and disadvantages of each [12, 21-24]. SCIG is widely employed in different kinds of power

generation systems by virtue of its low cost and robust structure. However, it requires additional reactive power, thus reducing the total efficiency of the system. PMSG offers the highest efficiency and power density and is suitable for direct drive power generation. Its major disadvantage is the high cost and demagnetization risk of the permanent magnets. Although DFIG can be equipped with a reduced capacity converter, the high maintenance cost makes it only suitable to medium and large scale generation systems. Similarly, the high initial investment and maintenance cost also restrict the application of WRSG to the medium and large scale generation systems.

Table. 2.1 Advantages and disadvantages of different types of generator:

Generator type	Advantages	Disadvantages
Squirrel Cage Induction Generator (SCIG)	• Low cost • High market share (Almost 70% of the industrial electric machines comes under this category) • Simple design • Rugged in construction and requires minimum maintenance • Higher overload capacity • Excellent damping of torque pulsation • Can operate in almost any environmental conditions including high-temperature, polluted and explosive • Applicable to super-high, high and medium generator environments	• Requires reactive power • Increased power converter cost in large scale generator since the converter must be rated at the full system power rating. • Higher energy losses in power converter • Relatively low efficiency • Limited range of operating speed • Needs Gearbox
Permanent Magnet Synchronous Generator (PMSG)	• Additional reactive power and excitation are not needed since the rotor	• High cost • Less rugged in construction • Relatively low market share

	magnetic flux is provided by permanent magnets • Higher efficiency and power density • Relatively wide operating speed range • Suitable for direct-drive and gear-box is therefore eliminated • Flexibility in design, especially for small and lightweight designs • No need for rotor maintenance • Applicable to super-high, high, medium and low speed generator	• Full-capacity power converter is also needed • Demagnetization risk of the permanent magnet under high temperature and overloading conditions • Rectifier is needed in initial stage of power conversion
Doubly Fed Induction Generator (DFIG)	• Reduced converter cost and losses, power converter rating is typically 25% of system power rating. • Improved system efficiency • Power factor regulation can be implemented at lower cost • Enables decoupled control of active power and reactive power of the generator • Suitable for high power applications	• Not applicable to medium-speed and low-speed generator • Complicated process to manufacture rotor • Need for periodic slip ring maintenance • Susceptible to grid disturbance
Wound Rotor Synchronous Generator (WRSG)	• Applicable for direct drive • Applicable to low speed generator	• High cost and complicated process to manufacture rotor • Low power density

	• Less mechanical wear due to low rotor speed • Allows decoupled control of both active and reactive power of the generator	• Full-capacity power converter is needed • Higher maintenance costs

2.3. Generators applicable to small scale renewable and distributed generation

Almost half a century ago, electric power is mainly generated by large scale centralised generating stations. These generating stations are generally located close to the fuels and far from the end users of power. The generated electricity has to be delivered to the end user through the long transmission and distribution (T&D) grid. This is because the cost of transporting fuel far exceeded the cost of building T&D grid at that time. However, with the rapid expansion of the electricity demand, the cost of building T&D grid also increases rapidly, it even has exceeded the cost of building centralised generating station in many places. Furthermore, more and more power failures were caused by the T&D grid.

In this context, the distributed generation was proposed in the early 1990s [25, 26]. In contrast to the centralised generation, distributed generation employs numerous, but small-scale generating systems to produce electricity close to the end users. Hence, the typical problems caused by the centralised generation, namely the high cost, poor reliability and low efficiency of the T&D grid, can be solved [27, 28]. Besides, the distributed generation, mainly using renewable energy, is more environmentally friendly than the fossil-fuel based centralised generation.

In recent years, renewable distributed generation using small scale generating units of power rating less than 200kW has drawn particular attentions [3, 4]. Because, this small scale renewable distributed generating system is suitable to provide electricity for homes, businesses and farms in remote areas. More importantly, this technology has great potential to help provide basic electricity service to the nearly one billion people who are living without electricity.

The advantages of such systems are listed as below:

- Low initial investment
- Capability to operate in standalone mode for isolated communities
- High feed-in tariffs (FIT)

- Lower impact on the landscape
- Lower noise level

As discussed previously, DFIGs and WRSGs are only suitable for medium and large scale power generations. Therefore, the selection of generators for such small scale distribution generation is confined to PMSGs and SCIGs.

For the PMSG, as mentioned before, it is possible to use a large number of pole pairs to allow the generator to operate at low speed without decreasing the efficiency. Therefore, the gear box and the issues relating to it, such as rising cost and weight, maintenance and noise, can be avoided. Such a generator is also called as a direct-drive generator. However, in order to accommodate a large number of pole pairs, it is inevitable to increase the rotor diameter. For the generator with power rating less than 200kW, the most commonly used radial-flux inner-rotor machine configuration no longer provides sufficient space to accommodate such high number of pole pairs, thus becomes unsuitable for the direct-drive application. Consequently, radial-flux outer-rotor and axial-flux machine configuration which could provide larger rotor diameter with the same machine volume are widely explored in this power range [29-34]. Drawbacks of these two configurations are the higher cost and more complicated manufacture process.

It is also possible to employ a high-speed PMSG with gearbox for such small scale distribution generation. In order to achieve higher power density than its SCIG counterpart, these high-speed PMSGs must be made with high-energy rare-earth magnets. However, expensive prices of rare-earth materials and export restriction on them make the cost of high-speed PMSGs much higher than its SCIG counterpart.

In summary, PMSG is highly desirable for the small scale distribution generation which is not sensitive to prices but pursues high power density and performance. Conversely, the SCIG is more suitable for the low-cost and durable small scale distribution generation and currently dominates the field of small scale distribution generation. Therefore, SCIG is selected to be the generator for the low-cost small scale distribution generation systems proposed in this thesis.

2.4. SCIG based small-scale generation systems

A small scale distribution generation system can be classified into two main categories by the type of loads: one for providing electricity to the 3-phase load and the other for providing electricity to the single-phase load. Therefore, the SCIG employed in such system can also be

classified into two categories accordingly: one is 3-phase SCIG and the other is single-phase SCIG.

2.4.1 **3-Phase SCIG and SEIG**

The principle and operation of grid-connected 3-phase SCIGs are well understood and discussed in detail [35, 36]. When the rotor of an induction machine is driven above synchronous speed by a prime mover, the machine will operate as a generator. The induction machine equivalent circuit model can also be used to investigate the electromechanical characteristics of the machine operating in the generating mode. In contrast to the motoring mode, a negative slip is used since the rotor speed is higher than the synchronous speed. A soft starter and a 3-phase capacitor bank are usually required for limiting the high inrush current during the start-up phase and compensating the reactive power drawn by the generator, respectively.

The 3-phase self-excited induction generator (SEIG), on the other hand, has also remained as a strong candidate for small scale standalone power generation system due to its low-cost and simple operating scheme [37-40]. The self-excitation phenomenon in induction machines, with excitation capacitors connected to stator terminals, has been well known for more than 80 years [41], and various models have been proposed to investigate the steady-state as well as transient characteristics of 3-phase SEIG operating with either a regulated or unregulated prime mover.

The major drawback of the standalone 3-phase SEIG is its poor voltage regulation. That is because the output voltage of the SEIG is governed by the excitation capacitance, the speed of the prime mover and the load impedance. In order to improve the voltage regulation, various techniques, such as switched capacitor bank; variable VAR (Volt-Ampere Reactive) controllers; electronic load controllers (ELCs) and solid-state controllers have been proposed [42-57]. However, these techniques, without exception, involve sophisticated and expensive equipment, which increase the cost and complexity of the system.

2.4.2 **Analysis of SEIGs**

For steady-state analysis, per phase equivalent circuit of the 3-phase SEIG has been developed from the classical mathematical model of induction machines. Based on this equivalent circuit, two different models, namely the loop impedance method [58-60] and the nodal admittance method [61-63], have been widely used to predict the generator performance.

For transient analysis, the *d-q* reference frame model of the SEIG, based on the generalized machine theory, has been extensively used for investigating the voltage built-up process and the impact of load variations [64-66].

The selection of excitation capacitors for the 3-phase SEIG was studied in [67-69], while the performance of the SEIGs, driven by regulated and unregulated prime mover, was investigated in [56, 70, 71].

2.4.3 **3-Phase SCIMs Supplying Single-Phase Loads**

In rural and suburban areas, the population is sparsely distributed, and the majority of electric loads are of single-phase nature. Therefore, a single-phase power supply is preferred over a 3-phase power supply to make the distribution system simple and cost-effective. Single-phase SCIMs can be used for single-phase electricity generation [72, 73], but the conventional 3-phase SCIMs has more advantages over single-phase machines to generate single-phase electricity, especially when the machine power rating exceeds 3kW [74, 75]. However, when a 3-phase SCIM is operated as a single-phase generator, the 3-phase stator currents are generally unbalanced. The unbalanced operation of the generator not only degrades the output power but causes many adverse effects such as mechanical vibration, poor efficiency, thermal overload and uncontrollable power factor [76].

Hence, various phase balancing techniques have been proposed and investigated to mitigate these concerns. All these techniques, in general, can be classified into two categories: one is based on the passive circuit elements and the other is based on the power electronic converters.

In the method proposed by [77], a steady-state power system balancer was investigated to resolve the aforementioned unbalanced conditions. By using a capacitance and an inductance of identical reactance, the power system balancer is able to balance the stator currents. However, the series resonance between the capacitance and inductance caused severe over voltages when the specified operating point is changed. The 3-phase SCIM in Smith connection, shown in Fig. 2.2(a), was proposed in [78]. It removed the danger of the resonance effect using capacitors exclusively. Additionally, it was capable of balancing stator phase currents for medium and heavy loads [79-81].

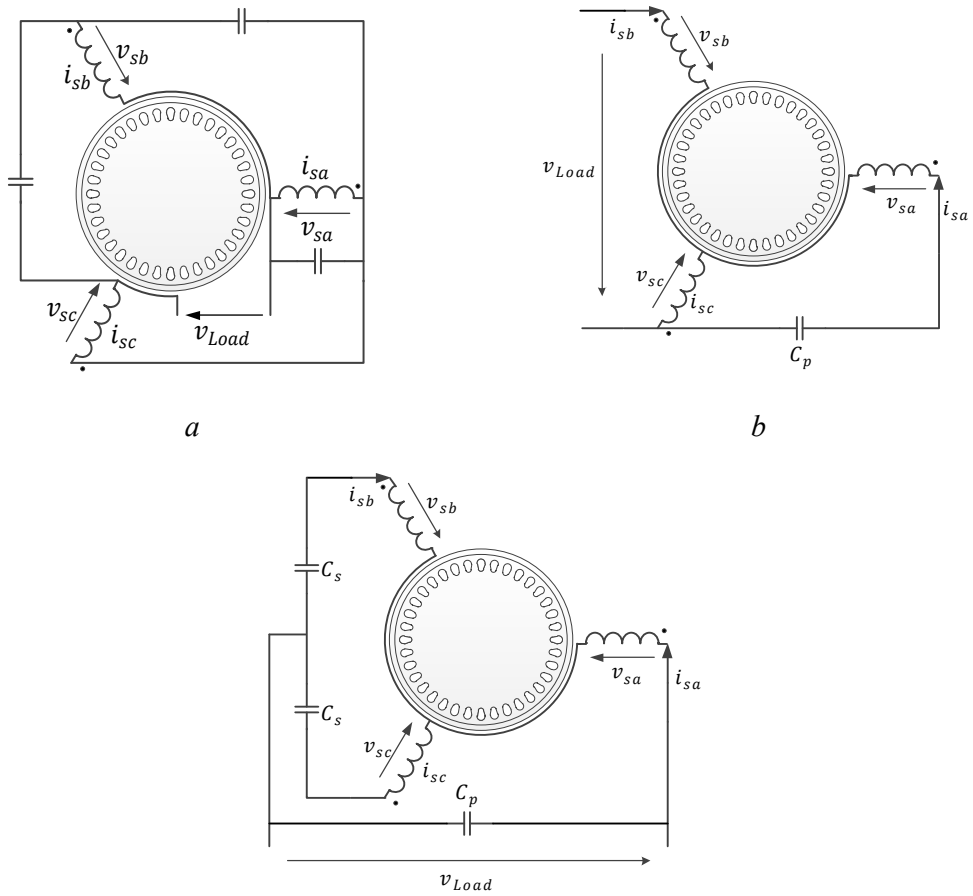

Fig. 2.2 3-phase SCIG with single-phase output: (a) Smith connection, (b) Steinmetz connection, (c) Fukami connection

The Steinmetz connection, shown in Fig. 2.2(b), is also widely used to balance 3-phase SCIGs operated in single-phase mode due to its simple configuration [82-84]. In contrast to the Smith connection, this method is applicable for 3-phase SCIMs with stator windings configured in both star and delta connections. With properly selected capacitance and operating speed, the perfect phase balance can be achieved through this connection. Another phase balancing scheme, proposed in [85], is illustrated in Fig. 2.3(c). It introduced series compensation capacitors to improve the regulation of output voltage. However, with this technique, it is more difficult to balance phase currents and the machine utilization is poor [75, 86]. Current injection method [87] and SCIGs with C-2C connection [88] have also been investigated as phase balancing techniques. Although all these passive circuit elements based techniques are able to balance the machine at a specific operating speed and load, the regulation of both power

and voltage with balanced operating conditions is very difficult to achieve under dynamic load and variable speed conditions. Additionally, these techniques have some inherent drawbacks such as self-excitation failure [89, 90], sensitivity to operating parameters [73, 91] and poor voltage and frequency regulations [92, 93]. Nonetheless, many attempts have been made to overcome these difficulties through various modifications to the existing techniques, including multi-mode operation for SCIGs with Smith connection [76, 79], SCIGs with different modified Steinmetz connections [94, 95] and Fukami configuration with damping resistance [86]. However, these modifications caused increased complexity and cost with limited improvement in performance.

With both the advances and reduction in cost in semiconductor devices, power electronic converters with active control started to emerge as an alternative approach to improve dynamic response as well as voltage and frequency regulation capability of the 3-phase SCIM based single-phase electricity generation systems. Methods in [96-98] employed two full-bridge converters in back-to-back configuration, as shown in Fig. 2.3(a), to improve the performance of the generator. However, the use of two full capacity converters with a bulky filter considerably increases the cost and size as well as the complexity of the system. As illustrated in Fig. 2.3(b), single-phase electricity could also be generated using a 3-phase SCIM with a combination of 3-phase converters and dump load [99, 100], but at the expense of significant power losses in the dump load and large output voltage drop under heavy load conditions. In [101, 102], an electronic load controller (ELC), as depicted in Fig. 2.3(c), was proposed to assist 3-phase SCIM in delta connection for standalone single-phase power generation, and subsequently extended for star connected 3-phase SCIMs with Fukami configuration [103]. Although this scheme provides a relatively low-cost and simple solution for 3-phase SCIM based single-phase power generation system, it is only applicable under constant input power conditions and suffers from low-efficiency and high harmonic distortion at output.

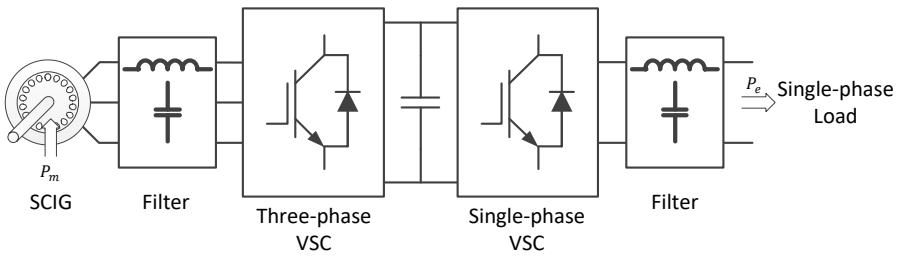

a

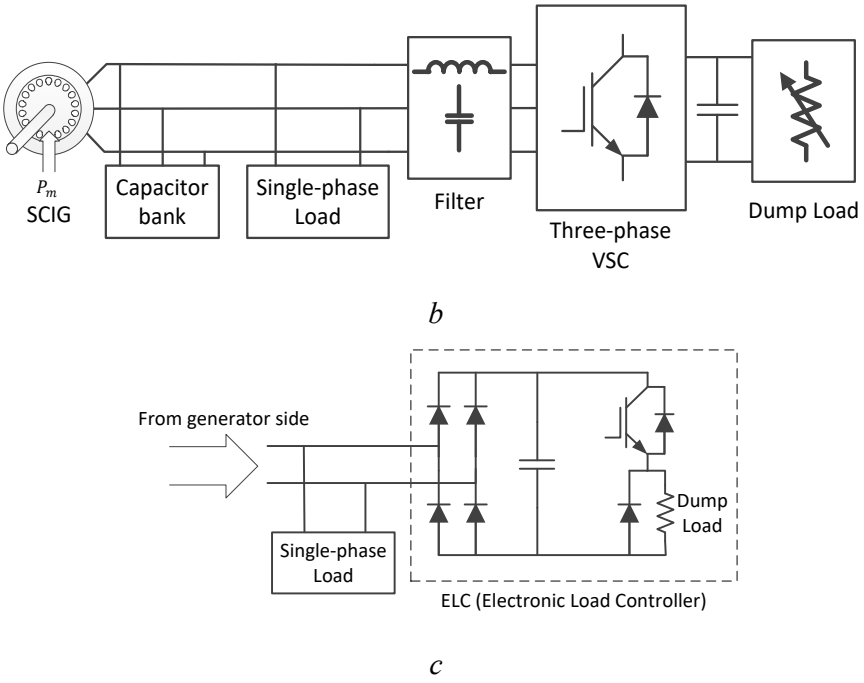

Fig. 2.3 Plots for:(a) The back-to-back configuration for 3-phase SCIGs feeding single-phase load (b) The voltage source converter (VSI) and dump load based configuration (c) The structure of electronic load controller (ELC)

Table. 2.2 summarises the advantages and disadvantages of the abovementioned two major phase balancing techniques.

Table. 2.2 Comparison of two major phase balancing techniques:

Phase balancing techniques	Advantages	Disadvantages
Passive Circuits Elements Based Techniques	• Low cost • Simple Configuration	• Poor voltage and frequency regulations • Poor machine utilization • Limited range of operating speed • Self-excitation failure
Power Electronic Converter Based Techniques	• Improved voltage and frequency regulations • Wide operating speed • Fast dynamic response	• High cost • Complex configuration • Bulky filter is needed • Low efficiency with dump load

2.4.4 **Analysis 3-Phase SCIGs Supplying Single-Phase Loads**

Numerous models have been proposed to investigate both the steady-state and dynamic behaviour of 3-Phase SCIGs supplying single-phase loads. In the steady-state analysis, the symmetrical components theory was widely used for developing models. In addition, the symmetrical components theory allows for determining the operating parameters, conditions of phase balancing and the values of excitation capacitors [104-108]. Based on the symmetrical components, various techniques such as Newton–Raphson method [109], Hooke-Jeeves optimization method [110] and genetic algorithm(GA) [111], were widely employed in the investigation of the passive circuit elements based single-phase generator. Similarly, in these techniques, the determination of the phase balancing conditions was enabled by imposing negative sequence symmetrical components to be equal to zero [112, 113]. In addition, the concepts of voltage unbalance factor (VUF) and current unbalance factor (CUF), which are evolved from symmetrical components, were widely used for evaluating the degree of the machine unbalance [113, 114].

However, the main disadvantage of symmetrical components is that the dynamic performance of the generator cannot be predicted and investigated. Therefore, the *d-q* reference frame model was widely employed in the dynamic analysis of the 3-Phase SCIGs operating on the single-phase mode [101, 114, 115]. Besides, a time-stepping finite element method (FEM) proposed in [116] was also adapted for dynamic performance studies.

2.4.5 **TSCAOI configuration**

Various attempts of operating a 3-phase SCIM to generate single-phase electricity have been surveyed in the section 2.4.3. In order to improve the electricity generation performance, a power conversion stage, comprising either a back-to-back converter or an alternating-current (AC)/direct-current (DC) converter, is employed on the front-end or back-end of the load. This power conversion stage allows for the variable-speed generation. However, it inevitably creates harmonic distortion of the load.

As an alternative, a new winding configuration that uses one of stator phases of the 3-phase SCIM as the excitation winding and the remaining two phases connected in series as the power winding, has been proposed [6-10]. This decoupled winding configuration is named as Two-Series Connected and One Isolated (TSCAOI) and shown in Fig. 2.4. It enables variable-speed single-phase electricity generation without using a power conversion stage.

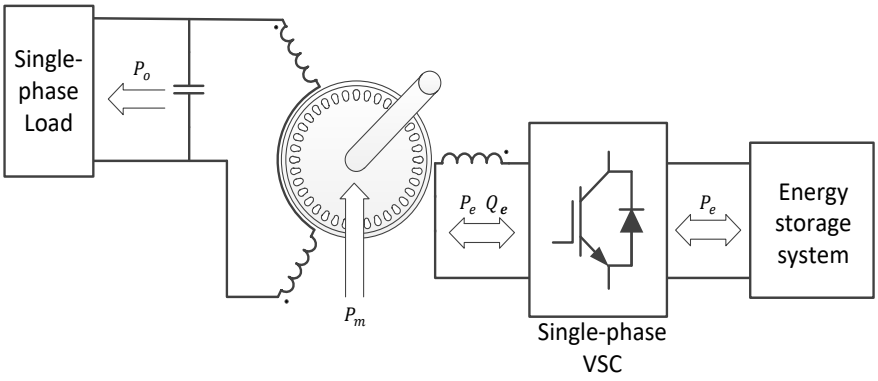

Fig. 2.4 The TSCAOI configuration for 3-phase SCIMs feeding single-phase load

Variable reactive power required by the TSCAOI configured generator is provided through the excitation winding by a small scale bi-directional converter. The bi-directional converter is connected with an energy-storage-system (ESS). In practice, a photovoltaic (PV) panel can be integrated into the ESS, enabling hybrid renewable energy generation (HREG) which can significantly improve the system reliability and energy utilization. The standalone single-phase electricity is generated through the power winding directly. With storage and retrieval of energy under light and heavy load conditions respectively, the combination of the ESS and the bi-directional converter allows constant frequency electricity generation for standalone applications under variable loads and rotor speeds conditions.

This unique winding configuration presents several interesting attributes, as presented below:

- With sinusoidal excitation, the frequency of the load voltage is as same as the frequency of the excitation voltage under varying loads and rotor speeds conditions.
- The amplitude of the load voltage is proportional to the applied excitation voltage, enabling the simple control scheme of the load voltage.
- Only a reduced-capacity converter is needed to generate electricity.
- The harmonic content of the load voltage is greatly attenuated due to the electric and magnetic decoupling of excitation winding and power winding. The bulky filters are therefore no longer necessary.

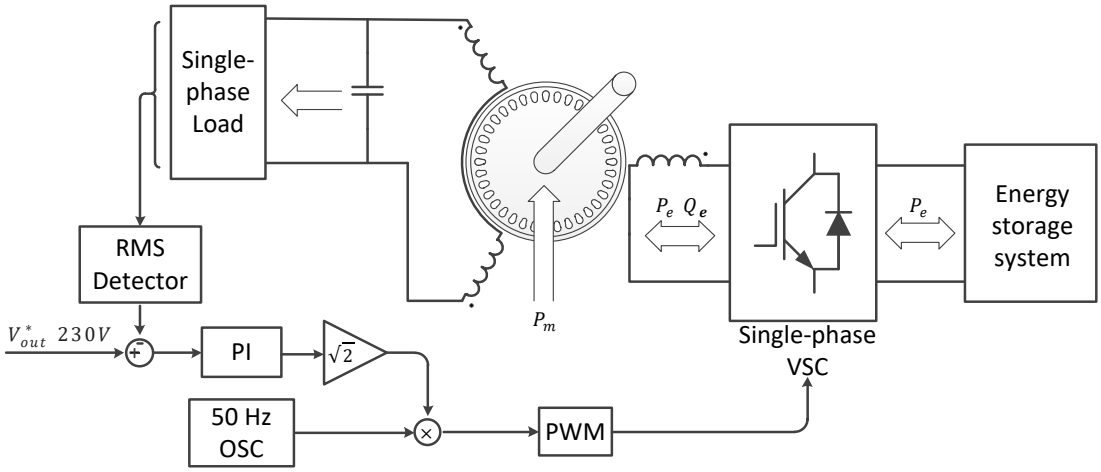

Fig. 2.5 Control block diagram for standalone TSCAOI configured generator

These attributes were used to develop the closed-loop controller for the standalone TSCAOI configured generator [8]. The controller is illustrated in Fig. 2.5. The single-phase output voltage is converted to a root-mean-square (RMS) value and compared with the desired output voltage. The voltage error is fed to a proportional–integral (PI) controller. This PI controller regulates the excitation voltage magnitude by providing the reference of the excitation voltage magnitude. The frequency of generation is set by a fixed-frequency oscillator, the output of which is multiplied with the excitation voltage magnitude reference to produce a sinusoidal excitation voltage reference for the full-bridge converter. The converter can be controlled using pulse-width modulation technique to produce the required voltage.

In comparison to other techniques, the TSCAOI configured generator is easier to implement. In addition, it can regulate the generated voltage at variable speeds with low cost. Therefore, it has been explored for generating single-phase electricity in small-scale renewable energy conversion systems. An improved dynamic model, which takes the core loss resistance into account, was presented in [117, 118] to improve the theoretical analysis of the TSCAOI configured generator. In [119], a gravitational search algorithm (GSA) based selective harmonic elimination (SHE) PWM technique was proposed, for excitation voltage control, to further decrease the harmonic distortion of the generated voltage. The integration of the TSCAOI configured generator into the hybrid renewable generation system has been investigated in [120, 121]. However, according to the literature review, there still exist three major unsolved difficulties associated with the TSCAOI configured generator.

- Firstly, in contrast to the conventional 3-phase cage induction machine, the TSCAOI configured induction machine lacks a unified equivalent circuit, through which the steady-state load and excitation characteristics of the generators can be investigated.
- Secondly, all the previous investigations of the TSCAOI configured generator are confined to the standalone power generation applications. However, the integration of the TSCAOI configured 3-phase cage induction generator into a single-phase distributed power system is yet to be investigated.
- Finally, although the TSCAOI generator is easy to implement and low in cost, the balanced operating condition and fast dynamic response are difficult to achieve, which severely restrict its practicability.

2.5. Summary

In this chapter, the squirrel cage induction generator (SCIG) was selected for the generation system studied in this thesis, by comparing the advantages and disadvantages of different electric generators. Then, an overview of the SCIG based small scale generation systems was presented, followed by a detailed survey of such systems in terms of their operating conditions, modelling methods, control strategies and limitations. The TSCAOI configuration, with its unique attributes, was emphasized by comparing with other techniques for operating a 3-phase SCIG to generate single-phase electricity. Finally, three major unsolved difficulties of the TSCAOI configured generator were identified and proposed as the research directions of this thesis.

Chapter 3

A Steady-State Equivalent Circuit Model for Standalone TSCAOI Configured Induction Generators

3.1. Introduction

3-phase cage induction machines, operated in two series-connected and one-isolated (TSCAOI) winding configuration, have been proposed to generate single-phase electricity at variable rotor speeds for renewable energy conversion systems. However, in comparison to other topologies employed for single-phase electricity generation using 3-phase SCIMs, there is no unified equivalent circuit for the TSCAOI configured induction generator to predict and investigate its steady-state performance. With the help of symmetrical components, this chapter therefore presents the steady-state equivalent circuit models, allowing to perform such detailed investigations.

A dynamic mathematical model, from which the final steady-state equivalent circuit model will be derived, is first presented in this chapter. The dynamic mathematical model is obtained using the winding function approach, which is much simpler than the transformation matrix based approach previously adopted in [8]. The winding function approach avoids the cumbersome mathematical derivation in [8]. More importantly, it directly offers an explicit description of the resulting winding distribution of the TSCAOI configured machine.

In order to investigate the load and excitation characteristics pertinently, it is desirable to isolate either the load circuit or excitation circuit from the derived equivalent circuit model. Accordingly, the dynamic model is then transformed into two different equivalent circuit models, enabling the investigation of either the load or excitation characteristics through the selection of the appropriate transformation matrix. Using these two different equivalent circuit models, this chapter therewith theoretically investigates the steady-state behaviour of the

generator and determines the impact of system parameters on the load and excitation characteristics, as well as on the level of voltage unbalance.

3.2. Dynamic Mathematical Model

To obtain the dynamic model of the 3-phase SCIM configured in the TSCAOI winding arrangement, this chapter proposes a modelling method, which is based on the winding function approach. This modelling approach not only eliminates the lengthy mathematical manipulation presented in [8] but also offers a direct visual insight into this particular generator concept which has not been possible with the reported modelling methods.

First, consider the stator winding distribution of a conventional 3-phase SCIM over 360 electrical degrees, as shown in Fig. 3.1 Each stator phase winding is assumed to be sinusoidally distributed along the air-gap, and the effects of slotting are neglected.

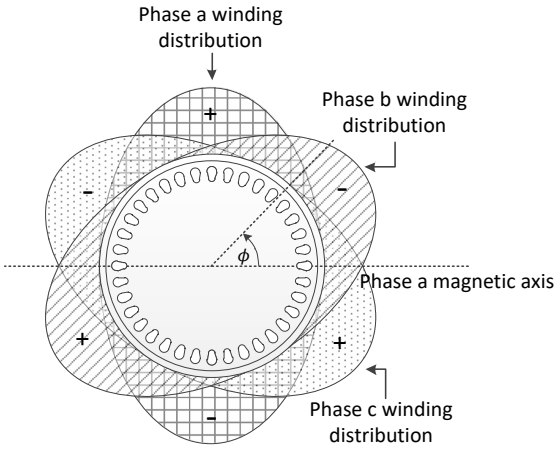

Fig. 3.1 Winding distribution of the stator of a conventional 3-phase SCIM over 360 electrical degrees

The winding function can be treated as spatial distribution of the magneto-motive force (MMF), excited by a unit current flowing through the associated winding [122]. It is therefore directly related to the MMF. By taking the magnetic axis of phase '*a*' as the reference, the winding functions of phase '*a*', '*b*' and '*c*' of the stator windings can be defined, respectively, as:

$$N_a(\phi) = \frac{N_s}{2} cos\ (\phi) \tag{3.1}$$

$$N_b(\phi) = \frac{N_s}{2} cos\ (\phi - \frac{2\pi}{3}) \tag{3.2}$$

$$N_c(\phi) = \frac{N_s}{2} cos\ (\phi - \frac{4\pi}{3}) \tag{3.3}$$

Where N_s is the per phase total number of turns and ϕ is the electrical angle with respect to the magnetic axis of the phase 'a' winding.

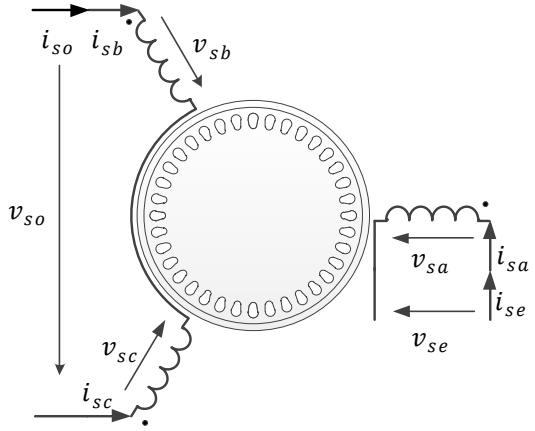

Fig. 3.2 TSCAOI winding configuration

Secondly, based on the TSCAOI winding arrangement, one of the three windings is separated as the One-Isolated (OI) winding and the remaining two windings, being connected in series, constitute the Two-Series-Connected (TSC) winding. As depicted in Fig. 3.2, with phase 'a' as the OI winding for excitation and phase 'b' and 'c' connected in series as the TSC winding for single-phase electricity generation, the winding functions of these two sets of windings can be readily obtained. The winding function of the OI winding, being identical to that of the phase 'a' winding, is given in (3.4), and the winding function of the TSC winding, which is directly related to its MMF distribution, is given in (3.5)

$$N_{se}(\phi) = \frac{N_s}{2} cos\ (\phi) \tag{3.4}$$

$$N_{so}(\phi) = N_b(\phi) - N_c(\phi) = \frac{\sqrt{3}N_s}{2} cos\left(\phi - \frac{\pi}{2}\right) \tag{3.5}$$

From (3.4) and (3.5), it can be noted that the TSC winding is still sinusoidally distributed along the air gap, but with $\sqrt{3}N_s$ turns. Furthermore, the TSC winding and the OI winding are located with their magnetic axes 90 electrical degrees apart. Hence they are magnetically decoupled. The resulting winding distribution of the TSCAOI configured 3-phase SCIM, over 360 electrical degrees, can be illustrated in Fig. 3.3. From Fig. 3.3, it is easy to observe that the TSCAOI configured 3-phase SCIM can be equivalent to an unsymmetrical 2-phase SCIM, by ignoring the slight differences in the stator resistance and leakage inductances. Thus, the modelling techniques and the analytical equations, developed in this chapter, are also suitable for investigating the behaviour of the inverter-assisted single-phase induction generator proposed in [123-126].

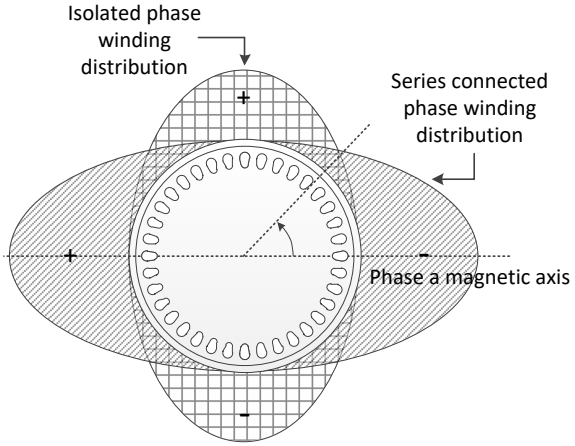

Fig. 3.3 Resulting winding distribution of the 3-phase SCIM in the TSCAOI winding configuration over 360 electrical degrees

The dynamics of the TSCAOI configured SCIM are modelled in the stationary $\alpha\beta$ reference frame. For derivation of the model, it is assumed that the α axis of the frame is aligned with the magnetic axis of OI winding. Since the number of turns of the equivalent 2-phase rotor windings in the $\alpha\beta$ reference frame can be arbitrarily selected [127], the rotor circuits are represented by 2-phase rotor circuits with each phase having the same number of turns with the OI winding. Moreover, the dependence of stator voltage equations on the turn's ratio between the TSC winding and OI winding can also be eliminated by referring the TSC winding to the OI winding.

Variables v'_{so} and i'_{so} are the referred voltage and current of the TSC winding, respectively. The relationships between the referred variables v'_{so} and i'_{so} and actual variables v_{so} and i_{so} are, respectively, given as:

$$v'_{so} = \frac{v_{so}}{\sqrt{3}} \tag{3.6}$$

$$i'_{so} = \sqrt{3} i_{so} \tag{3.7}$$

With the series connection of phase 'b' and 'c' windings, the resistance and leakage inductance of the TSC winding are twice as much as those of the OI winding. Consequently, the voltage equations of the stator and rotor circuits for the TSCAOI configured 3-phase SCIMs in stationary reference frame can be written as:

$$\begin{bmatrix} v_{se} \\ v'_{so} \\ 0 \\ 0 \end{bmatrix} = \begin{bmatrix} R_s + (L_{ls} + L_m)p & 0 & L_m p & 0 \\ 0 & \frac{2}{3}R_s + (\frac{2}{3}L_{ls} + L_m)p & 0 & L_m p \\ L_m p & \omega_r L_m & \frac{2}{3}R_r + \left(\frac{2}{3}L_{lr} + L_m\right)p & \omega_r\left(\frac{2}{3}L_{lr} + L_m\right) \\ -\omega_r L_m & L_m p & -\omega_r\left(\frac{2}{3}L_{lr} + L_m\right) & \frac{2}{3}R_r + \left(\frac{2}{3}L_{lr} + L_m\right)p \end{bmatrix} \begin{bmatrix} i_{se} \\ i'_{so} \\ i'_{r\alpha} \\ i'_{r\beta} \end{bmatrix} \tag{3.8}$$

Where variables v_{se} and i_{se} represent the voltage and current of the OI winding respectively, and variables $i'_{r\alpha}$ and $i'_{r\beta}$ represent the referred α and β components of the rotor currents, respectively. The p represents the differential operator d/dt, parameters R_s, L_{ls}, L_m, R_r and L_{lr} in (3.8) respectively represent the stator resistance, the stator leakage inductance, the magnetizing inductance, the rotor resistance and the rotor leakage inductance of the 3-phase SCIM and ω_r is the electrical angular frequency of the rotor in rad/s.

The electromagnetic torque applied on the rotor shaft can be expressed as:

$$T_e = \frac{P}{2} L_m (i'_{so} i'_{r\alpha} - i_{se} i'_{r\beta}) \tag{3.9}$$

where P is the number of poles. Equations (3.6)-(3.9) describe only the electrical behaviour of the TSCAOI configured SCIM. The motion of the machine can be described by

$$T_e - T_{ex} = \frac{2J}{P}\frac{d\omega_r}{dt} \tag{3.10}$$

where J is the rotor inertia in $kg \cdot m^2$, ω_r is the electrical angular frequency of the rotor in rad/s, T_e is the electromagnetic torque, in Nm and T_{ex} is the external torque applied on the rotor shaft, in Nm.

3.3. Steady-State Equivalent Circuit Model

To derive the steady-state equivalent circuit model of this particular generator, (3.8) can be readily transformed into the steady-state voltage equations via replacing p by $j\omega_s$, where ω_s is the synchronous angular frequency. As reviewed in Chapter 2 for the unbalanced excitation and load arrangements, the method of symmetrical components, proposed in [128], is most commonly used to develop the generalized steady-state equivalent model. Using symmetrical components, the unbalanced phasor variables of the generator can be represented in terms of two sets of balanced phasor variables, each having opposite phase sequence, as given below

$$\begin{bmatrix} \tilde{X}_\alpha \\ \tilde{X}_\beta \end{bmatrix} = [\boldsymbol{S}] \begin{bmatrix} \tilde{X}_{s+} \\ \tilde{X}_{s-} \end{bmatrix} \tag{3.11}$$

where $\tilde{X}$ represents any phasor variables of the stator and rotor circuits in the $\alpha\beta$ reference frame, $[\boldsymbol{S}]$ is the corresponding transformation matrix and the positive sequence and negative sequence symmetrical components are denoted by subscripts $s+$ and $s-$, respectively. However, according to the symmetrical components theory, the selection of $[\boldsymbol{S}]$ is not unique, and appropriately selected $[\boldsymbol{S}]$ will enable the derived equivalent circuit to pertinently investigate either the load or excitation characteristics of the generator, under steady-state conditions.

3.3.1 **Equivalent Circuit Model to Investigate Load Characteristics**

In order to derive an equivalent circuit model to investigate the load characteristics of the generator, it is desirable to isolate the load circuit in the model. Accordingly, the transformation matrix $[\boldsymbol{S}]$ is selected as:

$$[\boldsymbol{S}] = \begin{bmatrix} j & -j \\ 1 & 1 \end{bmatrix} \tag{3.12}$$

Then, the voltage equations in terms of the symmetrical components are directly obtained by substituting the transformation matrix $[\boldsymbol{S}]$, defined in (3.12), into the steady-state form of (3.8) as:

$$\begin{bmatrix} \tilde{V}_{s+} \\ \tilde{V}_{s-} \\ 0 \\ 0 \end{bmatrix} = \begin{bmatrix} [\boldsymbol{S}]^{-1} & [\boldsymbol{0}] \\ [\boldsymbol{0}] & [\boldsymbol{S}]^{-1} \end{bmatrix} \begin{bmatrix} R_s + j\omega_s(L_{ls} + L_m) & 0 & j\omega_s L_m & 0 \\ 0 & \frac{2}{3}R_s + j\omega_s(\frac{2}{3}L_{ls} + L_m) & 0 & j\omega_s L_m \\ j\omega_s L_m & \omega_r L_m & \frac{2}{3}R_r + j\omega_s(\frac{2}{3}L_{lr} + L_m) & \omega_r(\frac{2}{3}L_{lr} + L_m) \\ -\omega_r L_m & j\omega_s L_m & -\omega_r(\frac{2}{3}L_{lr} + L_m) & \frac{2}{3}R_r + j\omega_s(\frac{2}{3}L_{lr} + L_m) \end{bmatrix} \begin{bmatrix} [\boldsymbol{S}] & [\boldsymbol{0}] \\ [\boldsymbol{0}] & [\boldsymbol{S}] \end{bmatrix} \begin{bmatrix} \tilde{I}_{s+} \\ \tilde{I}_{s-} \\ \tilde{I}_{r+} \\ \tilde{I}_{r-} \end{bmatrix} \tag{3.13}$$

By simplification, the above voltage equations can be rewritten in a compact form as:

$$\begin{bmatrix} \tilde{V}_{s+} \\ \tilde{V}_{s-} \\ 0 \\ 0 \end{bmatrix} =$$

$$\begin{bmatrix} \frac{5}{6}R_s + \frac{5}{6}j\omega_s L_{ls} + j\omega_s L_m & -\frac{1}{6}Rs - \frac{1}{6}j\omega_s L_{ls} \\ -\frac{1}{6}Rs - \frac{1}{6}j\omega_s L_{ls} & \frac{5}{6}R_s + \frac{5}{6}j\omega_s L_{ls} + j\omega_s L_m \\ j\omega_s L_m & 0 \\ 0 & j\omega_{syn} L_m \end{bmatrix}$$

$$\begin{bmatrix} j\omega_s L_m & 0 \\ 0 & j\omega_s L_m \\ \frac{1}{s}\frac{2}{3}R_r + j\omega_s(\frac{2}{3}L_{lr} + L_m) & 0 \\ 0 & \frac{1}{2-s}\frac{2}{3}R_r + j\omega_s(\frac{2}{3}L_{lr} + L_m) \end{bmatrix} \begin{bmatrix} \tilde{I}_{s+} \\ \tilde{I}_{s-} \\ \tilde{I}_{r+} \\ \tilde{I}_{r-} \end{bmatrix} \quad (3.14)$$

where *s* is the slip.

Based on the inverse of the transformation matrix given in (3.12), the symmetrical components of stator voltages can be expressed as:

$$\tilde{V}_{s+} = -\frac{j}{2}\tilde{V}_{se} + \frac{1}{2}\tilde{V}'_{so} \quad (3.15)$$

$$\tilde{V}_{s-} = \frac{j}{2}\tilde{V}_{se} + \frac{1}{2}\tilde{V}'_{so} \quad (3.16)$$

When the load impedance Z is connected with the power winding in parallel, the referred output voltage $\tilde{V}'_{so}$ in (3.15) and (3.16) can be replaced by $-Z'\tilde{I}'_{so}$, where Z' is the referred load impedance, equalling to $Z/3$. Moreover, based on (3.12), $\tilde{I}'_{so}$ can be further replaced by $(\tilde{I}_{s+} + \tilde{I}_{s-})$, and the symmetrical components of stator voltages can be further expressed as:

$$\tilde{V}_{s+} = -\frac{j}{2}\tilde{V}_{se} - \frac{1}{2}Z'\tilde{I}'_{so} = -\frac{j}{2}\tilde{V}_{se} - \frac{1}{2}Z'\tilde{I}_{s+} - \frac{1}{2}Z'\tilde{I}_{s-} \quad (3.17)$$

$$\tilde{V}_{s-} = \frac{j}{2}\tilde{V}_{se} - \frac{1}{2}Z'\tilde{I}'_{so} = \frac{j}{2}\tilde{V}_{se} - \frac{1}{2}Z'\tilde{I}_{s+} - \frac{1}{2}Z'\tilde{I}_{s-} \quad (3.18)$$

Substituting (3.17) and (3.18) in (3.14) and rearranging the obtained voltage equations, the steady-state voltage equations can be given as:

$$\begin{bmatrix} -\frac{j}{2}\tilde{V}_{se} \\ \frac{j}{2}\tilde{V}_{se} \\ 0 \\ 0 \end{bmatrix} =$$

$$\begin{bmatrix} \frac{5}{6}R_s + \frac{5}{6}j\omega_s L_{ls} + j\omega_s L_m + \frac{1}{2}Z' & -\frac{1}{6}Rs - \frac{1}{6}j\omega_s L_{ls} + \frac{1}{2}Z' \\ -\frac{1}{6}Rs - \frac{1}{6}j\omega_s L_{ls} + \frac{1}{2}Z' & \frac{5}{6}R_s + \frac{5}{6}j\omega_s L_{ls} + j\omega_s L_m + \frac{1}{2}Z' \\ j\omega_s L_m & 0 \\ 0 & j\omega_s L_m \end{bmatrix}$$

$$\begin{bmatrix} j\omega_s L_m & 0 \\ 0 & j\omega_s L_m \\ \frac{1}{s}\frac{2}{3}R_r + j\omega_s(\frac{2}{3}L_{lr} + L_m) & 0 \\ 0 & \frac{1}{2-s}\frac{2}{3}R_r + j\omega_s(\frac{2}{3}L_{lr} + L_m) \end{bmatrix} \begin{bmatrix} \tilde{I}_{s+} \\ \tilde{I}_{s-} \\ \tilde{I}_{r+} \\ \tilde{I}_{r-} \end{bmatrix} \quad (3.19)$$

Equation (3.19) can be represented by the equivalent circuit shown in Fig. 3.4(a), in which the referred load impedance Z' is explicitly isolated.

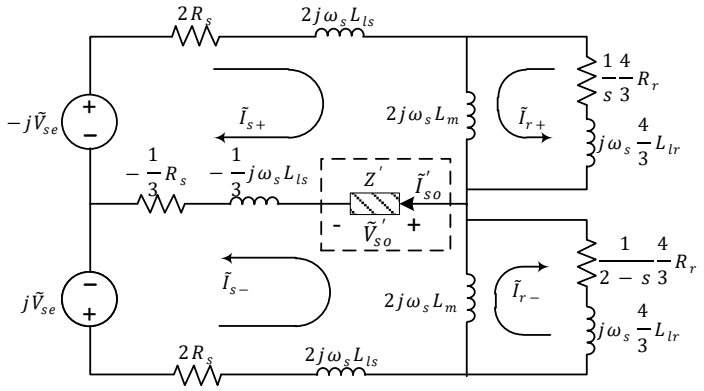

a

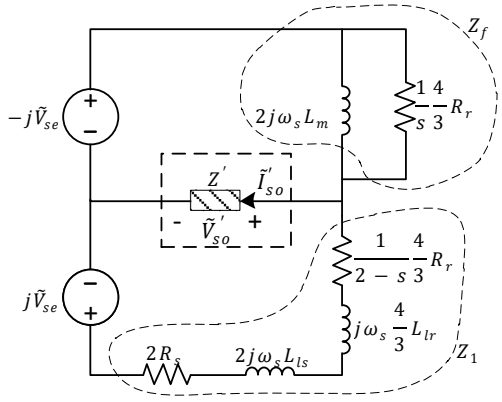

b

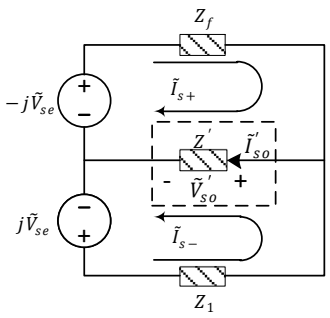

c

Fig. 3.4 The unified lumped equivalent circuit to investigate the load characteristics (a) Complete equivalent circuit (b) Simplified circuit and (c) Simplified circuit

The theoretical and experimental results presented in the next chapter correspond to an operating range within ± 10% synchronous speed, which is reasonable for maintaining the voltage unbalance within acceptable limits. In this range the slip *s* is small. Therefore, the rotor impedance of the forward field is largely resistive and comparable with the magnetizing branch. Conversely, reflected rotor resistance $4R_r/3(2-s)$ in the backward field becomes comparable with the rotor leakage inductance, enabling to simplify the equivalent circuit by neglecting the magnetizing branch in the backward field. In consequence, as shown in Fig. 3.4(b), the rotor leakage inductance in the forward field and the magnetizing branch in the backward field are ignored. Furthermore, the referred load impedance Z' is much larger than $(-R_s/3 - j\omega_s L_{ls}/3)$ in practise. Thus $(-R_s/3 - j\omega_s L_{ls}/3)$ is also ignored. Consequently Fig. 3.4(a) can be simplified to Fig. 3.4(b).

For clarity, let

$$Z_f = 2j\omega_s L_m \parallel \left(\frac{1}{s}\frac{4}{3}R_r\right) \tag{3.20}$$

$$Z_1 = 2R_s + 2j\omega_s L_{ls} + j\omega_s \frac{4}{3}L_{lr} + \frac{1}{s-2}\frac{4}{3}R_r \tag{3.21}$$

With the new impedances defined above, Fig. 3.4(b) can be further simplified to Fig. 3.4(c). The referred load voltage $\tilde{V}'_{so}$ can therewith be calculated from Fig. 3.4(c) as:

$$\tilde{V}'_{load} = \tilde{V}'_{so} = -Z'\tilde{I}'_{so} = -j\tilde{V}_{se}\frac{Z'(Z_f - Z_1)}{Z'Z_1 + Z'Z_f + Z_1Z_f} \tag{3.22}$$

Equation (3.22) can now be used to investigate the load characteristics of this generator. It is noticeable that when the load voltage is fixed to a specified value, there is an inversely proportional relationship between the load impedance and the required excitation winding voltage, and this is independent of the operating speed.

The major drawback of the TSCAOI configured SCIG is its asymmetrical excitation and load arrangement which inevitably causes unbalanced operation of the generator with torque fluctuations. The torque fluctuation, which is the major source of the audible noise and mechanical vibrations of this unbalanced induction generator, not only compromises the overall performance but degrades the operating life of the generator.

However, obtaining an expression for the electromagnetic torque under unbalanced operating conditions through mathematical manipulation is extremely difficult, and makes the prediction of the impact of system parameters on the torque fluctuation impossible [129]. Therefore, the voltage unbalance factor (VUF), defined in (3.23) exhibiting approximately proportional relationship with the torque fluctuation, is used to represent the level of the torque fluctuation.

$$VUF = \frac{Modulus\ of\ the\ negative\ sequence\ voltage}{Modulus\ of\ the\ positive\ sequence\ voltage} \tag{3.23}$$

Based on the selected transformation matrix, the VUF in (3.23) can be further expanded as:

$$VUF = \left|\frac{\tilde{V}_{s-}}{\tilde{V}_{s+}}\right| = \left|\frac{\frac{j}{2}\tilde{V}_{se} + \frac{1}{2}\tilde{V}'_{so}}{-\frac{j}{2}\tilde{V}_{se} + \frac{1}{2}\tilde{V}'_{so}}\right| \tag{3.24}$$

By substituting the referred load voltage $\tilde{V}'_{so}$, given by (3.22), in (3.24), both positive and negative sequence voltages can be expressed in terms of $\tilde{V}_{se}$, and VUF defined in (3.24) can be further simplified and given as:

$$VUF = \left|\frac{2/Z_f + 1/Z'}{2/Z_1 + 1/Z'}\right| \tag{3.25}$$

In practise, a compensation capacitor C_{comp} is often connected with the resistive load in parallel to compensate the reactive power requirement of the generator. The referred load impedance therefore can be expressed as:

$$Z' = R'_{load} \parallel \frac{1}{j\omega_s C'_{comp}} \tag{3.26}$$

where, R'_{load} and C'_{comp} are the referred resistive load and compensation capacitor, respectively.

Thus, (3.25) can be expanded as:

$$VUF = \left|\frac{j\left(\omega_s C'_{comp} - \frac{1}{\omega_s L_m}\right) + \left(\frac{3s}{2R_r} + \frac{1}{R'_{load}}\right)}{\frac{2}{Z_1} + \frac{1}{R'_{load}} + j\omega_s C'_{comp}}\right| \tag{3.27}$$

Equation (3.27) provides not only a comprehensive view of the unbalanced operation of the machine, but also a deep insight into how the system parameter variations impact the generator operation and torque fluctuation. In practise, the VUF should be maintained as small as possible to approach the ideal balanced operating condition as well as to minimize the torque fluctuation. Equation (3.27) will therefore serve as the guideline for parameter selection of this generator.

3.3.2 **Equivalent Circuit to Investigate Excitation Characteristics**

In order to derive an equivalent circuit to investigate the excitation winding characteristics of the generator, the transformation matrix [$\boldsymbol{S}$] for isolating the excitation source should be appropriately selected as:

$$[\boldsymbol{S}] = \begin{bmatrix} 1 & 1 \\ -j & j \end{bmatrix} \tag{3.28}$$

The voltage equations in terms of the symmetrical components can be obtained by substituting (3.28) into the steady-state form of (3.8) as:

$$\begin{bmatrix} \tilde{V}_{s+} \\ \tilde{V}_{s-} \\ 0 \\ 0 \end{bmatrix} = \begin{bmatrix} \frac{5}{6}R_s + \frac{5}{6}j\omega_s L_{ls} + j\omega_s L_m & \frac{1}{6}Rs + \frac{1}{6}j\omega_s L_{ls} & j\omega_s L_m & 0 \\ \frac{1}{6}Rs + \frac{1}{6}j\omega_s L_{ls} & \frac{5}{6}R_s + \frac{5}{6}j\omega_s L_{ls} + j\omega_s L_m & 0 & j\omega_{syn} L_m \\ j\omega_s L_m & 0 & \frac{1}{s}\frac{2}{3}R_r + j\omega_s(\frac{2}{3}L_{lr} + L_m) & 0 \\ 0 & j\omega_s L_m & 0 & \frac{1}{2-s}\frac{2}{3}R_r + j\omega_s(\frac{2}{3}L_{lr} + L_m) \end{bmatrix} \begin{bmatrix} \tilde{I}_{s+} \\ \tilde{I}_{s-} \\ \tilde{I}_{r+} \\ \tilde{I}_{r-} \end{bmatrix} \tag{3.29}$$

Based on the selected transformation matrix, the symmetrical components of the stator voltages can be given, in terms of $\tilde{V}_{se}$ and $\tilde{V}'_{so}$, as:

$$\tilde{V}_{s+} = \frac{1}{2}\tilde{V}_{se} + \frac{j}{2}\tilde{V}'_{so} \tag{3.30}$$

$$\tilde{V}_{s-} = \frac{1}{2}\tilde{V}_{se} - \frac{j}{2}\tilde{V}'_{so} \tag{3.31}$$

The referred output voltage $\tilde{V}'_{so}$ can also be replaced by $-Z'\tilde{I}'_{so}$, and $\tilde{I}'_{so}$ is equal to $(-j\tilde{I}_{s+} + j\tilde{I}_{s-})$ according to the selected transformation matrix. As a consequence, the

symmetrical components of the stator voltages, given in (3.30) and (3.31), can be further expressed as:

$$\tilde{V}_{s+} = \frac{1}{2}\tilde{V}_{se} - \frac{j}{2}Z'\tilde{I}'_{so} = \frac{1}{2}\tilde{V}_{se} - \frac{1}{2}Z'\tilde{I}_{s+} + \frac{1}{2}Z'\tilde{I}_{s-} \tag{3.32}$$

$$\tilde{V}_{s-} = \frac{1}{2}\tilde{V}_{se} + \frac{j}{2}Z'\tilde{I}'_{so} = \frac{1}{2}\tilde{V}_{se} + \frac{1}{2}Z'\tilde{I}_{s+} - \frac{1}{2}Z'\tilde{I}_{s-} \tag{3.33}$$

Substituting (3.32) and (3.33) into (3.29) and rearranging the obtained equations, the resulting steady-state voltage equations can be given as:

$$\begin{bmatrix} \frac{1}{2}\tilde{V}_{se} \\ \frac{1}{2}\tilde{V}_{se} \\ 0 \\ 0 \end{bmatrix} =$$

$$\begin{bmatrix} \frac{5}{6}R_s + \frac{5}{6}j\omega_s L_{ls} + j\omega_s L_m + \frac{1}{2}Z' & \frac{1}{6}Rs + \frac{1}{6}j\omega_s L_{ls} - \frac{1}{2}Z' & j\omega_s L_m & 0 \\ \frac{1}{6}Rs + \frac{1}{6}j\omega_s L_{ls} - \frac{1}{2}Z' & \frac{5}{6}R_s + \frac{5}{6}j\omega_s L_{ls} + j\omega_s L_m - \frac{1}{2}Z' & 0 & j\omega_s L_m \\ j\omega_s L_m & 0 & \frac{1}{s}\frac{2}{3}R_r + j\omega_s(\frac{2}{3}L_{lr} + L_m) & 0 \\ 0 & j\omega_s L_m & 0 & \frac{1}{2-s}\frac{2}{3}R_r + j\omega_s(\frac{2}{3}L_{lr} + L_m) \end{bmatrix} \begin{bmatrix} \tilde{I}_{s+} \\ \tilde{I}_{s-} \\ \tilde{I}_{r+} \\ \tilde{I}_{r-} \end{bmatrix} \tag{3.34}$$

The corresponding equivalent circuit model, through which the terminal characteristics of the external excitation source can be explicitly investigated, is shown in Fig. 3.5(a).

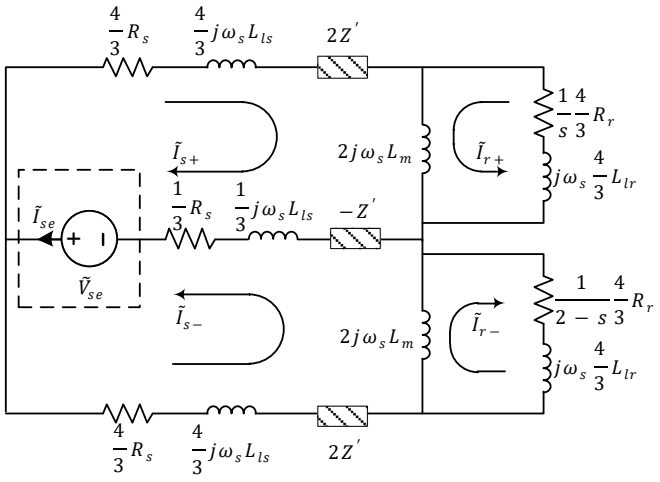

a

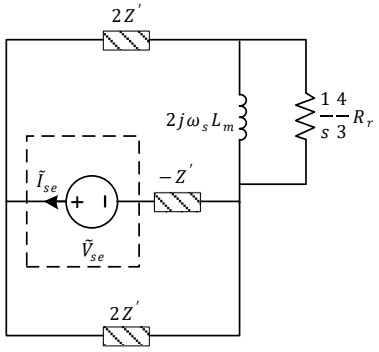

b

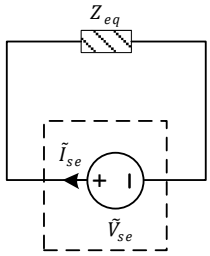

c

Fig. 3.5 The unified lumped equivalent circuit to investigate the excitation characteristics (a) Complete equivalent circuit (b) Simplified circuit and (c) Simplified circuit

Similarly using appropriate approximations, Fig. 3.5(a) can be replaced by Fig. 3.5(b), and then Fig. 3.5(b) can be further expressed by its simplest form shown in Fig. 3.5(c). In Fig. 3.5(c), both the external load circuit and machine itself are represented by an equivalent impedance Z_{eq}, which is connected in series with the excitation source. The expression of the excitation current can therefore be written as:

$$\tilde{I}_{se} = \frac{\tilde{V}_{se}}{Z_{eq}} = \tilde{V}_{se}\left(\frac{3s}{R_r} + \frac{1}{R'_{load}}\right) + j\tilde{V}_{se}\left(-\frac{2}{\omega_s L_m} + \omega_s C'_{comp}\right) \tag{3.35}$$

In (3.35), the first two terms represent the active component of the excitation current and the last two terms represent the reactive component of the excitation current. These two components are of great importance in the investigation of the TSCAOI configured generator. From (3.35), it is clear that the magnitude of no-load excitation current, for a given excitation voltage, is always minimum at synchronous speed ($s = 0$) regardless of machine parameters. When the load is connected, the minimum magnitude of the excitation current is achieved at $s = -R_r/3R'_{load}$. In (3.35), it is also observed that the reactive component of the excitation current is mainly influenced by the magnetizing inductance and the compensation capacitance. Thus, a properly selected compensation capacitance will significantly reduce the reactive power requirement of the bi-directional converter.

3.4. Summary

In this chapter, a winding function modelling approach was introduced to derive the dynamic model of the TSCAOI configured generator. It has been shown that the use of the winding function approach led to a simpler modelling process. More importantly, winding function approach provided a direct and visualized description of the resulting winding distribution of the TSCAOI configured generator, and revealed the relationship between TSCAOI configured 3-phase SCIG and single-phase SCIG. Using the symmetrical component theory, the obtained dynamic model was transformed into two different equivalent circuit models. Using these two equivalent circuit models, the load and excitation characteristics of the generator, as well as the impact of the machine parameters on its performance, were investigated.

Chapter 4

Performance of Standalone TSCAOI Configured Induction Generators

4.1. Introduction

Based on the proposed equivalent circuit models, the steady-state behaviour and performance of the standalone TSCAOI configured induction generator have been theoretically investigated in the previous chapter. However, the accuracy of both proposed model and performance characteristics is yet to be proven.

Therefore in this chapter, the general steady-state performance of the standalone TSCAOI configured generator is firstly investigated through simulations and experimentally under various operating conditions. Secondly, the steady-state load and excitation characteristics of the generator are also investigated using both simulations as well as experiments. Both the simulated and experimental results are in good agreement and exhibit same trend. These results further indicate that the load and excitation characteristics of this particular generator can be accurately predicted by the analytical equations extracted from the proposed equivalent circuit models. Finally, this chapter explains the causes of the torque fluctuations in this generator. However, the difficulties in the manipulation of the electromagnetic torque under unbalanced operating conditions, make it impossible to investigate the impact of the system parameters on the torque fluctuation. This chapter therefore proposes to use voltage unbalance factor (VUF) to determine the approximate level of the torque fluctuation and verifies the effectiveness of this approach by simulations.

4.2. General Steady-State Performance

In order to demonstrate the practical viability of the standalone TSCAOI configured generator, a prototype generator was configured in the TSCAOI winding arrangement, using a 4-pole, 3kW, 400V cage induction machine. The parameters of this cage induction machine

are given in the Appendix A. Based on this prototype generator, the experimental platform, on which a small scale generation system was implemented, was built and shown in Fig. 4.1.

In the experiment, the prototype generator was mechanically coupled to another induction machine controlled by a variable-speed drive (VSD) to emulate the variable-speed prime mover. A variable resistive load was connected with the power winding, and a single-phase voltage source converter (VSC) was connected with the excitation winding to regulate the load voltage at 230V/50Hz under varying rotor speeds. The control software of the single-phase VSC was developed on a TI Delfino 28335 controller board, and the control algorithm has been detailed in Chapter 2. The load voltage was measured by the isolated voltage sensor, and the feedback signal of the load voltage was read by the control board through an A/D (Analog to Digital) converter. According to the measured and desired load voltages, the controller board provides the PWM (Pulse Width Modulation) signals to the VSC.

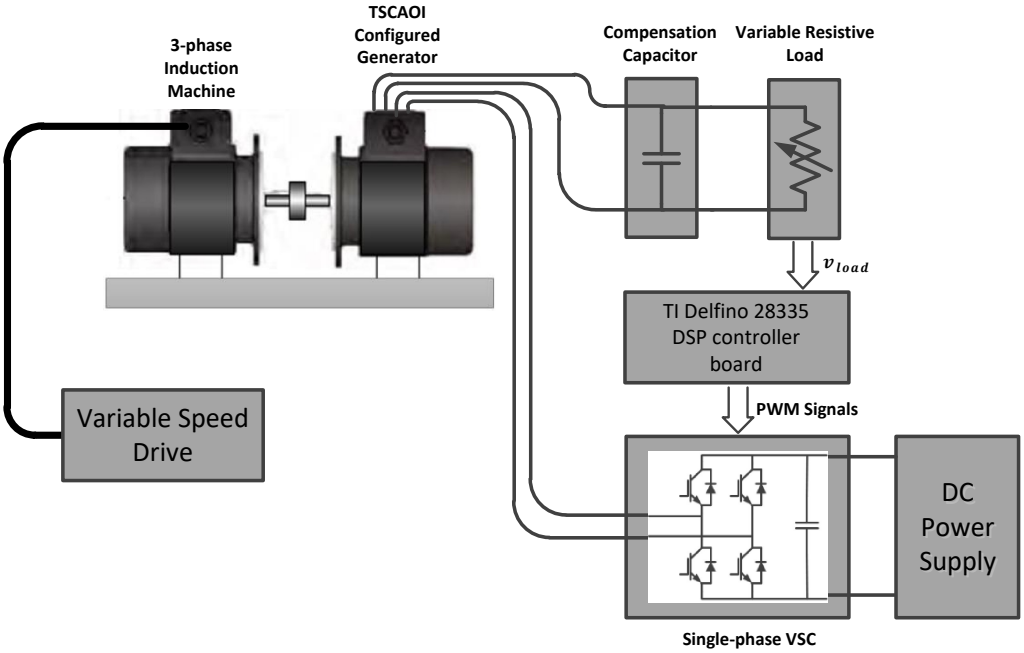

Fig. 4.1 Experimental setup

Before any detailed investigations through simulations and experiments, the value of the compensation capacitor must be first determined. The compensation capacitor, connected with the resistive load in parallel, is employed to reduce the reactive-power requirement of the VSC, having a significant impact on the system operating range.

For this particular generation system, the operating range is dependent on both its load range and speed range. Within the operating range, the phase currents and voltages and the VUF of this prototype generator must be all within the restricted range. Conversely, if any of them exceeds the restricted range, the corresponding operating point will not be within the operating range of the generator.

In practice, the phase currents and voltages are limited within 8.5A and 300V respectively, and the maximum VUF is not allowed to exceed 0.15. In addition, when this prototype generator is operated with a specific compensation capacitor, the actual phase currents and voltages and also the VUF of the generator at different resistive loads and rotor speeds can be calculated by MATLAB using the previously derived steady-state mathematical model. Therefore, by determining whether the calculated values are within the restricted ranges, the practical operating range of this prototype generator with the specific compensation capacitor can be obtained.

The blue shaded region in Fig. 4.2 indicates the simulated operating range satisfying the above criteria, when the prototype generator was connected with a 20uF compensation capacitor to supply power to the resistive load at 230 V/50 Hz. The area of the blue shaded region can be used to quantify the operating range of the generator. Therefore, the compensation capacitor can be selected by comparing the areas of the blue shaded regions with respect to different capacitors. The operating ranges of this prototype generator using different compensation capacitors are compared in the percentage bar graph illustrated in Fig. 4.3. According to Fig. 4.3, the 20uF capacitor provides the maximum operating range, hence it was selected.

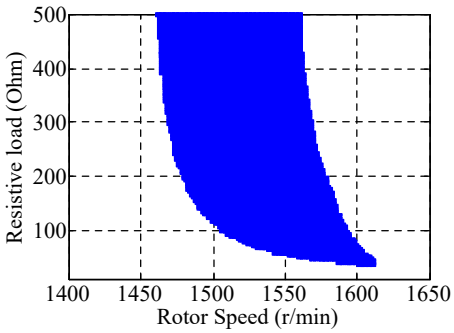

Fig. 4.2 Operating range of the prototype generator when a 20uF compensation capacitor was connected

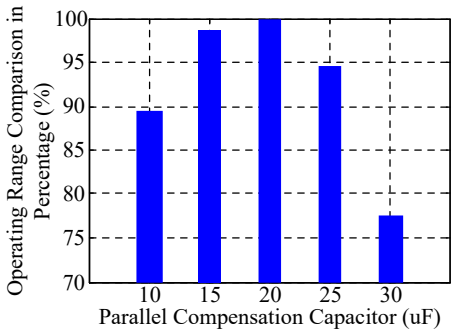

Fig. 4.3 Operating range comparison using different compensation capacitors

Fig. 4.4(a) and Fig. 4.4(b) show the contour plots simulated by MATLAB for the current variations of the excitation winding and the power winding, respectively, with varying loads and rotor speeds, when the load voltage is regulated at 230V/50Hz. At light loads, it is clear from Fig. 4.4(a) that the minimum excitation winding current is achieved at rotor speeds slightly above the synchronous speed. At heavy loads, however, the speed corresponding to the minimum excitation winding current increases substantially with increasing load. In contrast, the power winding current varies only with the changing loads, as shown in Fig. 4.4(b), because the load voltage is regulated at 230V/50Hz for all speeds.

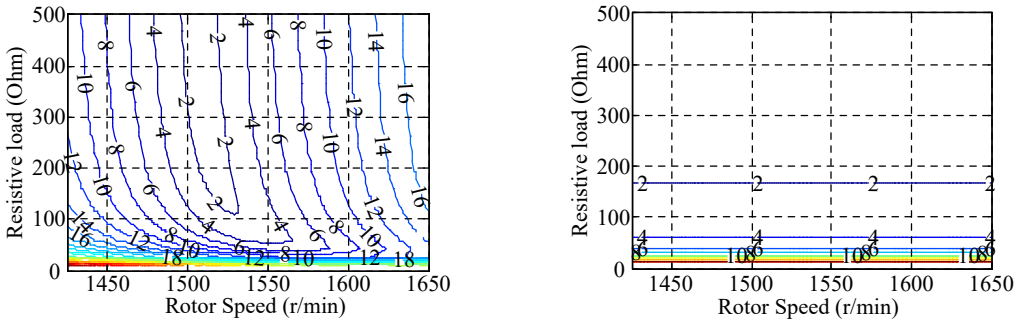

a *b*

Fig. 4.4 Contours of the excitation winding current (a) the power winding current (b) with the changing loads and rotor speeds.

The contours showing the variations of the excitation winding voltage with the changing loads and rotor speeds are presented in Fig. 4.5, when the load voltage is regulated at 230V/50Hz.

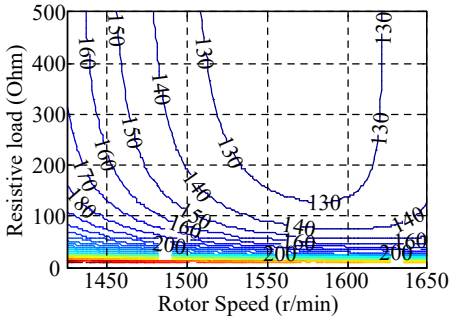

Fig. 4.5 Contours of the excitation winding voltage with the changing loads and rotor speeds

As shown in Fig. 4.5, the required excitation winding voltage should be augmented when a heavier load is connected over a wide range of rotor speeds. The simulated and experimental variations of the excitation winding voltage versus the rotor speeds are illustrated in Fig. 4.6 for three different resistive loads, when the load voltage is regulated at 230V/50Hz. The simulated and experimental results are in agreement and exhibit the same trend. As observed earlier in Fig. 4.5, Fig. 4.6 consistently indicates that excitation winding voltage is needed to increase with the increasing of the load, when the output voltage is regulated at a fixed value. Although the impedance seen from the excitation winding is complex in nature, being dependent on both the synchronous angular frequency and the slip frequency, the decrease in the required excitation winding voltage with the increasing rotor speed is obvious in Fig. 4.6.

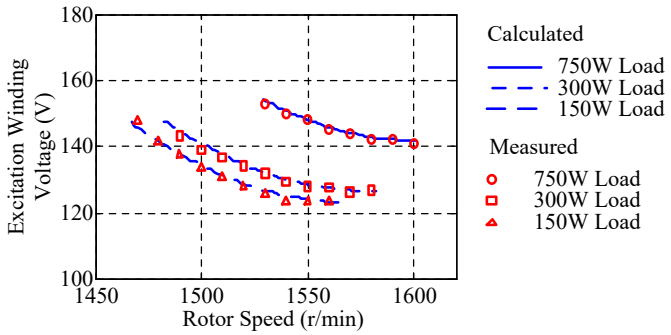

Fig. 4.6 Variations of the excitation winding voltage with the changing rotor speeds when three different loads are connected

Fig. 4.7 illustrates the variations of the excitation winding current for varying rotor speeds and different resistive loads.

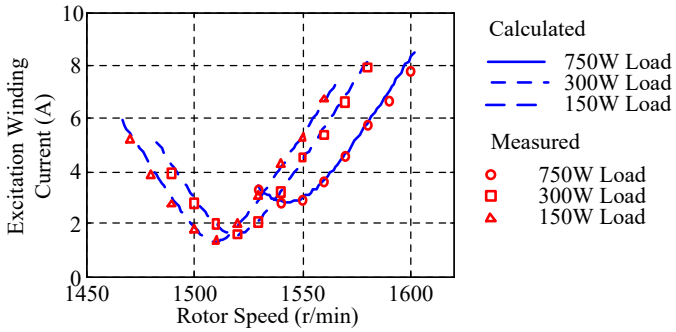

Fig. 4.7 Variations of the excitation winding current with the changing rotor speeds when three different loads are connected

As shown in Fig. 4.7, for each load, there exists a unique rotor speed, at which the excitation winding current is minimum. The variations of the active power provided by the

excitation winding for varying rotor speeds and different loads are illustrated in Fig. 4.8. The positive power and negative power indicate that the active power is supplied and absorbed by the excitation winding, respectively.

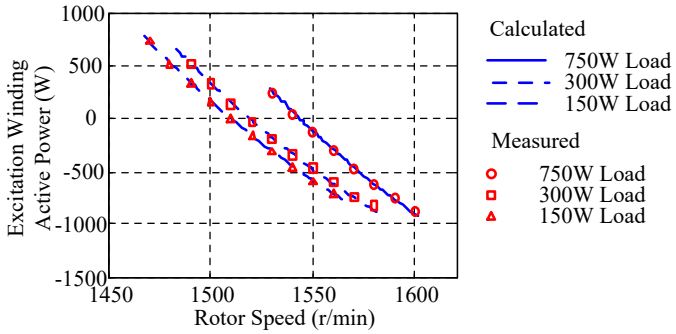

Fig. 4.8 Variations of the active power of the excitation winding with the changing rotor speeds when three different loads are connected

It can be noted that there also exists a unique rotor speed for each load at which the excitation winding neither supplies nor absorbs active power. This is because both the load power and losses of the generator at this speed are met by the prime mover. In addition, this speed is basically identical to the speed of minimum excitation winding current observed in Fig. 4.7. Because, when the rotor speed is increased beyond this unique speed, the power supplied by the prime mover is increased, and the excess power is therewith absorbed by the excitation winding, resulting in an increase in the excitation winding current. Similarly, when the rotor speed is reduced below the unique speed, the power of the prime mover is supplemented by the excitation winding, also resulting in an increase in the excitation winding current.

The performance of the proposed generator was also evaluated in term of the efficiency for three different load power levels, as shown in Fig. 4.9. A maximum efficiency of approximately 82% is observed when 750W load is connected.

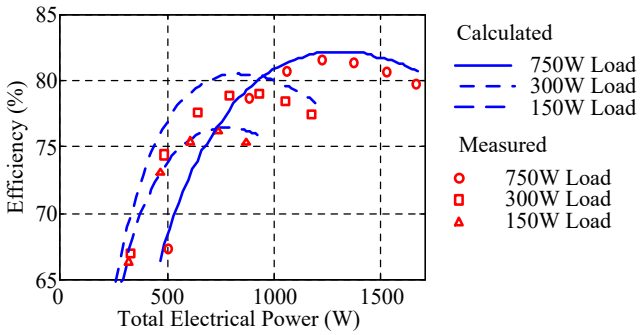

Fig. 4.9 Efficiency of the generator when three different loads are connected

4.3. Load Characteristics

The equivalent circuit model, derived for investigating the load characteristics of the standalone TSCAOI configured generator, has already been obtained in Section 3.3.1. Using this model, the relationship between the load voltage and the excitation winding voltage can be explicitly described by (3.22). According to (3.22), the load voltage is proportional to the excitation winding voltage but inversely proportional to the load impedance.

Fig. 4.10 shows the simulated and experimental variations of the no-load voltage with the changing rotor speeds for three different compensation capacitors, when the excitation winding voltage is fixed at 135V/50Hz. It is clear that there exists an inverse relationship between the load voltage and load impedance, when the excitation winding voltage is fixed. Combining with the results shown in Fig. 4.6, the load characteristics of the standalone TSCAOI configured generator can be comprehensively illustrated.

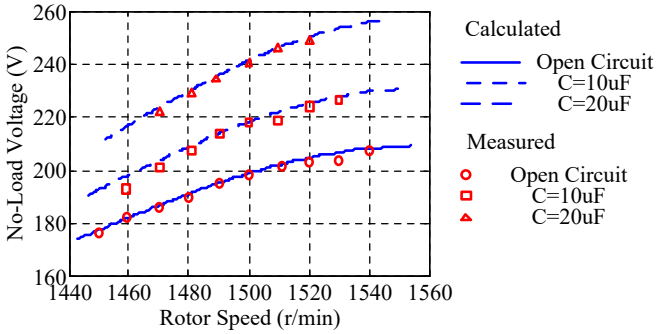

Fig. 4.10 Variations of the no-load voltage with the changing rotor speeds

4.4. Excitation Characteristics

The simulated and experimental variations of the no-load excitation winding currents with the changing rotor speeds for three different compensation capacitors are shown in Fig. 4.11, when the excitation winding voltage is fixed at 135V/50Hz. The good agreements between the simulated and experimental results convincingly indicate that the proposed unified equivalent circuits are accurate and can be used at the design stage. As expected from (3.34), Fig. 4.11 shows that the no-load excitation winding current requirement is always minimum at the synchronous speed even though the generator is connected with different compensation capacitors. Furthermore, Fig. 4.11 indicates that the reactive power requirement of the generator can be effectively compensated by the compensation capacitor, connected to the power winding. From the investigation of the reactive power terms in (3.34), it is notable that the selected compensation capacitor should be as close as to $2/3\ \omega_s^2 L_m$, which is about 31.6uF in this case to effectively compensate the reactive power requirement and reduce the excitation winding current.

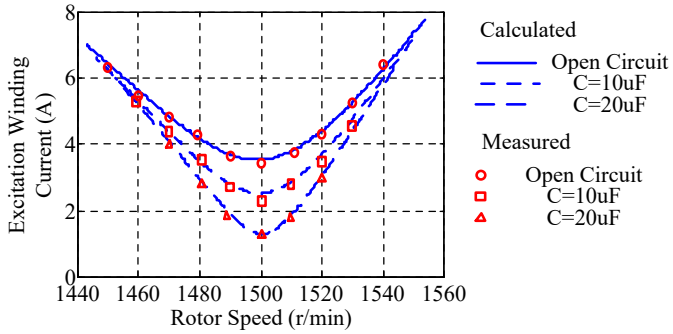

Fig. 4.11 Variations of the no-load excitation winding current with the changing rotor speeds and three different compensation capacitors

Fig. 4.12 shows the simulated variations of the excitation winding current of the generator with varying speeds and different resistive loads, when the load voltage was regulated at 230V/50Hz and a 20uF compensation capacitor is employed. According to (3.35), the excitation winding current is determined by the resistive load and operating speed, with the fixed compensation capacitors. In addition, as explained in Section 3.3.2, the excitation winding current for a given resistive load is always minimum at the operating speed, satisfying $s = -R_r/3R'_{load}$. The thicker blue line in Fig. 4.12 denotes the rotor speeds, satisfying $s = -R_r/3R'_{load}$, and the red circles denotes the experimental operating speeds, at which the

excitation winding current is minimum with the given resistive load. The good agreements between the theoretical and experimental results further indicate the validity of the theoretical analyses.

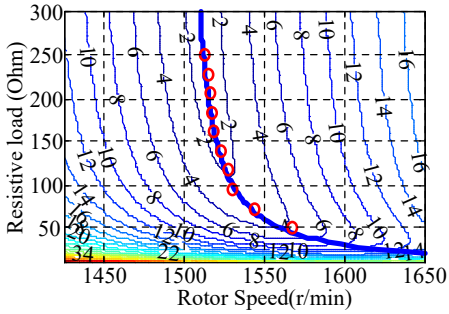

Fig. 4.12 Contours showing the variations of the excitation winding current with the changing loads and rotor speeds

4.5. Fluctuating Torque and VUF

The major drawback of the TSCAOI configured SCIG is its asymmetrical excitation and load arrangement. This asymmetrical arrangement will inevitably cause unbalanced operation of the generator, resulting in torque fluctuations. The fluctuating torque produces audible noise and mechanical vibrations, limiting not only the operating life but also the operating range of generator. The understanding of the mechanisms behind the fluctuating torque is therefore important.

Consistent with the assumption of the steady-state operation, the rotating vectors of the stator and rotor current symmetrical components can be written as:

$$\tilde{\imath}_{s+} = |\tilde{\imath}_{s+}|\cos(\omega_s t + \theta_{s+}) + j|\tilde{\imath}_{s+}|sin(\omega_s t + \theta_{s+}) \quad (4.1)$$

$$\tilde{\imath}_{s-} = |\tilde{\imath}_{s-}|\cos(\omega_s t + \theta_{s-}) + j|\tilde{\imath}_{s-}|sin(\omega_s t + \theta_{s-}) \quad (4.2)$$

$$\tilde{\imath}_{r+} = |\tilde{\imath}_{r+}|\cos(\omega_s t + \theta_{r+}) + j|\tilde{\imath}_{r+}|sin(\omega_s t + \theta_{r+}) \quad (4.3)$$

$$\tilde{\imath}_{r-} = |\tilde{\imath}_{r-}|\cos(\omega_s t + \theta_{r-}) + j|\tilde{\imath}_{r-}|sin(\omega_s t + \theta_{r-}) \quad (4.4)$$

Where $|\tilde{\imath}_{s+}|$, $|\tilde{\imath}_{s-}|$, $|\tilde{\imath}_{r+}|$ and $|\tilde{\imath}_{r-}|$ are the amplitudes of the corresponding vector quantities, and θ_{s+}, θ_{s-}, θ_{r+} and θ_{r-} are their phase angles, referring to the α axis. It can be noted that all of these variables are determined by the operating conditions and system

parameters. Substituting (4.1), (4.2), (4.3) and (4.4) into (3.12) and taking the real parts, gives the steady-state values of the stator and rotor currents in the α- and β-axis as:

$$i_{se} = |\tilde{\imath}_{s+}|\cos(\omega_s t + \theta_{s+}) + |\tilde{\imath}_{s-}|\cos(\omega_s t + \theta_{s-}) \tag{4.5}$$

$$i'_{so} = |\tilde{\imath}_{s+}|sin(\omega_s t + \theta_{s+}) - |\tilde{\imath}_{s-}|sin(\omega_s t + \theta_{s-}) \tag{4.6}$$

$$i'_{r\alpha} = |\tilde{\imath}_{r+}|\cos(\omega_s t + \theta_{r+}) + |\tilde{\imath}_{r-}|\cos(\omega_s t + \theta_{r-}) \tag{4.7}$$

$$i'_{r\beta} = |\tilde{\imath}_{r+}|sin(\omega_s t + \theta_{r+}) - |\tilde{\imath}_{r-}|sin(\omega_s t + \theta_{r-}) \tag{4.8}$$

Substituting (4.5), (4.6), (4.7) and (4.8) into (3.9) gives the steady-state electromagnetic torque as

$$\begin{aligned} T_e = \frac{P}{2} L_m (&|\tilde{\imath}_{s+}||\tilde{\imath}_{r+}|\, sin(\theta_{s+} - \theta_{r+}) - |\tilde{\imath}_{s-}||\tilde{\imath}_{r-}|\, sin(\theta_{s-} - \theta_{r-}) \\ &+ |\tilde{\imath}_{s+}||\tilde{\imath}_{r-}|\, sin(2\omega_s t + \theta_{s+} + \theta_{r-}) \\ &- |\tilde{\imath}_{s-}||\tilde{\imath}_{r+}| sin\,(2\omega_s t + \theta_{s-} + \theta_{r+})) \end{aligned} \tag{4.9}$$

As shown by (4.9), the time-invariant average torque is produced by the first two terms, in which the stator and rotor currents have the same phase sequence. In contrast, the time-variant torque fluctuating at the frequency of $2\omega_s$ is produced by the last two terms, in which the stator and rotor currents have opposite phase sequence.

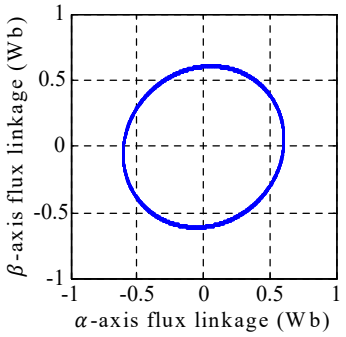

Fig. 4.13 The trajectory of the stator flux at 300W load and 1550 RPM rotor speed

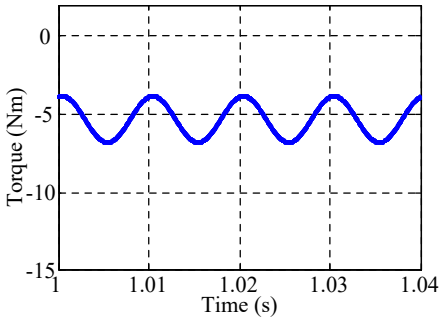

Fig. 4.14 The instantaneous electromagnetic torque at 300W load and 1550 RPM rotor speed

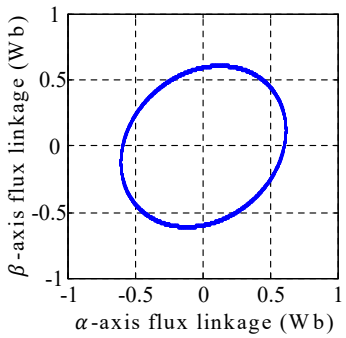

Fig. 4.15 The trajectory of the stator flux at 300W load and 1580 RPM rotor speed

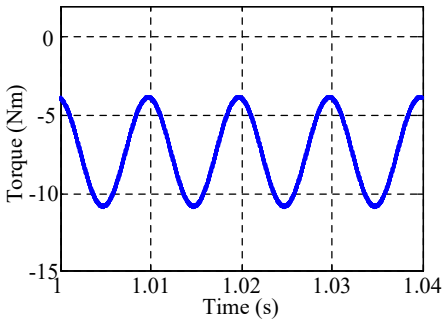

Fig. 4.16 The instantaneous electromagnetic torque at 300W load and 1580 RPM rotor speed

Fig. 4.13 and Fig. 4.15 show the trajectory of the stator flux simulated using MATLAB/Simulink, when the generator is operated under different operating conditions. As evident, the trajectory of the stator flux is elliptical because of the unbalanced operation of the generator. The simulated instantaneous electromagnetic torques of the generator, which are fluctuating at twice the synchronous frequency, are shown in Fig. 4.14 and Fig. 4.16.

The electromagnetic torque, given in (4.9), is hard to manipulate. However, as mentioned in Chapter 2, the VUF and CUF are widely used for evaluating the approximate level of torque fluctuations. Fig. 4.17 shows the simulated variations of the torque fluctuation amplitude with different rotor speeds and resistive loads when a 20uF compensation capacitor is connected, while the simulated VUF and CUF variations are shown in Fig. 4.18 and Fig. 4.19, respectively.

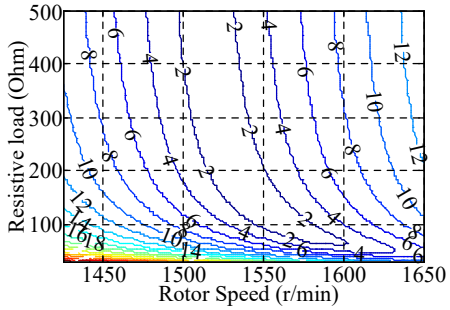

Fig. 4.17 Variations of the amplitude of the fluctuating torque with the changing loads and rotor speeds

An approximate linear relationship between the amplitude of the torque fluctuation and VUF can be observed from Fig. 4. 17 and Fig. 4.18. The VUF can therefore effectively measure the level of the torque fluctuations, therefore becomes an important indicator to evaluate the performance of the generator. However, from Fig. 4.19, it can be noted that CUF is not a good

measure to evaluate the level of torque fluctuations, comparing with VUF. This is because the negative sequence stator current is not always smaller than the positive sequence stator current, making the CUF even greater than 1, especially when the generator is operated at sub-synchronous speeds.

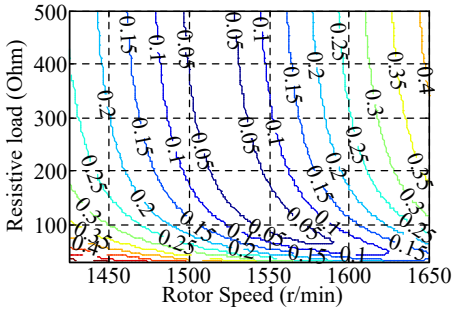

Fig. 4.18 Variations of VUF with the changing loads and rotor speeds

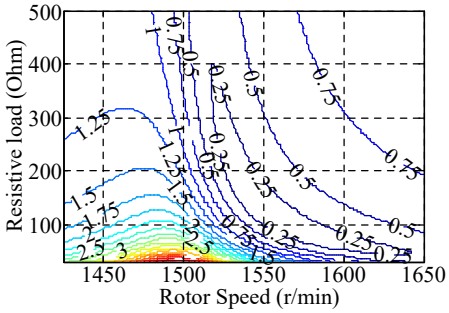

Fig. 4.19 Variations of CUF with the changing loads and rotor speeds

4.6. Selection of 3-phase SCIMs for TSCAOI Configuration

The machine parameters of the conventional 3-phase SCIM vary considerably, based on their power ratings, efficiency classes, rotor materials, application, operating environmental and cooling method. By linking the torque fluctuations and using VUF, it is possible to develop a guideline to select a 3-phase SCIM, which produces relatively low torque fluctuation in the TSACOI winding configuration. With the help of obtained analytical equations, the guideline of selecting the values of both compensation capacitor and machine parameters is summarized as below:

C_{comp} : According to (3.35), in order to effectively compensate for the reactive requirement of the generator, C_{comp} should be as close as to $2/3\ \omega_s^2 L_m$,. However from the aspect of VUF, C_{comp} should be as close as to $1/3\ \omega_s^2 L_m$ to make the numerator of (3.27) as small as possible. In practise, C_{comp} will be selected between $1/3\ \omega_s^2 L_m$ and $2/3\ \omega_s^2 \mathrm{L_m}$, but must be closer to $1/3\ \omega_s^2 \mathrm{L_m}$ due to higher priority given for the VUF.

L_m: Since C_{comp} has to be close to $1/3\ \omega_s^2 L_m$, the value of L_m will therefore directly influence the denominator of (3.35). As the imaginary part of $2/Z_1$ is negative, the value of L_m should be as large as possible to reduce VUF.

R_s and R_r: the values of R_s and R_r should be selected to make the value of Z_1 as small as possible, namely $(3R_s - R_r)$ as small as possible, to reduce VUF.

L_{ls} and L_{lr}: the values of both L_{ls} and L_{lr} should be selected as small as possible to reduce VUF, according to (3.35).

4.7. Summary

Both the steady-state behaviour and performance of the standalone TSCAOI configured generator were discussed and investigated using simulations and experiments in this chapter, with the emphasis on its load and excitation characteristics. Both the simulated and experimental results are in good agreement, and prove the accuracy and effectiveness of the proposed equivalent circuit models. Moreover, the theoretical basis of the torque fluctuation of this generator was described by investigating its electromagnetic torque production in detail. To overcome the difficulties in manipulating the torque expression under unbalanced operating conditions, use of VUF was proposed to obtain the approximate level of the torque fluctuation. A guideline for selecting 3-phase SCIMs for TSCAOI winding configuration to achieve low torque fluctuations has been described.

Chapter 5

Grid Integration of TSCAOI Configured Generators

5.1. Introduction

Behaviour of 3-phase cage induction machines, operated in the TSCAOI winding configuration at variable speeds to generate single-phase electricity, has been investigated in detail for standalone renewable power generation systems. However, integration of TSCAOI configured 3-phase cage induction machines into single-phase distributed power system is yet to be investigated. This chapter therefore investigates the behaviour of the grid-connected TSCAOI generator, and proposes a control scheme for integrating the TSCAOI configured generators into the single-phase distributed power system.

Firstly, a steady-state model is presented to investigate the behaviour of the grid-connected TSCAOI generator. Secondly, the operating criterion is formulated for the grid-connected TSCAOI generators, considering the following three aspects, namely the grid-side power factor, the torque fluctuation and the operating voltages and currents of the machines. From the investigation of the proposed model, it is found that there exists mutual coupling among these three aspects of the proposed criterion. Moreover, the coupling makes it very difficult to operate the generator to fulfil the proposed criterion at variable speeds, using real-time computed excitation winding voltage. In order to overcome this issue, this chapter therefore proposes a look-up table (LUT) method, using pre-computed optimum excitation voltage at different operating speeds. Thirdly, to further simplify the overall system, a slip estimation method is proposed to enable speed-sensorless control of the generator. Finally, the validity of the proposed generator concept is verified through simulations, implementing the proposed model in MATLAB/Simulink and experimental evidence of a prototype generator in this chapter. Good agreement between simulated and experimental results under various operating conditions indicates that the generator can be successfully grid integrated by the

proposed control scheme and is suitable for applications, such as small-scale wind and micro-hydro distributed generation systems.

5.2. Mathematical Model

As derived in Chapter 3, the dynamic behaviour of the TSCAOI configured SCIM can be described by the following equations in the stationary $\alpha\beta$ frame, with the α-axis of the frame being aligned with the magnetic axis of the One Isolated (OI) winding:

$$\begin{bmatrix} v_{se} \\ v'_{so} \\ 0 \\ 0 \end{bmatrix} = \begin{bmatrix} R_s + (L_{ls} + L_m)p & 0 & L_m p & 0 \\ 0 & \frac{2}{3}R_s + (\frac{2}{3}L_{ls} + L_m)p & 0 & L_m p \\ L_m p & \omega_r L_m & \frac{2}{3}R_r + \left(\frac{2}{3}L_{lr} + L_m\right)p & \omega_r\left(\frac{2}{3}L_{lr} + L_m\right) \\ -\omega_r L_m & L_m p & -\omega_r\left(\frac{2}{3}L_{lr} + L_m\right) & \frac{2}{3}R_r + \left(\frac{2}{3}L_{lr} + L_m\right)p \end{bmatrix} \begin{bmatrix} i_{se} \\ i'_{so} \\ i'_{r\alpha} \\ i'_{r\beta} \end{bmatrix} \tag{5.1}$$

$$T_e = \frac{P}{2}L_m(i'_{so}i'_{r\alpha} - i_{se}i'_{r\beta}) \tag{5.2}$$

$$T_e - T_{ex} = \frac{2J}{P}\frac{d\omega_r}{dt} \tag{5.3}$$

In (5.1), p represents the differential operator d/dt, parameters R_s, L_{ls}, L_m, R_r and L_{lr} represent the stator resistance, the stator leakage inductance, the magnetizing inductance, the rotor resistance and the rotor leakage inductance of the 3-phase SCIM, respectively, and ω_r is the electrical angular frequency of the rotor in rad/s. The electromagnetic torque applied on the rotor shaft is given in (5.2), where *P* is the number of poles. The motion of the machine is described in (5.3) subsequently, where J is the rotor inertia in $kg \cdot m^2$, T_e is the electromagnetic torque, in Nm and T_{ex} is the external torque, applied on the rotor shaft, in *Nm*.

The steady-state voltage equations of the grid-connected TSCAOI configured generator can be readily obtained via replacing the differential operator p by $j\omega_{grid}$, where ω_{grid} is the grid angular frequency, and consequently expressed using phasor variables as:

$$\begin{bmatrix}\tilde{V}_{se}\\ \tilde{V}'_{so}\\ 0\\ 0\end{bmatrix}=\begin{bmatrix}R_s+j\omega_{grid}(L_{ls}+L_m) & 0 & j\omega_{grid}L_m & 0\\ 0 & \frac{2}{3}R_s+j\omega_{grid}(\frac{2}{3}L_{ls}+L_m) & 0 & j\omega_{grid}L_m\\ j\omega_{grid}L_m & \omega_r L_m & \frac{2}{3}R_r+j\omega_{grid}\left(\frac{2}{3}L_{lr}+L_m\right) & \omega_r\left(\frac{2}{3}L_{lr}+L_m\right)\\ -\omega_r L_m & j\omega_{grid}L_m & -\omega_r\left(\frac{2}{3}L_{lr}+L_m\right) & \frac{2}{3}R_r+j\omega_{grid}\left(\frac{2}{3}L_{lr}+L_m\right)\end{bmatrix}\begin{bmatrix}\tilde{I}_{se}\\ \tilde{I}'_{so}\\ \tilde{I}'_{r\alpha}\\ \tilde{I}'_{r\beta}\end{bmatrix} \tag{5.4}$$

The method of symmetrical components is also employed to develop the generalized steady-state equivalent circuit model that will be used to investigate the behaviour and performance of this grid-connected generator. By appropriately selecting the transformation matrix [$\boldsymbol{S}$] as:

$$[\boldsymbol{S}]=\begin{bmatrix}j & -j\\ 1 & 1\end{bmatrix} \tag{5.5}$$

The steady-state voltage equations in terms of the symmetrical components can be obtained as:

$$\begin{bmatrix}\tilde{V}_{s+}\\ \tilde{V}_{s-}\\ 0\\ 0\end{bmatrix}=$$

$$\begin{bmatrix}\frac{5}{6}R_s+\frac{5}{6}j\omega_{grid}L_{ls}+j\omega_{grid}L_m & -\frac{1}{6}R_s-\frac{1}{6}j\omega_{grid}L_{ls} & j\omega_{grid}L_m & 0\\ -\frac{1}{6}R_s-\frac{1}{6}j\omega_{grid}L_{ls} & \frac{5}{6}R_s+\frac{5}{6}j\omega_{grid}L_{ls}+j\omega_{grid}L_m & 0 & j\omega_{grid}L_m\\ j\omega_{grid}L_m & 0 & \frac{1}{s}\frac{2}{3}R_r+j\omega_{grid}(\frac{2}{3}L_{lr}+L_m) & 0\\ 0 & j\omega_{grid}L_m & 0 & \frac{1}{2-s}\frac{2}{3}R_r+j\omega_{grid}(\frac{2}{3}L_{lr}+L_m)\end{bmatrix}\begin{bmatrix}\tilde{I}_{s+}\\ \tilde{I}_{s-}\\ \tilde{I}_{r+}\\ \tilde{I}_{r-}\end{bmatrix} \tag{5.6}$$

where s is the slip. The positive sequence and negative sequence symmetrical components are denoted by subscripts $s+$ and $s-$, respectively.

The above equations can be represented by the steady-state equivalent circuit shown in Fig. 5.1.

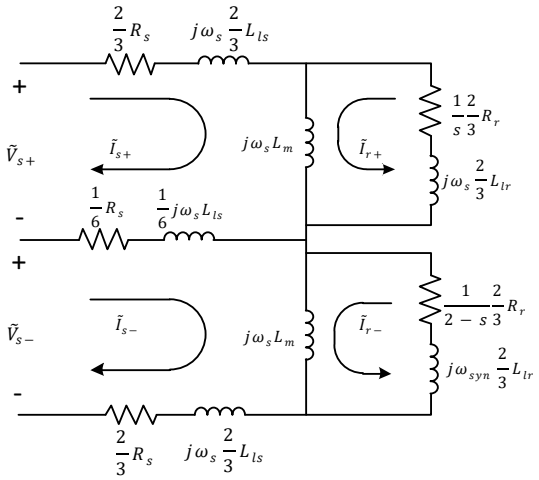

Fig. 5.1 The steady-state equivalent circuit of the grid-connected TSCAOI configured 3-phase SCIG

For clarity, let

$$Z_1 = \frac{5}{6}R_s + \frac{5}{6}j\omega_s L_{ls} + \frac{j\omega_s L_m(\frac{1}{s}\frac{2}{3}R_r + j\omega_s\frac{2}{3}L_{lr})}{\frac{1}{s}\frac{2}{3}R_r + j\omega_s(L_m + \frac{2}{3}L_{lr})} \tag{5.7}$$

$$Z_2 = -\frac{1}{6}R_s - \frac{1}{6}j\omega_s L_{ls} \tag{5.8}$$

$$Z_3 = \frac{5}{6}R_s + \frac{5}{6}j\omega_s L_{ls} + \frac{j\omega_s L_m(\frac{1}{2-s}\frac{2}{3}R_r + j\omega_s\frac{2}{3}L_{lr})}{\frac{1}{2-s}\frac{2}{3}R_r + j\omega_s(L_m + \frac{2}{3}L_{lr})} \tag{5.9}$$

With the impedances defined above, the steady-state equivalent circuit model shown in Fig. 5.1 can be accordingly simplified to the model shown in Fig. 5.2.

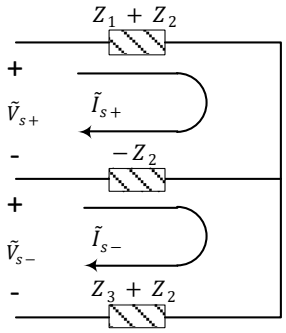

Fig. 5.2 Simplified steady-state equivalent circuit

The symmetrical components of the stator voltages can therefore be expressed in terms of the stator currents symmetrical components with newly defined impedances as:

$$\tilde{V}_{s+} = Z_1\tilde{I}_{s+} + Z_2\tilde{I}_{s-} \tag{5.10}$$

$$\tilde{V}_{s-} = Z_2\tilde{I}_{s+} + Z_3\tilde{I}_{s-} \tag{5.11}$$

The symmetrical components of the stator currents can be accordingly obtained by solving (5.10) and (5.11) simultaneously as:

$$\tilde{I}_{s+} = \left(Z_3\tilde{V}_{s+} - Z_2\tilde{V}_{s-}\right)/Z_m \tag{5.12}$$

$$\tilde{I}_{s-} = \left(Z_1\tilde{V}_{s-} - Z_2\tilde{V}_{s+}\right)/Z_m \tag{5.13}$$

where $Z_m = Z_1Z_3 - (Z_2)^2$.

Based on the inverse of the transformation matrix given in (5.5), the symmetrical components of stator voltages can be written as

$$\tilde{V}_{s+} = -\frac{j}{2}\tilde{V}_{se} + \frac{1}{2}\tilde{V}'_{so} \tag{5.14}$$

$$\tilde{V}_{s-} = \frac{j}{2}\tilde{V}_{se} + \frac{1}{2}\tilde{V}'_{so} \tag{5.15}$$

For simplicity, the referred power winding phasor voltage is fixed as reference to be $\tilde{V}'_{so} = V'_{so}\angle 0^o = V'_{so}$ where V'_{so} is the referred grid voltage amplitude; the excitation winding phasor voltage is represented in terms of its real and imaginary components as $\tilde{V}_{se} = V_{seR} +$

jV_{seI}, where V_{seR} and jV_{seI} denote the real part and the imaginary part of the excitation winding phasor voltage, respectively.

Accordingly, the phasors of the stator voltage symmetrical components, given in (5.14) and (5.15), can be further expressed, in terms of its real and imaginary components, as:

$$\tilde{V}_{s+} = \frac{1}{2}(V_{seI} + V'_{so}) - \frac{j}{2}V_{seR} \tag{5.16}$$

$$\tilde{V}_{s-} = \frac{1}{2}(V'_{so} - V_{seI}) + \frac{j}{2}V_{seR} \tag{5.17}$$

Substituting (5.16) and (5.17) into (5.12) and (5.13), the phasors of the stator current symmetrical components can be further given as:

$$\tilde{I}_{s+} = \frac{1}{2}\frac{Z_3}{Z_m}(V_{seI} + V'_{so} - jV_{seR}) - \frac{1}{2}\frac{Z_2}{Z_m}(V'_{so} - V_{seI} + jV_{seR}) \tag{5.18}$$

$$\tilde{I}_{s-} = \frac{1}{2}\frac{Z_1}{Z_m}(V'_{so} - V_{seI} + jV_{seR}) - \frac{1}{2}\frac{Z_2}{Z_m}(V_{seI} + V'_{so} - jV_{seR}) \tag{5.19}$$

Based on the transformation matrix $[\boldsymbol{S}]$, defined in (5.5), the current flowing through the power winding can be obtained as follows:

$$\begin{gathered}\tilde{I}'_{so} = \tilde{I}_{s+} + \tilde{I}_{s-} \\ = \frac{1}{2}\frac{Z_3}{Z_m}(V_{seI} + V'_{so} - jV_{seR}) + \frac{1}{2}\frac{Z_1}{Z_m}(V'_{so} - V_{seI} + jV_{seR}) - \frac{Z_2}{Z_m}V'_{so}\end{gathered} \tag{5.20}$$

In practice, a parallel compensation capacitor C_{comp} is employed to compensate the reactive power requirement of the generator, therefore the actual grid current can be represented as:

$$\tilde{I}_g = \mathrm{abs}(\tilde{I}_g)e^{j\theta_{grid}} = \tilde{I}'_{so}/\sqrt{3} + j\omega_s C_{comp}\tilde{V}_{so} \tag{5.21}$$

Where $\mathrm{abs}(\tilde{I}_g)$ represents the absolute value of the grid current phasor and θ_{grid} is the grid current phasor angle.

The grid voltage phasor, being the same as the power winding voltage phasor, is fixed as reference. Therefore, the power factor at the grid side can be obtained by calculating the cosine of the grid current phasor angle as:

$$\text{P. F.} = \cos\left(\theta_{grid}\right) \tag{5.22}$$

Likewise, this asymmetrical winding arrangement will also cause the unbalanced operation of the generator, leading to torque fluctuation. As described in the previous chapter, the difficulties in the manipulation of the fluctuating torque, make VUF and CUF widely adopted to approximate the level of torque fluctuation.

According to (5.16) and (5.17), the voltage unbalance factor (VUF), which is defined as the ratio of modulus of the negative-sequence to the positive-sequence components of the stator voltages, can be obtained as:

$$VUF = \left|\frac{\tilde{V}_{s-}}{\tilde{V}_{s+}}\right| = \left|\frac{(V_{seI} + V'_{so}) - jV_{seR}}{(V'_{so} - V_{seI}) + jV_{seR}}\right| \tag{5.23}$$

Similarly, according to (5.18) and (5.19), the current unbalance factor (CUF), which is defined as the ratio of modulus of the negative-sequence to the positive-sequence components of the stator currents, can be obtained as:

$$CUF = \left|\frac{\tilde{I}_{s-}}{\tilde{I}_{s+}}\right| = \left|\frac{Z_3(V_{seI} + V'_{so} - jV_{seR}) - Z_2(V'_{so} - V_{seI} + jV_{seR})}{Z_1(V'_{so} - V_{seI} + jV_{seR}) - Z_2(V_{seI} + V'_{so} - jV_{seR})}\right| \tag{5.24}$$

It can be noted in (5.23) and (5.24) that the VUF is independent of the system parameters; conversely, the CUF is dependent on the system parameters.

The steady-state torque production of the generator, with a specific excitation voltage, can be obtained through simulation, implementing the proposed mathematical model in MATLAB/Simulink. Then, the associated torque fluctuation amplitude can be readily calculated from the obtained torque production. By changing the real and imaginary part of the phasor of the excitation winding voltage respectively, the variations of the torque fluctuation amplitude with varying excitation voltages can be simulated.

A 3-kW, 4-pole 3-phase cage induction machine, with the parameters given in Appendix A, was configured in the TSCAOI winding arrangement for the following simulations. Fig. 5.3

shows the simulated variations of the torque fluctuation amplitude with changing excitation voltages, when slip = -0.06, $C_{comp} = 20uF$ and the grid voltage is fixed at 230V/50Hz.

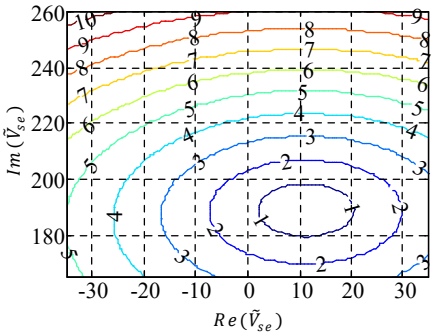

Fig. 5.3 Variations of the amplitude of the torque fluctuation with changing excitation voltages

Where the $Re(\tilde{V}_{se})$ and $Im(\tilde{V}_{se})$ are the imaginary and real part of the excitation winding phasor voltage respectively. As shown in Fig. 5.3, the torque fluctuation could be eliminated at a specific excitation voltage. In addition, it is noticeable that the larger the difference between the applied excitation voltage and this specific voltage, the larger the amplitude of the torque fluctuation will be.

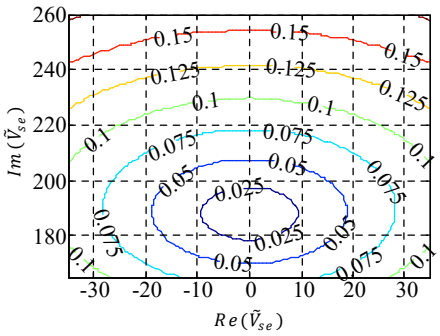

Fig. 5.4 Variations of VUF with changing excitation voltages

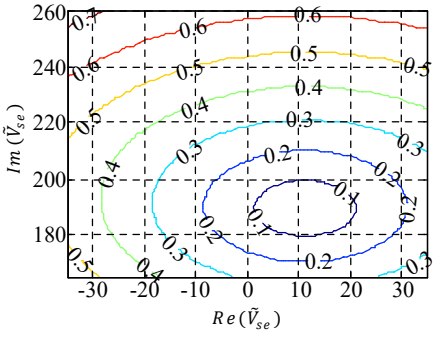

Fig. 5.5 Variations of CUF with changing excitation voltages

The variations of VUF and CUF with changing excitation voltages can be obtained through simulation in the similar way, implementing the (5.23) and (5.24) in MATLAB/Simulink respectively. The variations of VUF and CUF with changing excitation voltages are simulated, under the same operating conditions, and shown in Fig. 5.4 and Fig.

5.5, respectively. As evident, the CUF outperforms the VUF in approximating the level of torque fluctuations. Hence the CUF is selected to an indicator to represent the level of torque fluctuations approximately.

5.3. Determination of the Excitation Winding Voltage

In this section, the strategies for selecting the excitation winding voltage, which allows the generator to satisfy given criterion, is described. In order to demonstrate the viability of the proposed selection strategy, a 3-kW, 4-pole 3-phase cage induction machine, with the parameters given in Appendix A, was configured in the TSCAOI winding arrangement, as a prototype generator, for the following numerical analysis.

The formulation of the operating criterion mainly considers three aspects, namely the grid-side power factor, the torque fluctuation and the maximum operating voltage and current.

Firstly, for the grid-side power factor, it is desirable to provide power to the single-phase grid at near-unity power factor in a majority of application scenarios. Secondly, for the torque fluctuation, in order to minimize the audible noise and mechanical vibrations caused by it, the amplitude of the torque fluctuation must be limited. Although, the torque fluctuation is difficult to be manipulated mathematically, it has been proven that the CUF can effectively approximate the level of the torque fluctuation in the last section. Hence, the CUF will replace the torque fluctuation to be limited. Finally, both the maximum operating voltage and current must be limited, considering the machine ratings, operating conditions and operating range.

The detailed operating criterion for this prototype generator is proposed according to the considerations above and listed as following:

- Generating active power to the single-phase grid at near-unity power factor (Power factor < -0.98).
- Operating the generator with as small torque fluctuation as possible by maintaining the current unbalanced factor (CUF) under 0.05.
- The operating phase currents and voltages are limited within 8.5A and 300V respectively.

It is important to note that the operating criterion can be modified to suit different considerations, and is not limited only to the abovementioned.

From (5.22), (5.24) and (5.4), it can be noted that the grid-side power factor, the CUF and the operating currents are all only dependent on the operating speed and excitation voltage,

when the grid voltage and system parameters are fixed. However, it is still very difficult to regulate these three factors at the same time under variable speed conditions, using real-time computed excitation voltage. This chapter therefore proposed an approach, using the off-line method to pre-compute the optimum excitation voltages at different operating speeds. The obtained excitation voltages and corresponding speeds are stored in a two-dimensional (2-D) look-up table. This look-up table is used to provide the optimum excitation winding reference voltage according to different operating rotor speeds in practice.

The off-line computation mainly consists of two parts: firstly, selecting the excitation voltages, satisfying all the requirements included in the criteria, for different speeds respectively; then, using the average filtering algorithm to obtain the final excitation voltages applied for different speeds.

The detailed determination process of the excitation voltage is described as follows:

1) ***Selecting the excitation voltages to generate power to the grid at near-unity power factor for different rotor speeds respectively:***

The grid-side power factor can be calculated using (5.22), for different real and imaginary parts of the excitation winding phasor voltages, at any given rotor speed.

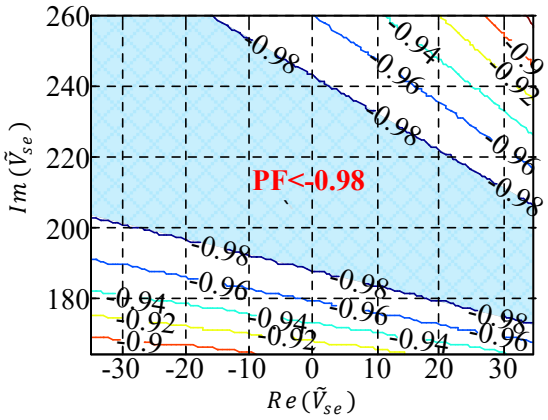

Fig. 5.6 The variations of the grid-side power factor (P.F.) with respect to different excitation voltages for slip = −0.06, C_{comp} = 20μF

Fig. 5.6 shows the grid-side power factor variations with varying excitation voltages, when slip = −0.06 and a 20μF compensation capacitor is connected with the power winding of the prototype generator in parallel. The blue shaded

region in Fig. 5.6 shows the collection of the excitation voltages that satisfy near-unity power factor generation at this particular speed. This process is repeated to obtain the excitation voltages, satisfying the near-unity power factor generation, for different speeds.

2) ***Selecting the excitation voltages to operate the generator with CUF smaller than 0.05 for different rotor speeds respectively:***

Similarly, the CUF can be calculated using (5.24), for different real and imaginary parts of the excitation winding phasor voltages at any given rotor speed.

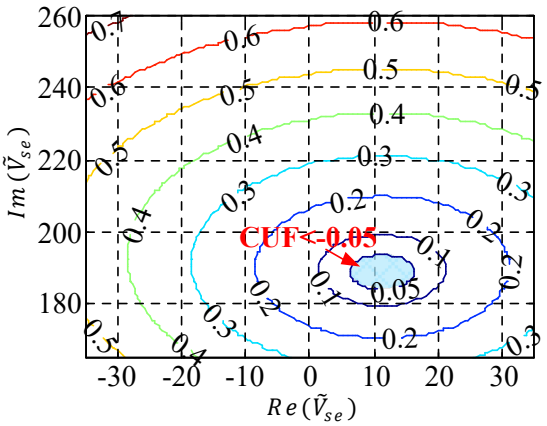

Fig. 5.7 The variations of the CUF with respect to different excitation voltages for slip = -0.06, C_{comp} = 20μF.

Fig. 5.7 illustrates the variations of the CUF with varying excitation winding voltage for slip = -0.06 and C_{comp} = 20μF. The collection of the excitation voltages which allow the CUF smaller than 0.05 at this particular speed is marked by blue shaded region. This process is repeated to obtain the excitation voltages, satisfying the CUF requirement, for different speeds.

3) ***Selecting the excitation voltages to operate the generator with its phase voltages and currents limited to specific values for different rotor speeds respectively:***

For the phase voltages, due to this particular winding arrangement, the excitation voltage is not allowed to exceed the grid voltage when minimizing the unbalanced operation of the generator. The requirement associated with the phase voltage is therefore easily satisfied.

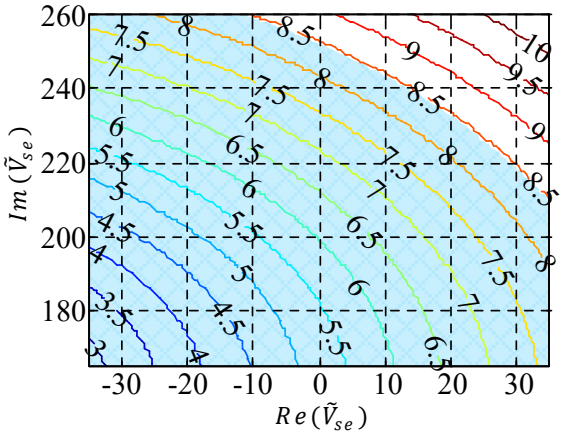

Fig. 5.8 The variations of the excitation winding current with respect to different excitation voltages for slip = -0.06, C_{comp} = 20μF.

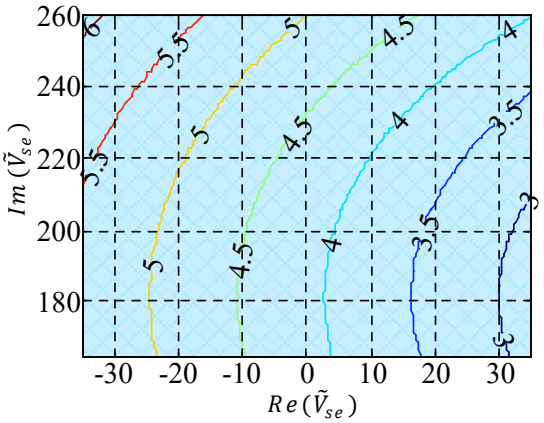

Fig. 5.9 The variations of the power winding current with respect to different excitation voltages for slip = -0.06, C_{comp} = 20μF.

For the phase currents, both the power winding current and the excitation winding current can be calculated using (5.4), for different real and imaginary parts of the excitation winding phasor voltage at any given rotor speed. Fig. 5.8 and Fig. 5.9 illustrate the variations of the excitation winding current and the power winding current with varying excitation winding voltage for slip = −0.06 and C_{comp} = 20μF, respectively. The collection of the excitation voltages which makes the excitation winding current and power winding current smaller than 8.5A are marked by blue shaded region, respectively in Fig. 5.8 and Fig. 5.9. As shown in Fig. 5.8 and Fig. 5.9, the power current is smaller than the excitation winding in

general. This is because the power winding has a greater number of turns, thus needs less current. Likewise, this process is repeated to obtain the excitation voltages, satisfying the phase voltages and currents requirements, for different speeds.

4) ***Selecting the collection of the excitation voltages which can operate the generator satisfying all the requirements included in the criteria for different rotor speeds respectively:***

Once the excitation voltages, allowing the generator to satisfy each individual requirement included in the criteria, are selected respectively for a specific speed, the excitation voltages which allow the generator to satisfy all the requirements in the criteria can be readily obtained. Likewise, this process is repeated to obtain the excitation voltages, satisfying all requirements included in the criteria, for different speeds.

5) ***Obtaining the final excitation voltages for different rotor speeds:***

Once the excitation voltages, allowing the generator to satisfy all the requirements in the criteria for a specific speed, are obtained, the final excitation voltage applied for this specific speed can be determined, using the average filtering algorithm, by:

$$Real(\tilde{V}_{se}^{*}) = \frac{sum(Real(\tilde{V}_{se_1}^{*}) + Real(\tilde{V}_{se_2}^{*}) + \cdots Real(\tilde{V}_{se_n}^{*}))}{n} \quad (5.25)$$

$$Imag(\tilde{V}_{se}^{*}) = \frac{sum(Imag(\tilde{V}_{se_1}^{*}) + Imag(\tilde{V}_{se_2}^{*}) + \cdots Imag(\tilde{V}_{se_n}^{*}))}{n} \quad (5.26)$$

Where, $\tilde{V}_{se}^{*}$ is the final excitation phasor voltage applied for this specific speed, $\tilde{V}_{se_1}^{*}$, $\tilde{V}_{se_2}^{*}$ …$\tilde{V}_{se_n}^{*}$ are the selected excitation phasor voltages which satisfy all the requirements included in the criteria, n is the total number of these selected voltages. $Real()$ and $Imag()$ denote the real part and imaginary part of the phasor respectively. Likewise, this process is repeated to obtain the final excitation voltages applied for different speeds. The final excitation voltages are represented in the form of the phasor. For the practical use, these phasor values will be transformed into the RMS values of the excitation winding voltages and the phase

difference between the excitation winding voltage and power winding voltage. These transformed values will be stored in the memory of the microprocessor as a look-up table. Fig. 5.10 and Fig. 5.11 show the final RMS value of the excitation voltage and the phase difference for different operating speeds respectively. As shown in Fig. 5.10 and Fig. 5.11, the variations of the excitation RMS voltage and the phase difference with the rotor speed are smooth, thus ensuring the data continuity and smoothness across the operating rotor speed.

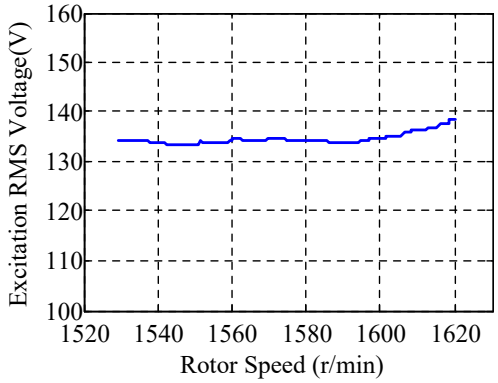

Fig. 5.10 The RMS values of the excitation voltages for different operating speeds.

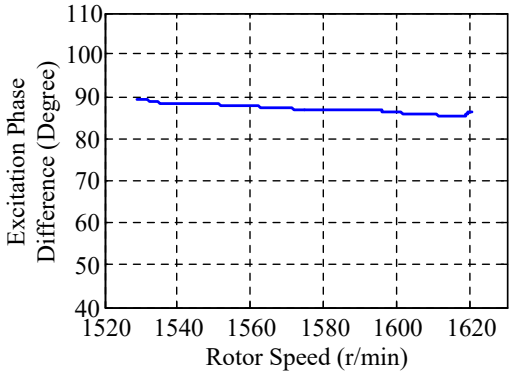

Fig. 5.11 The phase difference for different operating speeds.

5.4. Slip Estimation

As mentioned above, the operating speed of the generator is required to determine which excitation voltage that will be applied from the look-up table. Although the operating speed can be obtained directly by a speed sensor, it is undesirable because this causes degradation of reliability and adds extra cost. It is therefore quite necessary to propose a speed estimation

method. For the grid-connected TSCAOI configured generator, its synchronous angular frequency is fixed with the grid angular frequency, to allow the speed estimation to be transformed into slip estimation. Thus, in this section, a slip estimation method, which is based on the fast time domain symmetrical components decomposition algorithm, is presented, considering the cross coupling effects caused by the intrinsic asymmetry of the machine winding.

The space complex vector representation method, introduced in [130] for dynamic analysis of variable frequency ac drives, is used in this paper to simplify the derivations, and the machine variable represented in space complex vector can be given by:

$$\vec{X}(t) = X_\alpha(t) + jX_\beta(t) \tag{5.27}$$

Where X can represent any variable of the stator and rotor circuits, X_α and X_β are α and β components of the variable X in the stationary $\alpha\beta$ frame respectively and j is the imaginary unity. The $\vec{X}(t)$ can also be expressed by the summation of the positive and negative sequence components, as follows:

$$\vec{X}(t) = X_+(t)e^{j(\omega_s t+\theta_+)} + X_-(t)e^{-j(\omega_s t+\theta_-)} \tag{5.28}$$

In (5.28), subscripts $+ and -$ represent positive and negative sequence components, $X_+(t)$ and $X_-(t)$, which are assumed to vary slowly with time, are the magnitudes of the positive and negative sequence components respectively, ω_s is the synchronous angular frequency and θ_+ and θ_- are the corresponding phase angles. Equation (5.28) can be rewritten as below with γ/ω_s delay.

$$\vec{X}(t-\frac{\gamma}{\omega_s}) = X_+\left(t-\frac{\gamma}{\omega_s}\right)e^{j(\omega_s t+\theta_+)}e^{-j\gamma} + X_-\left(t-\frac{\gamma}{\omega_s}\right)e^{-j(\omega_s t+\theta_-)}e^{j\gamma} \tag{5.29}$$

When the delay angle γ is very small, above equation can be approximated as follows:

$$\vec{X}(t-\frac{\gamma}{\omega_s}) = X_+(t)e^{j(\omega_s t+\theta_+)}e^{-j\gamma} + X_-(t)e^{-j(\omega_s t+\theta_-)}e^{j\gamma} \tag{5.30}$$

Subtracting $\vec{X}(t)e^{j\gamma}$ from (5.30), equation below can be obtained.

$$\vec{X}\left(t-\frac{\gamma}{\omega_s}\right)-\vec{X}(t)e^{j\gamma}=-2jsin\gamma\cdot X_+(t)e^{j(\omega_s t+\theta_+)} \tag{5.31}$$

Thus

$$X_+(t)e^{j(\omega_s t+\theta_+)}=\frac{j}{2sin\gamma}\left[\vec{X}\left(t-\frac{\gamma}{\omega_s}\right)-\vec{X}(t)e^{j\gamma}\right] \tag{5.32}$$

Equation (5.32) is the decomposition equation of the positive sequence component from the original signals. The positive sequence component can be described in terms of α and β components as below by substituting (5.27) into (5.32).

$$\begin{aligned}X_+(t)e^{j(\omega_s t+\theta_+)}=&\frac{1}{2sin\gamma}\left[X_\beta(t)cos\gamma+X_\alpha(t)sin\gamma-X_\beta\left(t-\frac{\gamma}{\omega_s}\right)\right]\\&+\frac{j}{2sin\gamma}\left[X_\alpha\left(t-\frac{\gamma}{\omega_s}\right)-X_\alpha(t)cos\gamma+X_\beta(t)sin\gamma\right]\end{aligned} \tag{5.33}$$

The α and β axis positive sequence components can be readily obtained by (5.33) as below:

$$X_{\alpha+}(t)=\frac{1}{2}X_\alpha(t)-\frac{1}{2sin\gamma}\left[X_\beta\left(t-\frac{\gamma}{\omega_s}\right)-X_\beta(t)cos\gamma\right] \tag{5.34}$$

$$X_{\beta+}(t)=\frac{1}{2}X_\beta(t)+\frac{1}{2sin\gamma}\left[X_\alpha\left(t-\frac{\gamma}{\omega_s}\right)-X_\alpha(t)cos\gamma\right] \tag{5.35}$$

In the similar method, the negative sequence components in the $\alpha\beta$ frame can also be obtained as below:

$$X_{\alpha-}(t)=\frac{1}{2}X_\alpha(t)+\frac{1}{2sin\gamma}\left[X_\beta\left(t-\frac{\gamma}{\omega_s}\right)-X_\beta(t)cos\gamma\right] \tag{5.36}$$

$$X_{\beta-}(t)=\frac{1}{2}X_\beta(t)-\frac{1}{2sin\gamma}\left[X_\alpha\left(t-\frac{\gamma}{\omega_s}\right)-X_\alpha(t)cos\gamma\right] \tag{5.37}$$

From (5.34) to (5.37), it is noted that the smaller the time delay γ/ω_s is, the faster the response will be. However, the time delay γ/ω_s cannot be too small as it will then be susceptible to the noise.

The block diagrams for decomposing the positive and negative sequence components from original signals are illustrated in Fig. 12 and Fig. 13, respectively.

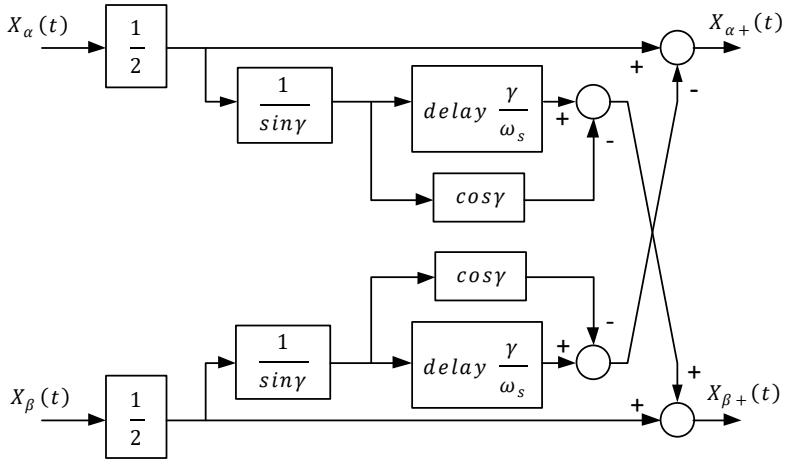

Fig. 5.12 The decomposition algorithm for positive sequence component

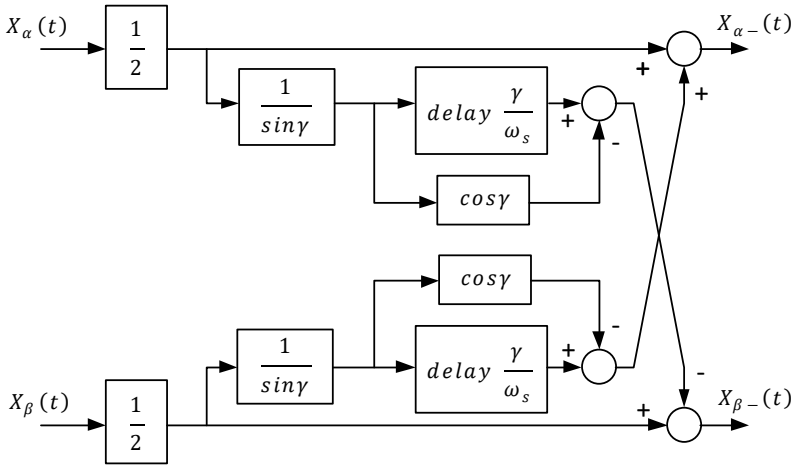

Fig. 5.13 The decomposition algorithm for negative sequence component

The symmetrical components obtained from the abovementioned method can be employed to estimate the operating slip. The proposed slip estimation strategy is performed in the reference frame fixed to the decoupled positive sequence component of the stator flux linkage. This reference frame is rotating at frequency ω_{s+}, which denotes the positive synchronous frequency, and the estimation is based on the positive sequence components only. The positive sequence components based rotor circuit equations in the positive synchronously

rotating frame can be directly derived from (5.1) in the stationary frame, due to the decoupled relationship between positive and negative sequence components in rotor circuits.

$$\frac{d\psi'^{+}_{rd+}}{dt} + \frac{2}{3}R_r i'^{+}_{rd+} - (\omega_{s+} - \omega_r)\psi'^{+}_{rq+} = 0 \tag{5.38}$$

$$\frac{d\psi'^{+}_{rq+}}{dt} + \frac{2}{3}R_r i'^{+}_{rq+} + (\omega_{s+} - \omega_r)\psi'^{+}_{rd+} = 0 \tag{5.39}$$

Where ψ'_r and i'_r represent the referred rotor flux linkage and rotor current respectively. The subscript $+$ represents the positive sequence components and superscript $+$ represents the components being evaluated in the positive synchronously rotating reference frame. The subscripts d and q are used to denote the direct and quadrature axis components in the reference frame respectively.

The positive sequence components of rotor currents in the positive synchronously rotating frame can also be written as

$$i'^{+}_{rd+} = \frac{1}{L_r}\psi'^{+}_{rd+} - \frac{L_m}{L_r}i^{+}_{sd+} \tag{5.40}$$

$$i'^{+}_{rq+} = \frac{1}{L_r}\psi'^{+}_{rq+} - \frac{L_m}{L_r}i^{+}_{sq+} \tag{5.41}$$

Where L_r equals $(2L_{lr}/3 + L_m)$. The rotor currents in (5.38) and (5.39) are inaccessible, they can be eliminated by substituting (5.40) and (5.41) into (5.38) and (5.39) respectively as

$$(1 + pT_r)\psi'^{+}_{rd+} - L_m i^{+}_{sd+} - T_r\omega_{slip}\psi'^{+}_{rq+} = 0 \tag{5.42}$$

$$(1 + pT_r)\psi'^{+}_{rq+} - L_m i^{+}_{sq+} + T_r\omega_{slip}\psi'^{+}_{rd+} = 0 \tag{5.43}$$

Where p denotes d/dt, ω_{slip} denotes the slip angular velocity and T_r equals $L_r/(2R_r/3)$. In (5.42) and (5.43), ψ'^{+}_{rd+} and ψ'^{+}_{rq+} are to be eliminated and replaced by ψ^{+}_{sd+} and ψ^{+}_{sq+}. According to equivalent circuit model proposed in Section 5.2, the ψ^{+}_{sd+} and ψ^{+}_{sq+} can be expressed as below. However, because of the intrinsic asymmetry of the stator circuit, ψ^{+}_{sd+} and ψ^{+}_{sq+} comprise terms resulting from the negative sequence components of stator currents.

$$\psi_{sd+}^{+} = \left(\frac{5}{6}L_{ls} + L_m\right) i_{sd+}^{+} + \frac{1}{6}L_{ls} i_{sd-}^{+} + L_m i'^{+}_{rd+} \tag{5.44}$$

$$\psi_{sq+}^{+} = \left(\frac{5}{6}L_{ls} + L_m\right) i_{sq+}^{+} - \frac{1}{6}L_{ls} i_{sq-}^{+} + L_m i'^{+}_{rq+} \tag{5.45}$$

The subscript $-$ represents the negative sequence components, and the terms arising from the negative sequence components should be eliminated as only the positive sequence components of the stator currents has a direct concern in positive sequence components of rotor flux linkages production.

The positive sequence components of the rotor flux linkages can be expressed as below:

$$\psi'^{+}_{rd+} = \frac{L_r}{L_m}\psi_{sd+,decoup}^{+} + (L_m - \frac{L_r L_s}{L_m}) i_{sd+}^{+} \tag{5.46}$$

$$\psi'^{+}_{rq+} = \frac{L_r}{L_m}\psi_{sq+,decoup}^{+} + (L_m - \frac{L_r L_s}{L_m}) i_{sq+}^{+} \tag{5.47}$$

Where L_s equals $(5L_{ls}/6 + L_m)$, $\psi_{sd+,decoup}^{+}$ and $\psi_{sq+,decoup}^{+}$, which are the decoupled terms, can be written as below:

$$\psi_{sd+,decoup}^{+} = \left(\frac{5}{6}L_{ls} + L_m\right) i_{sd+}^{+} + L_m i'^{+}_{rd+} \tag{5.48}$$

$$\psi_{sq+,decoup}^{+} = \left(\frac{5}{6}L_{ls} + L_m\right) i_{sq+}^{+} + L_m i'^{+}_{rq+} \tag{5.49}$$

Substituting (5.46) and (5.47) into (5.43) obtains

$$(1 + pT_r)\psi_{sq+,decoup}^{+} = (1 + \sigma p T_r) L_s i_{sq+}^{+} - T_r \omega_{slip}(\psi_{sd+,decoup}^{+} - \sigma L_s i_{sd+}^{+}) \tag{5.50}$$

where $\sigma = 1 - L_m^2/L_s L_r$. With direct axis of the reference frame being fixed to the decoupled positive sequence component of the stator flux linkage, $\psi_{sq+,decoup}^{+} = 0$ and ω_{slip} can be therefore written as:

$$\omega_{slip} = \frac{(1 + \sigma p T_r) L_s i_{sq+}^{+}}{T_r(\psi_{sd+,decoup}^{+} - \sigma L_s i_{sd+}^{+})} \tag{5.51}$$

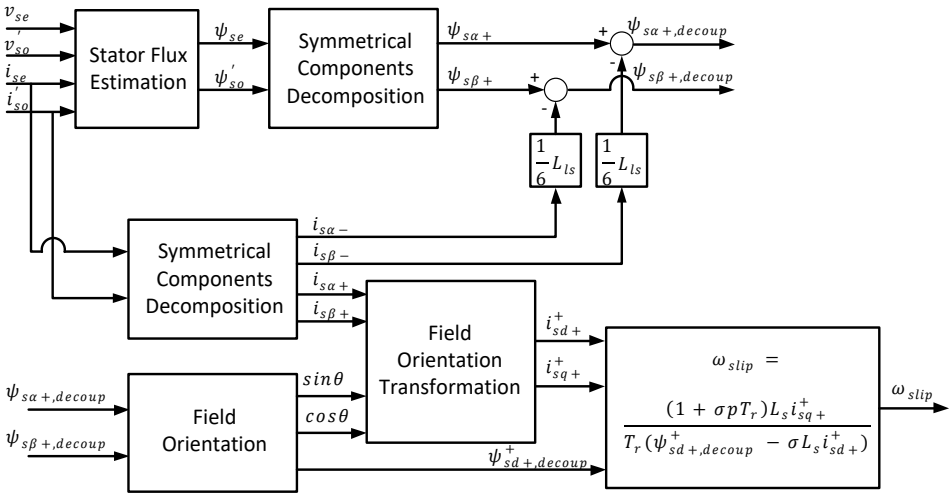

Fig. 5.14 Block diagram of the proposed slip estimation scheme

Fig. 5.14 shows the block diagram of the proposed slip estimation scheme, and the stator flux estimation can be easily realized by

$$\psi_{se} = \int (v_{se} - R_s i_{se})\, dt \tag{5.52}$$

$$\psi'_{so} = \int (v'_{so} - \frac{2}{3} R_s i'_{so})\, dt \tag{5.53}$$

Fig. 5.15 shows the simulated step response of the proposed slip estimation method. The estimated and real slip are in good accordance. Furthermore, the proposed slip estimation scheme shows a very good performance in settling and rising time.

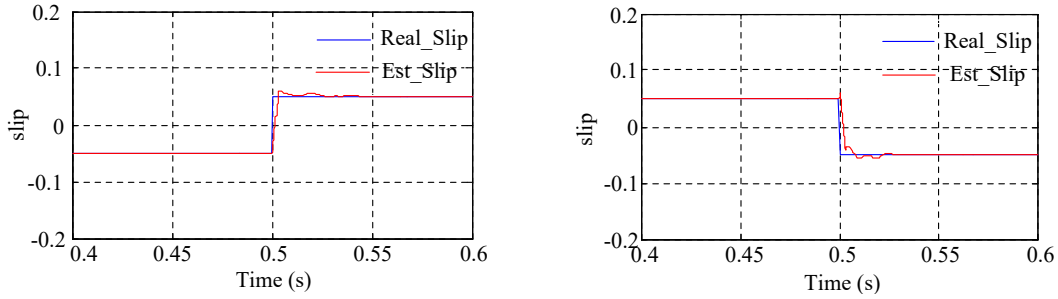

a *b*

Fig. 5.15 Step response of the slip estimation

5.5. TSCAOI Configured Single-Phase Grid-Connected Induction Generator

The block diagram of the TSCAOI-configured single-phase grid-connected induction generator is illustrated in Fig. 5.16. As shown in Fig. 5.16, the excitation winding of the TSCAOI configured generator is fed by the single-phase bi-directional converter and the power winding, constructed by the two series-connected windings, is connected with the single-phase AC grid. The measured winding currents and voltages are provided to the slip estimator to estimate the slip angular frequency. The estimated slip angular frequency or its equivalent rotor speed is fed into the pre-defined look-up table to select the reference voltage of the excitation winding. In order to generate the actual excitation voltage, besides the reference voltage, the grid phase angle θ_{grid} is also required, and it is obtained from the PLL (Phase-Locked Loop).

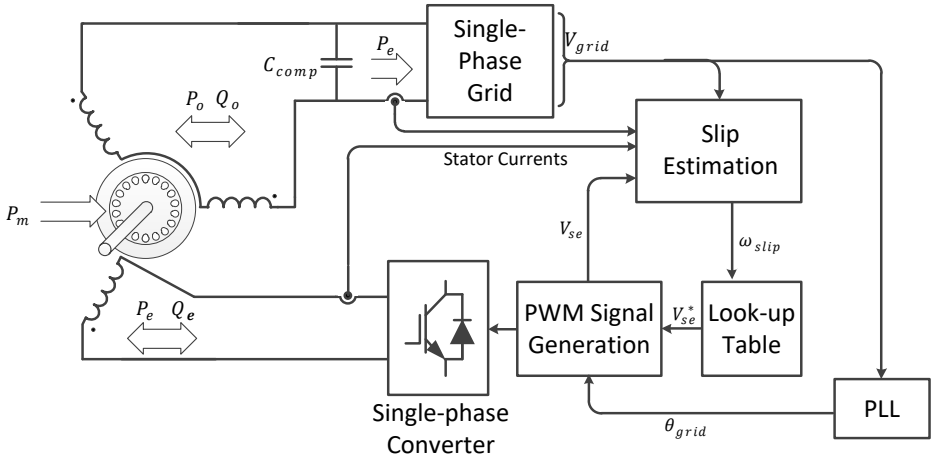

Fig. 5.16 Block diagram of the proposed control scheme for grid connected TSCAOI generator

5.6. Results and Discussion

In order to demonstrate the viability of the proposed control strategy and investigate both the behaviour and limitations of the grid-connected TSCAOI generator, simulations and experimental tests have been performed under various steady-state and transient conditions.

A four-pole 3 kW, 400V cage induction machine was configured in the TSCAOI winding arrangement for both simulations and experiments. The parameters of this cage induction machine are given in the Appendix A. Based on this prototype generator, a small-scale generation system was implemented on the experimental platform shown in Fig. 5.17.

In the experiment, the prototype generator was mechanically coupled with another induction machine controlled by a variable-speed drive (VSD) to emulate the variable-speed prime mover. The 230V/50Hz single-phase grid was connected with the power winding, and a single-phase voltage source converter (VSC) was connected with the excitation winding. The control software of the single-phase VSC was developed on a TI Delfino 28335 controller board. Voltage and current sensors were used to measure the grid voltage and the winding currents of the generator, respectively. The feedback signals of the grid voltage and the winding currents were read by the controller board through A/D (Analog to Digital) converter. The look-up table presented in Fig. 5.16 was stored in the controller board to select the proper excitation winding voltage. Based on the selected excitation winding reference voltage and grid phase angle, the PWM signals for the switches in the single-phase VSC were generated by the controller board, accordingly.

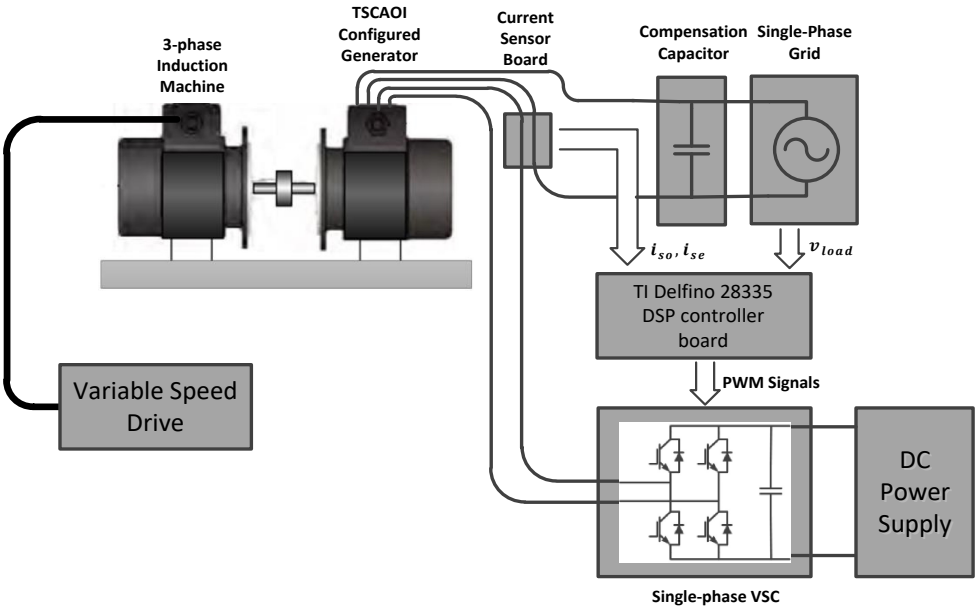

Fig. 5.17 Experimental setup

Before the detailed simulated and experimental investigation, the value of the compensation capacitor must be first determined. The compensation capacitor, connected with the single-phase grid in parallel, is used to reduce the reactive power requirement of the grid. Thus, it plays a vital role in correcting the grid-side power factor, and then has a significant impact on the system operating range.

Unlike the standalone TSCAOI configured generator, the operating range of the grid-connected TSCAOI configured generator is only determined by its speed range. The speed range can be indirectly obtained, using the determination method proposed for the excitation winding voltage in Section 5.3. For a given rotor speed, the determination method can find whether there exists an excitation voltage, allowing this prototype generator to satisfy the criteria described above, with a specific compensation capacitor. If there exists such an excitation voltage, this particular rotor speed is applicable for the generator; otherwise, this particular rotor speed is not applicable.

Fig. 5.18 illustrates the simulated operating speed range of the prototype generator with different compensation capacitors using the proposed criteria. According to Fig. 5.18, the 20uF capacitor providing the maximum operating range, was therefore selected.

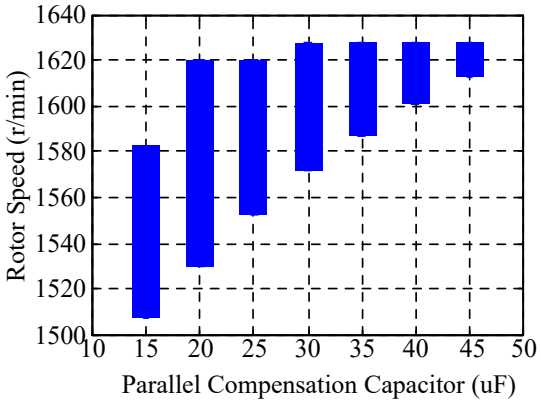

Fig. 5.18 The operating speed range for different parallel compensation capacitors

Fig. 5.19(a) and Fig. 5.19(b) show the variations in the steady-state currents of the excitation winding and power winding respectively with varying rotor speeds. As shown in Fig. 5.19, experimental and simulated results are in good agreement, and both excitation winding and power winding currents increase linearly with increasing rotor speeds. It is important to note that, the excitation winding current is proportional to the power winding current by a factor approximately equalling to $\sqrt{3}$, which is the turns ratio between the power winding and excitation winding, thus indicating the generator is operated with minimum unbalance.

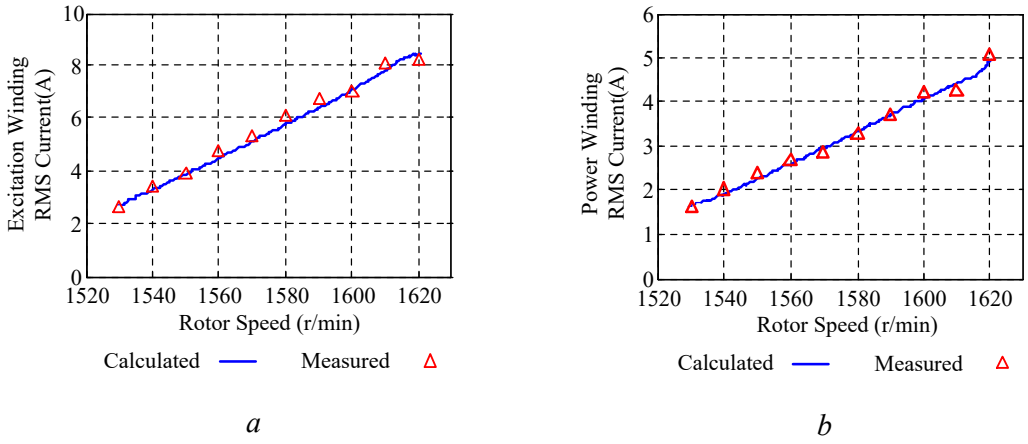

Fig. 5.19 (a) Excitation winding current and (b) power winding current vs rotor speeds

The variations in the active power provided by the excitation winding and power winding versus the rotor speeds are shown in Fig. 5.20(a) and Fig. 5.20(b), respectively. The negative power indicates that the active power is supplied by both power winding and excitation winding. Unlike the standalone TSCAOI configured generator, which can be operated both at sub- and super-synchronous rotor speeds, the grid-connected generator is limited to be operated at only super-synchronous speeds by the given operating criteria. Thus, the excitation winding keeps generating active power, and the generated power is fed back through the bi-directional converter to the energy storage system under all operating conditions. However, if the operating criterion is changed, the grid-connected generator is also able to operate at both sub- and super-synchronous rotor speeds and active power can also be provided from the converter side. The similar variations of the generated active power versus rotor speeds can be observed in Fig. 5.20(a) and Fig. 5.20(b), further indicating that the generator is operated with minimum unbalance. In addition, it is noticeable that the maximum generated active power is about 2kW, when the generator is operated at highest speeds.

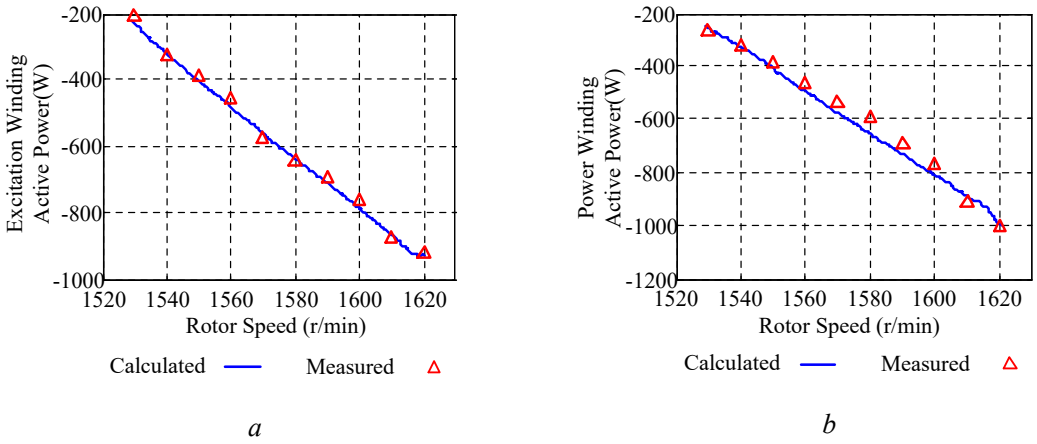

a *b*

Fig. 5.20 Active power generation of the (a) excitation winding and (b) power winding vs rotor speeds

Fig. 5.21(a) and Fig. 5.21(b), respectively, demonstrate the variations of the reactive power supplied by the power winding and excitation winding with different rotor speeds. As illustrated in Fig. 5.21, the reactive power requirements increase with the increasing rotor speeds. Furthermore, as expected, the presence of the compensation capacitor significantly reduces the reactive power requirement of the grid side. Meanwhile, as the generator is required to be operated with minimum unbalance, the reactive power consumed by the compensation capacitor, which is 332.2VA in this case, is approximately equal to the difference between the reactive power provided by the grid-side and converter-side.

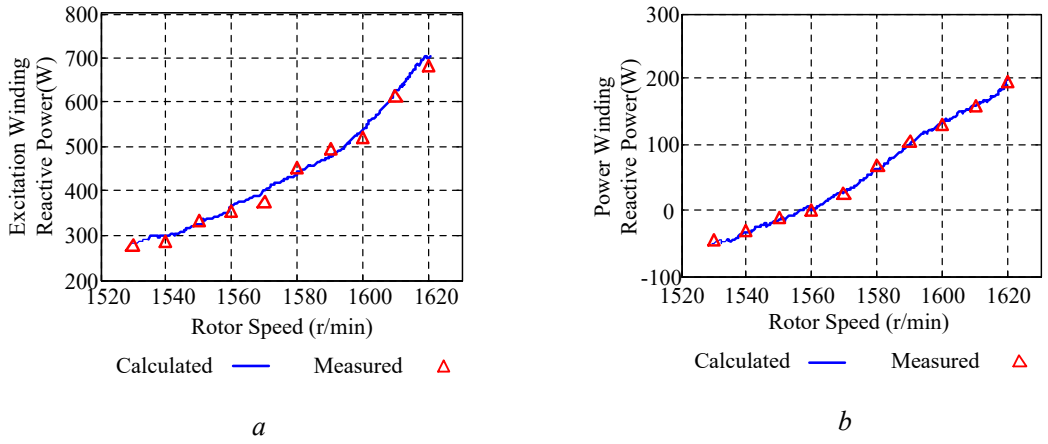

a *b*

Fig. 5.21 Reactive power generation of the (a) excitation winding and (b) power winding vs rotor speeds

Fig. 5.22(a) shows the variation of CUF with different rotor speeds. As shown in Fig. 5.22(a), the variation of CUF is strictly limited within the given range, which is 0 to 0.05 in this case. The small variations of CUF further indicate the generator is operated with minimum unbalance. It is interesting to note that the magnitude of unbalance is intensified when the operating speed approaches to the lowest and highest speed limitations. The variations of the power factor versus the rotor speeds are shown in Fig. 5.22(b). As shown in Fig. 5.22(b), the experimental and simulated results are also in good agreement and the power factor is well regulated below -0.98, ensuring that generated power is delivered to the grid with near unity power factor. However, the power factor becomes poor at the lowest and highest speeds. The performance of the proposed generator was also evaluated using the efficiency, as shown in Fig. 5.22(c). The small difference between the experimental and simulated results can be attributed to losses that were not included in the mathematical model. A maximum efficiency of approximately 90% was achieved when the generator was operated at the lowest rotor speeds with minimum load. However, as speed and load increase, the efficiency begins to decrease linearly to an approximately 80%.

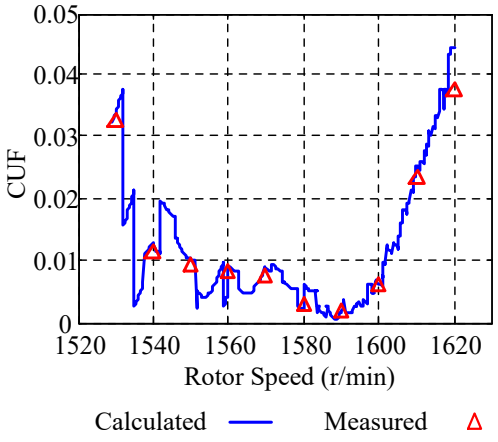

a

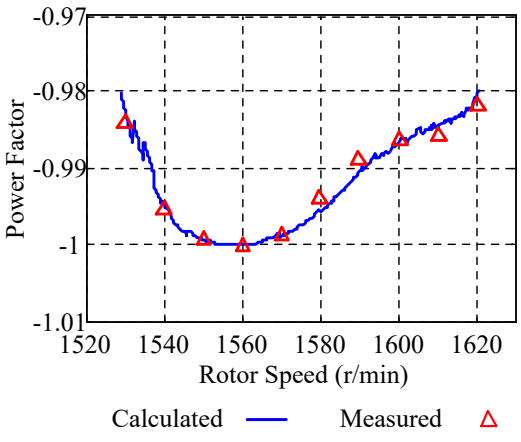

b

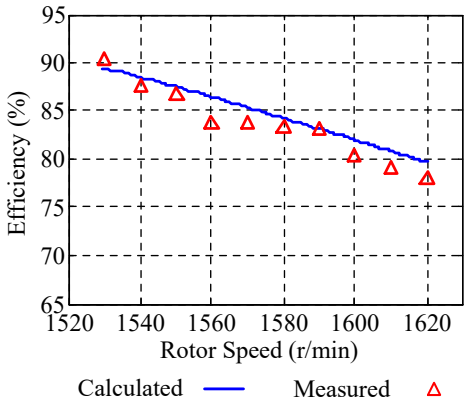

c

Fig. 5.22 (a) CUF, (b) power factor and (c) efficiency vs rotor speeds

Fig. 5.23 and Fig. 5.24 show the transient experimental waveforms of the grid voltage and current of the proposed single-phase grid-connected TSCAOI generator during the change of speed. The acceleration test results, which are shown in Fig. 5.23, were obtained by linearly increasing the rotor speed from 1540 rpm at 0.3s to 1600 rpm within 0.5s and the deceleration test results, shown in Fig. 5.24, were obtained by linearly decreasing the rotor speed from 1600 rpm at 0.3s to 1540 rpm within 0.5s. As can be seen, the system behaves as expected. Under the proposed control scheme, the grid current varies smoothly with the varying speeds and the power is still delivered to the grid at near unity power factor when the speed was changed.

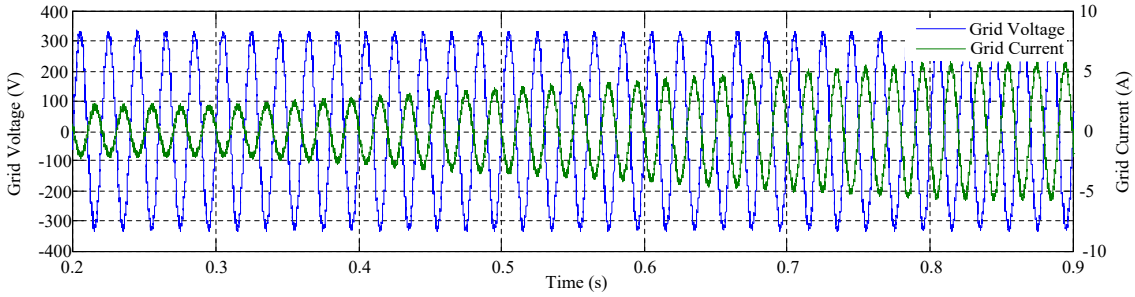

Fig. 5.23 Experimental transient waveforms of grid voltage and current at acceleration

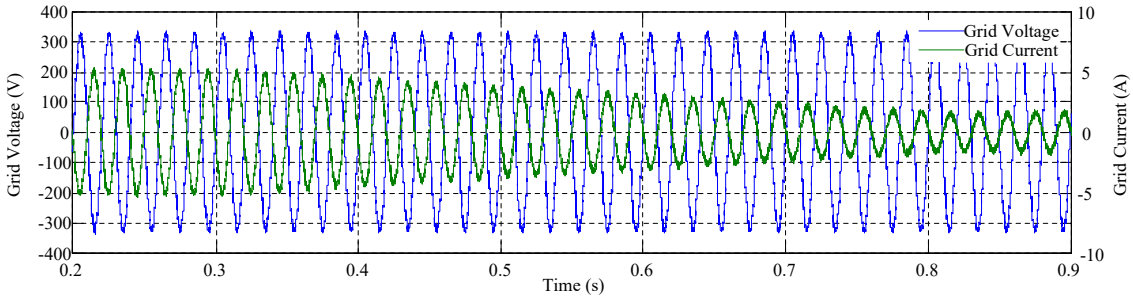

Fig. 5.24 Experimental transient waveforms of grid voltage and current at deceleration

5.7. Summary

A variable-speed grid-connected TSCAOI configured SCIG for single-phase electricity generation has been described in this chapter. A mathematical model has been proposed to investigate the behaviour and limitations of this grid-connected generator. A look-up table based control scheme has also been proposed to operate the generator under given operating conditions. To simplify the implementation of the proposed generator, a slip estimation method has been incorporated to the controller to achieve speed-sensorless control of this generator. The validity of the proposed generator concept has been verified by using both simulations and experimental evidence of a prototype generator. Both analytical and measured results indicate the proposed technique is viable and allows for variable-speed electricity generation at near unity power factor. The proposed generator, which is easy to be implemented and low in cost, is an ideal candidate for small-scale renewable energy distributed generation.

Chapter 6

Direct-Flux-Controlled NPC-TSCAOI Configured Generators for Standalone Applications

6.1. Introduction

Behaviour of the TSCAOI configured SCIG has been investigated in detail for both standalone and grid-connected applications. By using only a reduced–capacity converter, this technique provides a low-cost and small-sized solution for single-phase electricity generation. However, due to the lack of control degrees of freedom, the balanced operation condition and fast dynamic response are difficult to achieve.

This chapter therefore proposes a topological modification to the TSCAOI winding configuration to overcome this problem. The modified winding configuration, named NPC-TSCAOI (Neutral-Point-Connected TSCAOI) configuration, connects the neutral-point of the two series-connected winding to an additional converter leg, thus providing an additional control degree of freedom.

In addition, this chapter investigates the behaviour and control of the NPC-TSCAOI configured generator for standalone applications. Firstly, a dynamic mathematical model, which can accurately predict the behaviour of the standalone NPC-TSCAOI configured generator, is presented. With the help of this model, it is shown that, by directly controlling the modulus and rotating speed of the stator flux, the generator can provide well-regulated output voltage under balanced operating conditions. Secondly, a direct-flux-controlled (DFC) scheme is accordingly proposed. This control scheme enables balanced operation and fast transient response of the standalone NPC-TSCAOI configured generator, through directly regulating the modulus and rotating speed of the stator flux. Finally, the validity of the proposed generator concept is verified through simulations, implementing the proposed model in MATLAB/Simulink and experimental evidence of a prototype generator. Good agreement

between theoretical results and those obtained from the prototype NPC-TSCAOI generator under various operating conditions indicates that the generator can be successfully regulated by the proposed control scheme.

6.2. Dynamic Mathematical Model

The proposed NPC-TSCAOI configured SCIG is depicted in Fig. 6.1. As shown in Fig. 6.1, the NPC-TSCAOI winding configuration is evolved from the TSCAOI winding configuration. In order to provide more control degrees of freedom, the NPC-TSCAOI winding configuration connects the neutral-point of the two series-connected winding in the TSCAOI winding configuration to an additional converter leg.

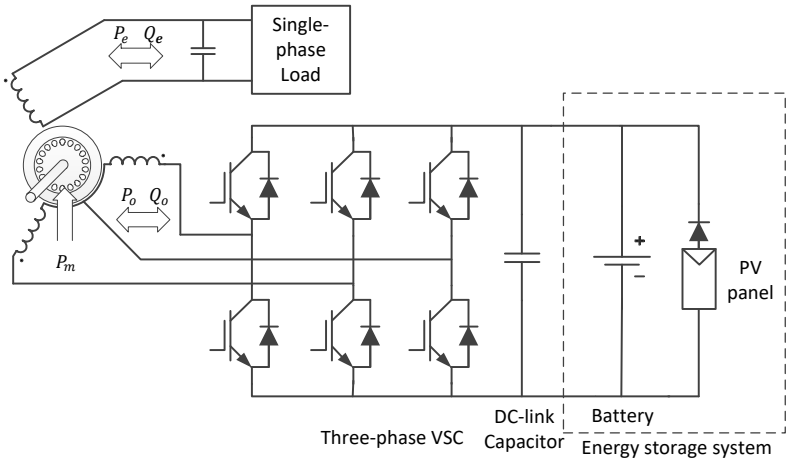

Fig. 6.1 The NPC-TSCAOI configuration for 3-phase SCIGs feeding single-phase load

The dynamic behaviour of the NPC-TSCAOI configured SCIG will be described in the stationary $\alpha\beta 0$ reference frame. Due to the presence of the additional leg, there will be a zero-sequence stator current. Thus, the zero-sequence component, indicated by the subscript 0, should be included. The stator and rotor $\alpha\beta 0$ variables can be directly determined from the *abc* variables by using the following power invariant transformation equation.

$$\begin{bmatrix} X_{\alpha s} \\ X_{\beta s} \\ X_{0s} \end{bmatrix} = \sqrt{\frac{2}{3}} \begin{bmatrix} 1 & -\frac{1}{2} & -\frac{1}{2} \\ 0 & \frac{\sqrt{3}}{2} & -\frac{\sqrt{3}}{2} \\ \frac{1}{\sqrt{2}} & \frac{1}{\sqrt{2}} & \frac{1}{\sqrt{2}} \end{bmatrix} \begin{bmatrix} X_{as} \\ X_{bs} \\ X_{cs} \end{bmatrix} \tag{6.1}$$

The variable X can be the stator or rotor voltage, current and flux linkage. For the squirrel cage rotor, there are no zero-sequence components. Thus, the rotor voltage $v_{\alpha r}$ and $v_{\beta r}$ are zero. Consequently, the dynamic model of the NPC-TSCAOI configured SCIG can be obtained in the stationary $\alpha\beta 0$ reference frame as follows:

For the stator:

$$v_{\alpha s} = R_s i_{\alpha s} + \frac{d\psi_{\alpha s}}{dt} \tag{6.2}$$

$$v_{\beta s} = R_s i_{\beta s} + \frac{d\psi_{\beta s}}{dt} \tag{6.3}$$

$$v_{0s} = R_s i_{0s} + \frac{d\psi_{0s}}{dt} \tag{6.4}$$

Where

$$\psi_{\alpha s} = (L_{ls} + L_m) i_{\alpha s} + L_m i_{\alpha r} \tag{6.5}$$

$$\psi_{\beta s} = (L_{ls} + L_m) i_{\beta s} + L_m i_{\beta r} \tag{6.6}$$

$$\psi_{0s} = L_{ls} i_{0s} \tag{6.7}$$

For the rotor

$$0 = R_r i_{\alpha r} + \frac{d\psi_{\alpha r}}{dt} + \omega_r \psi_{\beta r} \tag{6.8}$$

$$0 = R_r i_{\beta r} + \frac{d\psi_{\beta r}}{dt} - \omega_r \psi_{\alpha r} \tag{6.9}$$

where

$$\psi_{\alpha r} = (L_{lr} + L_m) i_{\alpha r} + L_m i_{\alpha s} \tag{6.10}$$

$$\psi_{\beta r} = (L_{lr} + L_m) i_{\beta r} + L_m i_{\beta s} \tag{6.11}$$

The electromagnetic torque and the electromechanical behaviour can be expressed by:

$$T_e = \frac{p}{2} L_m (i_{\beta s} i_{\alpha r} - i_{\alpha s} i_{\beta r}) \tag{6.12}$$

$$T_e - T_{ex} = \frac{2J}{P}\frac{d\omega_r}{dt} \tag{6.13}$$

Variables $v_{\alpha s}$, $v_{\beta s}$, v_{0s}, $i_{\alpha s}$, $i_{\beta s}$, i_{0s}, $\varphi_{\alpha s}$, $\varphi_{\beta s}$ and φ_{0s} represent the α, β and zero components of the stator voltages, currents and flux linkages respectively, and $i_{\alpha r}$, $i_{\beta r}$, $\varphi_{\alpha r}$ and $\varphi_{\beta r}$ represent the referred α and β components of the rotor currents and flux linkages. The variable ω_r denotes the instantaneous rotor angular speed in electrical radians per second. T_e and T_{ex} represent the electromagnetic torque and the load torque respectively. The model parameters R_s, R_r, L_{ls}, L_{lr}, L_m, J and P represent the stator and rotor resistances, the stator and rotor leakage inductances, the magnetizing inductance, the rotor inertia and the number of poles, and all these rotor quantities are referred to the stator circuit. Accordingly, the dynamic equivalent circuits of the NPC-TSCAOI configured SCIG in the stationary $\alpha\beta0$ reference frame can be shown as in Fig. 6.2.

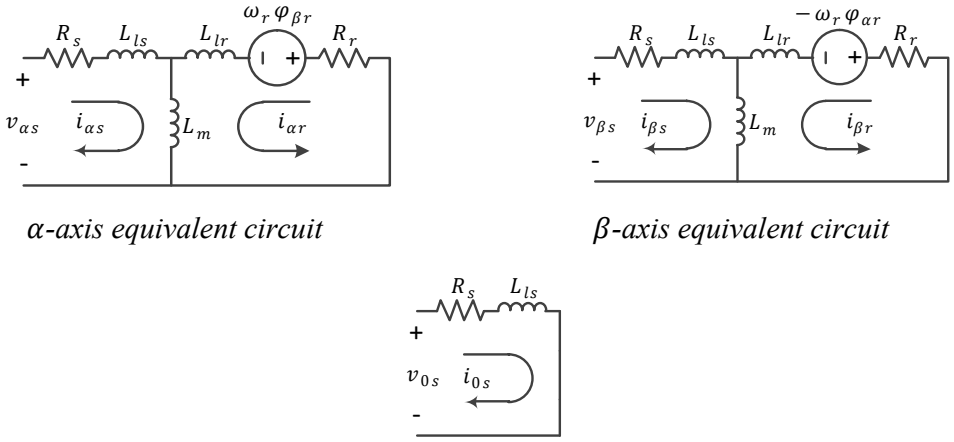

α-axis equivalent circuit

β-axis equivalent circuit

0-axis equivalent circuit

Fig. 6.2 The dynamic equivalent circuits of the NPC-TSCAOI configured 3-phase SCIG

6.3. Direct Flux Control

Assuming that stator flux vector $\vec{\Psi}_s = \psi_{\alpha s} + j\psi_{\beta s}$ rotates with an angular speed ω_s and its amplitude is kept constant at $\left|\vec{\Psi}_s^{\,*}\right|$, the stator flux vector can be expressed as

$$\vec{\Psi}_s = \left|\vec{\Psi}_s^{\,*}\right| e^{j\omega_s t} \tag{6.14}$$

The α and β components of the stator flux linkages can be obtained by using Euler's formula

$$\psi_{\alpha s} = \left|\vec{\Psi}_s^{\,*}\right| cos\,(\omega_s t) \tag{6.15}$$

$$\psi_{\beta s} = \left|\vec{\Psi}_s^{\,*}\right| sin\,(\omega_s t) \tag{6.16}$$

By using the Laplace transform of (6.8) and (6.9) and the relationship between the currents and flux linkages given by (6.5), (6.6), (6.10) and (6.11), and considering rotor flux has zero initial condition and rotor speed is kept constant, the relationship between stator and rotor flux linkage can be obtained as:

$$\begin{aligned}\psi_{\alpha r}(s) = {} & \frac{R_r L_m}{L_s L_r \sigma} \frac{\left(s + \frac{R_r}{L_r \sigma}\right)}{\left(s + \frac{R_r}{L_r \sigma}\right)^2 + (\omega_r)^2} \psi_{\alpha s}(s) \\ & - \frac{R_r L_m}{L_s L_r \sigma} \frac{\omega_r}{\left(s + \frac{R_r}{L_r \sigma}\right)^2 + (\omega_r)^2} \psi_{\beta s}(s)\end{aligned} \tag{6.17}$$

$$\begin{aligned}\psi_{\beta r}(s) = {} & \frac{R_r L_m}{L_s L_r \sigma} \frac{\omega_r}{\left(s + \frac{R_r}{L_r \sigma}\right)^2 + (\omega_r)^2} \psi_{\alpha s}(s) \\ & + \frac{R_r L_m}{L_s L_r \sigma} \frac{\left(s + \frac{R_r}{L_r \sigma}\right)}{\left(s + \frac{R_r}{L_r \sigma}\right)^2 + (\omega_r)^2} \psi_{\beta s}(s)\end{aligned} \tag{6.18}$$

where $L_s = L_{ls} + L_m$, $L_r = L_{lr} + L_m$ and $\sigma = 1 - L_m^2 / L_s\, L_r$ is the leakage factor.

By substituting the Laplace transform of (6.15) and (6.16) into (6.17) and (6.18) and taking the inverse Laplace transform, the α and β components of the rotor flux linkages in time domain can be obtained:

$$\begin{aligned}\psi_{\alpha r} = {} & x \left|\vec{\Psi}_s^{\,*}\right| \left[cos(\omega_s t) - e^{-\frac{R_r}{\sigma L_r} t}\, cos(\omega_r t)\right] \\ & - y \left|\vec{\Psi}_s^{\,*}\right| \left[sin(\omega_s t) - e^{-\frac{R_r}{\sigma L_r} t}\, sin(\omega_r t)\right]\end{aligned} \tag{6.19}$$

$$\psi_{\beta r} = y\left|\vec{\Psi}_s^{\,*}\right|\left[cos(\omega_s t) - e^{-\frac{R_r}{\sigma L_r}t}\, cos(\omega_r t)\right] + x\left|\vec{\Psi}_s^{\,*}\right|\left[sin(\omega_s t) - e^{-\frac{R_r}{\sigma L_r}t}\, sin(\omega_r t)\right] \tag{6.20}$$

where

$$x = \frac{L_m}{L_s}\frac{\cos\left(\arctan\left(\sigma(\omega_s - \omega_r)\, L_r/R_r\right)\right)}{\sqrt{1 + (\sigma(\omega_s - \omega_r)\, L_r/R_r)^2}} \tag{6.21}$$

$$y = -\frac{L_m}{L_s}\frac{\sin\left(\arctan\left(\sigma(\omega_s - \omega_r)\, L_r/R_r\right)\right)}{\sqrt{1 + (\sigma(\omega_s - \omega_r)\, L_r/R_r)^2}} \tag{6.22}$$

Thus, in the steady state, the α and β components of the rotor flux linkages are both sinusoidal and can be expressed as:

$$\psi_{\alpha r,ss} = M\left|\vec{\Psi}_s^{\,*}\right|\cos\left(\omega_s t - \theta\right) \tag{6.23}$$

$$\psi_{\beta r,ss} = M\left|\vec{\Psi}_s^{\,*}\right|\sin(\omega_s t - \theta) \tag{6.24}$$

where

$$M = \frac{L_m}{L_s}\frac{1}{\sqrt{1 + (\sigma(\omega_s - \omega_r)\, L_r/R_r)^2}} \tag{6.25}$$

$$\theta = \arctan\left(\sigma(\omega_s - \omega_r)\, L_r/R_r\right) \tag{6.26}$$

By substituting (6.15), (6.16), (6.23) and (6.24) into the dynamic model of the NPC-TSCAOI configured SCIG, the steady-state stator voltages $v_{\alpha s}$ and $v_{\beta s}$, and stator currents $i_{\alpha s}$ and $i_{\beta s}$ can be obtained as:

$$v_{\alpha s,ss} = \left|\vec{\Psi}_s^{\,*}\right|\left[A\cos(\omega_s t) - B\sin(\omega_s t)\right] \tag{6.27}$$

$$v_{\beta s,ss} = \left|\vec{\Psi}_s^{\,*}\right|\left[Asin(\omega_s t) + Bcos(\omega_s t)\right] \tag{6.28}$$

$$i_{\alpha s,ss} = \left|\vec{\Psi}_s^{\,*}\right|\left[C\cos(\omega_s t) - D\sin(\omega_s t)\right] \tag{6.29}$$

$$i_{\beta s,ss} = \left|\vec{\Psi}_s^{\,*}\right|\left[C\, sin(\omega_s t) + Dcos(\omega_s t)\right] \tag{6.30}$$

where

$$A = \frac{R_s}{\sigma L_s} - \frac{R_s L_m}{\sigma L_s L_r} M\cos(\theta) \tag{6.31}$$

$$B = \frac{R_s L_m}{\sigma L_s L_r} M sin(\theta) + 1 \tag{6.32}$$

$$C = \frac{1}{\sigma L_s} - \frac{L_m}{\sigma L_s L_r} M cos(\theta) \tag{6.33}$$

$$D = \frac{L_m}{\sigma L_s L_r} M sin(\theta) \tag{6.34}$$

In practice, it is assumed that the phase 'b' winding is used as the isolated power winding for single-phase electricity generation. The standalone resistive load R_{load} is directly connected across the power winding. Additionally, a compensation capacitor C_{comp} is commonly connected with the power winding in parallel to provide fixed reactive power to the generator. Thus, the external electrical relationship of the power winding can be expressed as below:

$$i_b(s) = -\frac{1 + sR_{load}C_{comp}}{R_{load}} v_b(s) \tag{6.35}$$

The voltage and current of the phase 'b' can be expressed by the corresponding $\alpha\beta 0$ components by taking the inverse transform of (1), thus

$$v_b = \sqrt{\frac{2}{3}}(-\frac{1}{2} v_{\alpha s,ss} + \frac{\sqrt{3}}{2} v_{\beta s,ss} + \frac{\sqrt{2}}{2} v_{0s}) \tag{6.36}$$

$$i_b = \sqrt{\frac{2}{3}}(-\frac{1}{2} i_{\alpha s,ss} + \frac{\sqrt{3}}{2} i_{\beta s,ss} + \frac{\sqrt{2}}{2} i_{0s}) \tag{6.37}$$

Based on (6.4) and (6.7), the zero sequence component of the stator voltages can be expressed by the zero component of the stator currents. By solving (6.35), (6.36) and (6.37) simultaneously, the steady-state zero component stator voltage v_{0s} can be obtained. Therefore, the steady-state generated output voltage can be calculated by substituting (6.27), (6.28) and v_{0s} into (6.36), and can be simplified as:

$$v_{out,ss} = G \left| \vec{\Psi}_s^{\,*} \right| \cos(\omega_s t + P) \tag{6.38}$$

Where, G and P are the functions of ω_s, ω_r and system parameters. It is evident that, by maintaining the rotating speed of the stator flux constant, the generated frequency will be kept constant, and by controlling the modulus of the stator flux, the amplitude of the output voltage will be regulated proportionally. This means that it is possible to obtain the output voltage control by regulating the rotating speed and the modulus of the stator flux, and this is the fundamental idea of the DFC scheme for the NPC-TSCAOI configured SCIG.

6.4. DFC of NPC-TSCAOI Configured SCIG

In the previous section, it has been proven that the generated single-phase voltage can be directly controlled by regulating the rotating speed and the modulus of the stator flux. Therefore, a control scheme of the direct flux controlled NPC-TSCAOI configured SCIG is shown in Fig. 6.3.

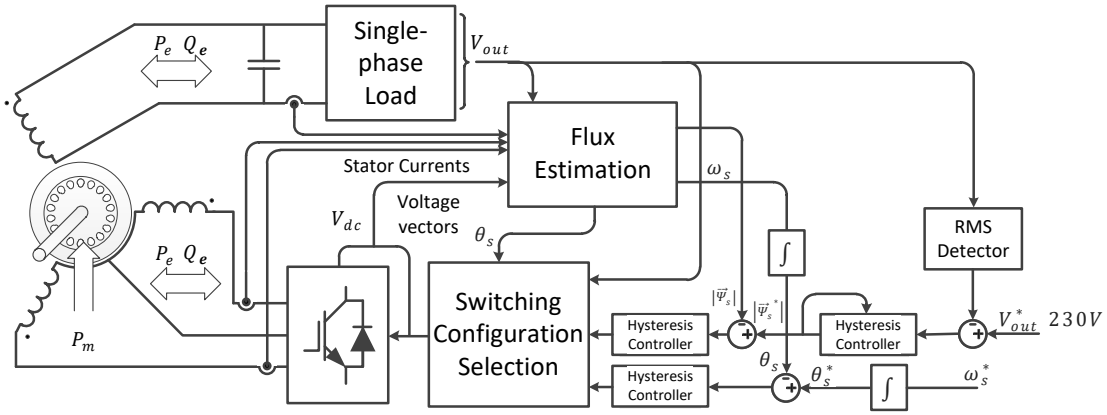

Fig. 6.3 Direct flux controlled standalone NPC-TSCAOI configured SCIG

The key components in the proposed scheme are the flux estimation block and switch configuration selection block. The flux estimation block estimates the instantaneous values of the stator flux using (6.2) and (6.3). The switch configuration selection block regulates the rotating speed and modulus of the stator flux by selecting the proper converter switching configuration, according to the difference between the reference and instantaneous value of the stator flux.

Due to the presence of the output voltage (phase '*b*' voltage), the control effects applied by the converter voltage switching space vector are disturbed. Thus, in order to compensate the

disturbance effects of the output voltage applied on the stator flux effectively, large DC-link voltage and small sampling period should be adopted.

There are six non-zero active voltage switching space vectors and two zero space vectors in the three-phase VSC shown in Fig. 6.1. These space vectors are depicted in Fig. 6.4. The corresponding eight switching configurations are shown in Fig. 6.5.

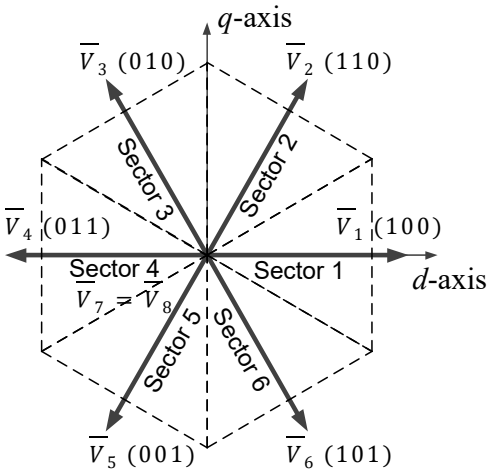

Fig. 6.4 Voltage switching space vectors of the three-phase VSC

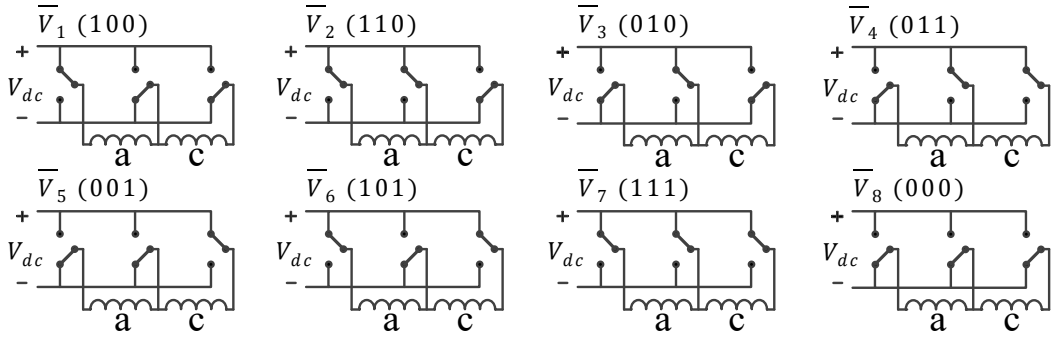

Fig. 6.5 Corresponding eight switching configurations

According to the principle of operation of DFC, the selection of the converter voltage space vectors applied at each sampling period is made to maintain the stator flux deviations within the limits of two hysteresis bands, shown in Fig. 6.6 and Fig. 6.7. The stator flux modulus hysteresis comparator, illustrated in Fig. 6.6, is used to regulate the amplitude of the output voltage. Because the direct use of the stator flux rotating speed regulator leads to the steady state error in the frequency of the output voltage, the frequency of the output voltage is therefore indirectly controlled by regulating the angle of the stator flux, as shown in Fig. 6.7.

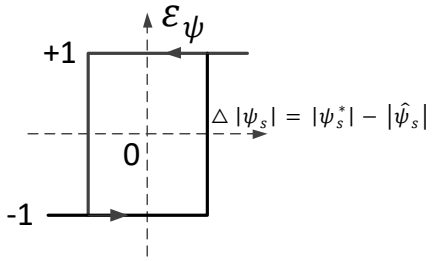

Fig. 6.6 Stator flux modulus hysteresis comparator

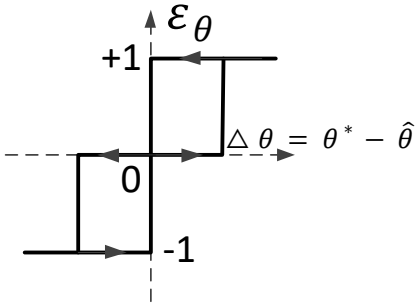

Fig. 6.7 Stator Flux angle hysteresis comparator

The desired reference of the modulus and the angle of the stator flux ($|\psi_s^*|\ and\ \theta^*$) are compared with the estimated values ($|\hat{\psi}_s|\ and\ \hat{\theta}$) respectively, and the resulting errors are fed into corresponding hysteresis-band comparators depicted in Fig. 6.6 and Fig. 6.7. As indicated in Fig. 6.6, if an increase in the stator flux modulus is required then output signal $\varepsilon_\psi = 1$, and if a decrease is required $\varepsilon_\psi = -1$. Also as indicated in Fig. 6.7, if an increase of the stator flux angle is required then the output signal $\varepsilon_\theta = 1$, if a decrease is required $\varepsilon_\theta = -1$, and if no change is required $\varepsilon_\theta = 0$.

Table. 6.1 Optimum voltage switching vector look-up table

$\boldsymbol{\varepsilon_\psi}$	$\boldsymbol{\varepsilon_\theta}$	**Sector 1**	**Sector 2**	**Sector 3**	**Sector 4**	**Sector 5**	**Sector 6**
1	1	$\overline{V}_2$	$\overline{V}_3$	$\overline{V}_4$	$\overline{V}_5$	$\overline{V}_6$	$\overline{V}_1$
	0	$\overline{V}_7$	$\overline{V}_8$	$\overline{V}_7$	$\overline{V}_8$	$\overline{V}_7$	$\overline{V}_8$
	-1	$\overline{V}_6$	$\overline{V}_1$	$\overline{V}_2$	$\overline{V}_3$	$\overline{V}_4$	$\overline{V}_5$
-1	1	$\overline{V}_3$	$\overline{V}_4$	$\overline{V}_5$	$\overline{V}_6$	$\overline{V}_1$	$\overline{V}_2$
	0	$\overline{V}_8$	$\overline{V}_7$	$\overline{V}_8$	$\overline{V}_7$	$\overline{V}_8$	$\overline{V}_7$
	-1	$\overline{V}_5$	$\overline{V}_6$	$\overline{V}_1$	$\overline{V}_2$	$\overline{V}_3$	$\overline{V}_4$

Except for the outputs of these comparators, the selection of the converter voltage space vectors also depends on the sector in which the stator flux lies. The six sectors, each $\pi/3$ wide, are indicated in Fig. 6.4. The switching configuration selection block shown in Fig. 6.3 receives the input signals ε_{ψ}, ε_{θ} and sector number, and then feeds the switching configuration to the VSC to generate the appropriate voltage switching space vector using the optimum voltage switching vector look-up table shown in Table. 6.1.

The desired stator flux modulus reference is obtained by the hysteresis controller shown in Fig. 6.8. First, in every cycle (0.02s for 50Hz), the desired output RMS voltage value is compared with the value obtained from the RMS detector, and the resulting error is fed into the hysteresis controller. As indicated in Fig. 6.8, if an increase in the output RMS voltage is required then $\varepsilon_{Vrms} = \triangle |\psi_s^*|$, which means the reference value of the stator flux modulus is increased by $\triangle |\psi_s^*|$, if the decrease of the output RMS voltage is required, then $\varepsilon_{Vrms} = -\triangle |\psi_s^*|$, which means the reference value of the stator flux modulus is decreased by $\triangle |\psi_s^*|$, if the output RMS voltage is within the hysteresis band, the reference value of the stator flux does not change.

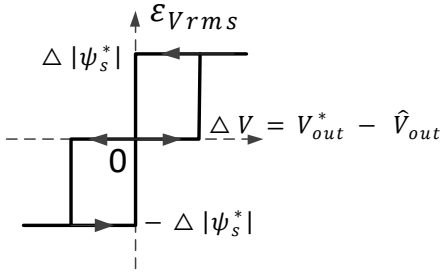

Fig. 6.8 Output voltage hysteresis comparator

6.5. Results and Discussion

In order to demonstrate the practical viability of the proposed concept and to investigate the behaviour and limitations of the single-phase NPC-TSCAOI configured generator, a comprehensive set of simulated and experimental tests have been performed under steady-state and transient conditions. A four-pole 3 kW 400V cage induction machine was configured in the NPC-TSCAOI winding arrangement for both theoretical simulations and experiments. The parameters of this cage induction machine are also given in the Appendix A. Based on this prototype machine, a small-scale single-phase generation system was implemented on the experimental platform, schematically shown in Fig. 6.9.

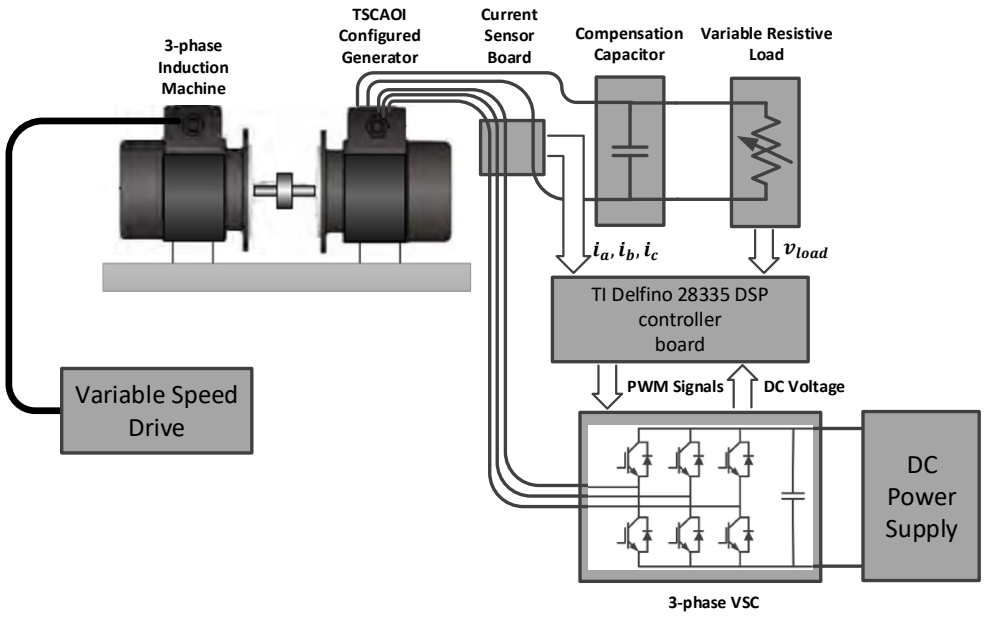

Fig. 6.9 Experimental setup

In the experiment, the prototype generator was mechanically coupled with another induction machine, which was controlled by a variable-speed drive (VSD) to emulate the variable-speed prime mover. A variable resistive load was directly connected with the power winding, and the generator was controlled by the 3-phase voltage source converter (VSC) to supply single-phase power to the standalone resistive load at 230V/50Hz. In order to overcome the disturbance caused by the load voltage, large DC-link voltage and small sample period should be employed in the proposed control scheme. Therefore, 800V DC-link voltage with 50 μs sample period was selected for the experiments.

The control software of the three-phase VSC was developed on a TI Delfino 28335 controller board. Voltage and current sensors were used to measure the load voltage and the winding currents of the generator, respectively. The feedback signals of the load voltage and the winding currents were read by the controller board through A/D (Analog to Digital) converter. Based on the proposed DFC scheme, the PWM signals for the switches in the 3-phase VSC were accordingly generated by the controller board.

Before detailed analysis, it is vital to determine the value of the compensation capacitor, which is connected with the power winding in parallel. By limiting the operating phase currents and voltages within 8.5A and 300V respectively, the practical operating range of the proposed generator was evaluated numerically for different compensation capacitors and a 45uF parallel-

connected compensation capacitor is selected with satisfactory operating range. The blue shaded area in Fig. 6.10 illustrates the possible operating range of the given NPC-TSCAOI configured generator with a 45uF compensation capacitor. The operating ranges of this prototype generator using different compensation capacitors are compared in the percentage bar graph illustrated in Fig. 6.11.

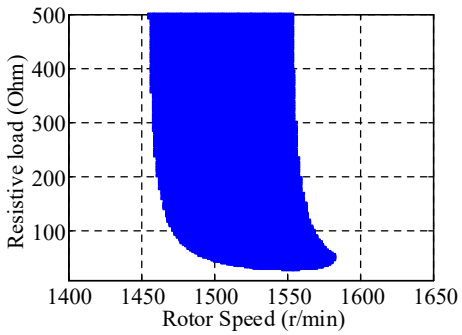

Fig. 6.10 Possible operating range with 45uF compensation capacitor

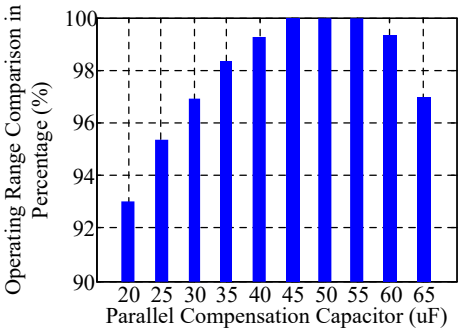

Fig. 6.11 Operating range comparison using different compensation capacitors

Fig. 6.12 (a), Fig. 6.12 (b) and Fig. 6.12 (c) give contour curves showing the variations of phase '*a*' RMS current, phase '*b*' RMS current and phase '*c*' RMS current with the changing loads and rotor speeds respectively. As shown in Fig. 6.12 (a) and Fig. 6.12 (b), both phase '*a*' current and phase '*b*' current increase with a deviation of the rotor speed from the synchronous speed (1500 r/min). Additionally, as the load voltage is regulated at 230V/50Hz for any speeds, the load current (phase '*b*' current) varies only with the changing loads, as shown in Fig. 6.12 (c).

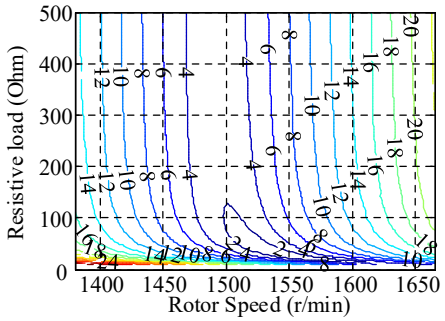

a

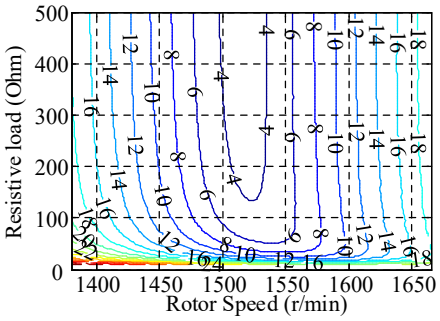

b

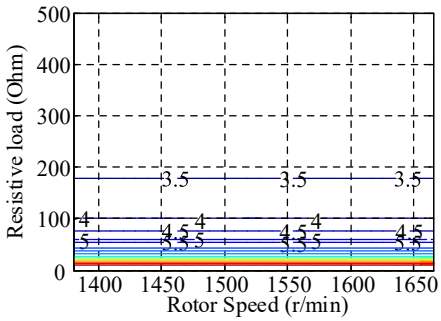

c

Fig. 6.12 Contours showing the variations of phase '*a*' current (a), phase '*b*' current (b) and phase '*c*' current (c) with the changing loads and rotor speeds

Fig. 6.13(a) and Fig. 6.13(b) present the contours showing the variations of phase '*a*' RMS voltage and phase '*c*' RMS voltage with changing loads and rotor speeds respectively.

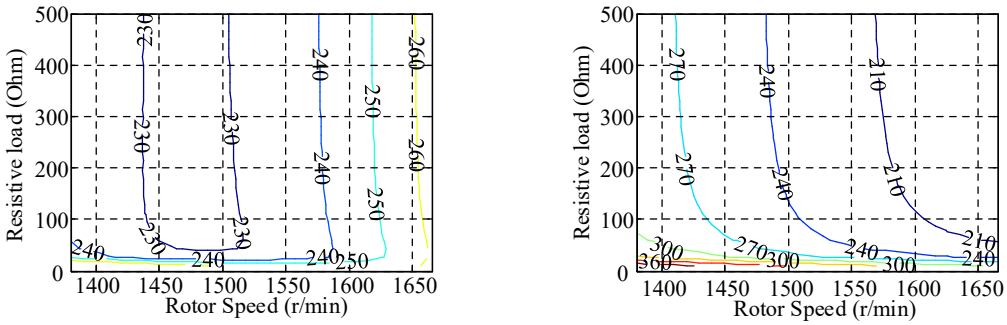

a *b*

Fig. 6.13 Contours showing the variations of phase a voltage (a) and phase c voltage (c) with the changing loads and rotor speeds

As shown in Fig. 6.13(a), the minimum phase '*a*' voltage is achieved at a rotor speed slightly below the synchronous speed, even when different resistive loads are connected. However, the phase '*c*' voltage decreases with an increase of rotor speeds and load resistance.

Fig. 6.14(a) and Fig. 6.14(b), respectively, demonstrate the variations of phase '*a*' and phase '*c*' currents with the rotor speed when three different resistive loads are connected. As evident, both experimental and simulated results are in agreement and exhibit the same trend. It is interesting to note that the variations of phase '*a*' current with loads is opposite to the variations of phase '*c*' current with loads, although there exists a unique rotor speed for certain loads, at which the currents are minimum.

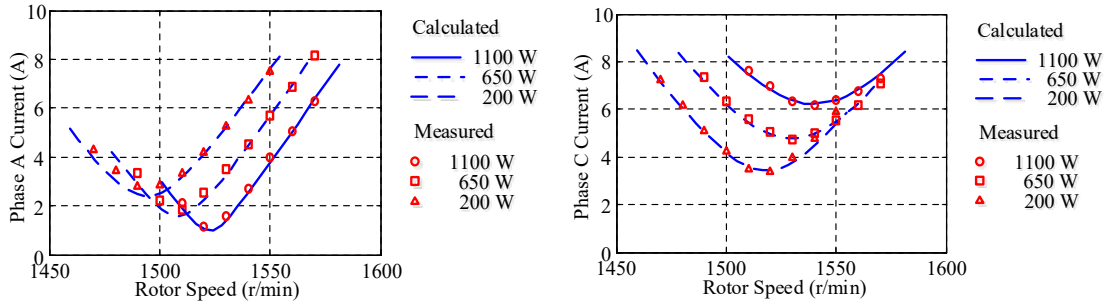

a *b*

Fig. 6.14 Variations of the phase '*a*' current (a) and phase '*c*' current (b) with the rotor speed when different loads are connected

The variations of the active power and reactive power provided by the excitation winding versus rotor speeds are illustrated in Fig. 6.15(a) and Fig. 6.15(b), respectively, when three different resistive loads are connected.

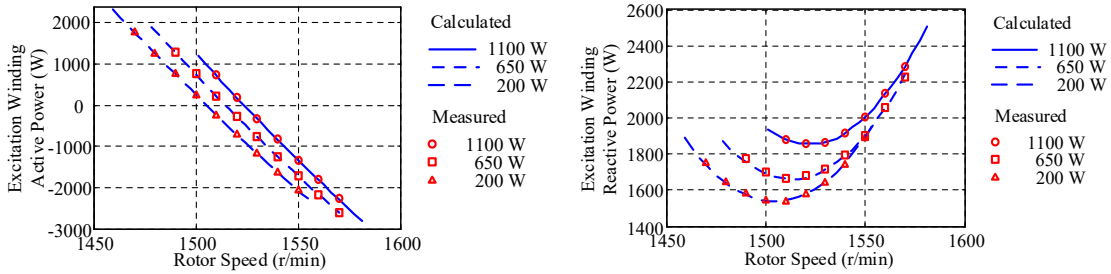

a *b*

Fig. 6.15 Variations of the active power (a) and reactive power (b) of the excitation winding with the rotor speed when different loads are connected

As shown in Fig. 6.15(a), the provided active power varies linearly with the changing rotor speeds. Moreover, it is clearly evident that there exists a unique rotor speed at which the excitation winding neither supplies nor absorbs active power but only provides excitation power to the generator. When the generator is operated above this speed, the summation of the load power and machine losses are less than the power provided by the prime mover, and excess power is absorbed by the excitation winding. In contrast, the excitation winding needs to supplement the prime mover to meet the load requirements when the generator is operated below this speed. In addition, it is interesting to note that this unique rotor speed increases with the increase in the load. As shown in Fig. 6.15(b), the reactive power provided by the excitation

winding is observed to increase with increasing load and the minimum reactive power requirements are achieved at a speed slightly higher than the synchronous speed for different loads.

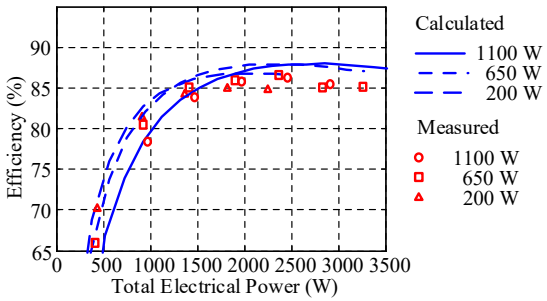

Fig. 6.16 Efficiency of the generator

The performance of the proposed generator was also evaluated by measuring the efficiency for a range of load and excitation power levels, as illustrated in Fig. 6.16. A maximum efficiency of approximately 87% is observed. Fig. 6.17 and Fig. 6.18, respectively, show the output voltage when the power winding is subjected to the load resistance increase and decrease. Fig. 6.17 illustrates the experimental waveform of the load voltage when the resistance load is increased from 100 Ohm to 200 Ohm at 0.6s, and Fig. 6.18 illustrates the experimental waveform of the load voltage when the resistance load is reduced from 200 Ohm to 100 Ohm at 0.6s. As shown in Fig. 6.17 and Fig. 6.18, the load voltage is well controlled by the proposed strategy with a short settling time.

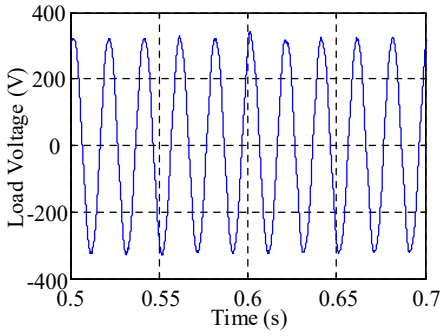

Fig. 6.17 Experimental waveform of the load voltage when the load is increased

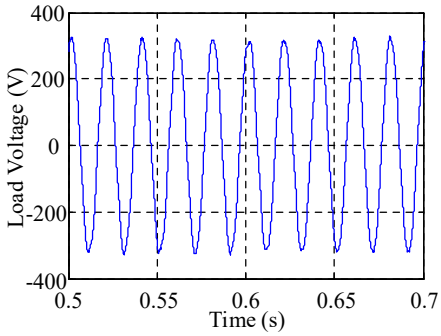

Fig. 6.18 Experimental waveform of the load voltage when the load is reduced

6.6. Summary

By connecting the neutral-point of the two series-connected winding of the TSCAOI configured generator to an additional converter leg, an improved TSCAOI winding configuration that enables the balanced operating condition, fast dynamic response and wider operating range has been proposed in this chapter. The mathematical model, which predicts its behaviour, has also been presented. With the help of this model, a novel direct-flux-controlled (DFC) scheme, which enables the control of generated voltage by directly regulating the stator flux, is proposed. The validity of the proposed concept of generation has been verified using simulations and experimental evidence of a prototype generator. Both simulations and measured results indicate that the technique is viable and allows for the variable-speed electricity generation at constant frequency while operating the cage induction machine under balanced conditions.

Chapter 7

Conclusions

This chapter includes concluding remarks and contributions made to the field of the TSCAOI configured generator from this thesis, and a discussion on possible directions for future research.

7.1. Conclusions

Due to depleting reserves, increasing costs and adverse environmental effects of fossil fuels, it has become a common practice within both academia and industry to focus more on renewable generation systems. Among these, the small scale single-phase renewable distributed generation system has drawn particular attention. Because, such a generation system is suitable to meet the electricity demand in rural and remote areas. However, these areas are normally located in the less-developed regions, thus become cost sensitive. In order to satisfy the requirements of both low system cost and high reliability, the low-cost and rugged 3-phase squirrel cage induction machine can be employed. Because the majority of electric loads in these areas are of single-phase nature, various techniques have been developed to use 3-phase squirrel cage induction machines for single-phase electricity generations, as detailed in Chapter 2.

As an alternative, a new winding configuration, using one of the stator phases of a 3-phase squirrel cage induction machine as the excitation winding and the remaining two phases connected in series as the power winding, has been proposed for using 3-phase squirrel cage induction machines to generate single-phase electricity, and named TSCAOI. With this simple configuration, a 3-phase squirrel cage induction machine can generate regulated single-phase electricity at constant frequency under varying rotor speeds. The aim of this thesis was to solve three major technical difficulties associated with the TSCAOI configured generator, as identified in Chapter 2.

In Chapter 3, a comprehensive equivalent circuit model was proposed to provide an insight into the steady-state behaviour of the standalone TSCAOI configured generator. Using

this model, the impacts of system parameters on its load and excitation characteristics, as well as on its level of unbalanced operation were identified. Furthermore, Chapter 3 presented a winding function approach to obtain the dynamic model of the TSCAOI configured generator, eliminating the previous reported cumbersome derivations. Chapter 4 investigated the steady-state behaviour of the standalone TSCAOI configured generator through simulations, implementing the proposed mathematical model in MATLAB/Simulink and experimentally using a prototype generator. Both the simulated and experimental results are in good agreement and exhibit same trend, further indicating that the characteristics of this particular generator can be accurately predicted by the proposed equivalent circuit models.

Chapter 5 investigated the steady-state behaviour of the grid-connected TSCAOI generator and proposed a look-up table based control scheme to operate the generator under given operating conditions. To simplify the implementation of the generator, Chapter 5 proposed a slip estimation method, enabling the speed-sensorless control of the generator. Finally, simulation and experimental results for a prototype generator were provided to validate the proposed concept and control scheme.

In Chapter 6, a modified winding configuration, named NPC-TSCAOI, was presented. By connecting the neutral-point of the two series-connected winding in the TSCAOI winding configuration to an additional converter leg, the balanced operation of the generator can be realized. The fundamental relationship between the stator flux linkage and the output voltage was investigated for the standalone generator. Based on this relationship, a direct-flux-controlled (DFC) scheme, which enables balanced operation of the generator with fast transient response, was accordingly proposed. The validity of the proposed generator concept was also verified through both simulations and experiments.

7.2. Contributions

The main contributions of this thesis are summarized as below

- Steady-state equivalent circuit models have been proposed for the standalone TSCAOI configured generator. With these models, the steady-state behaviour of the standalone TSCAOI configured generator was investigated, and the impacts of system parameters on the load and excitation characteristics of the generator, as well as on the level of its voltage unbalance, were identified.
- A control scheme has been proposed for the grid-connected TSCAOI configured generator. The control scheme incorporates a look-up table, enabling the

electricity generation at near-unity power factor and limiting the unbalanced operation of the generator. In addition, a slip estimation method, which enables speed-sensorless control of the generator, has also been proposed for simplifying the system.

- An NPC-TSCAOI winding configuration has been proposed based on the TSCAOI winding configuration. This new configuration allows the balanced operation of the generator. A mathematical model for the NPC-TSCAOI configured generator has been derived and a DFC scheme has been proposed to regulate the output voltage with fast transient response.

7.3. Future Work

This thesis has already identified the impacts of machine parameters on the load and excitation characteristics of the standalone TSCAOI configured generator, as well as on its level of unbalanced operation in Chapter 3. It is well known that the parameters of SCIM change significantly with many variables, such as power ratings, applications, materials, winding patterns and manufacture processes. For example, resistance and leakage reactance of both stator and rotor circuits are usually reduced with increasing of the power ratings. In addition, the rotor resistance of the line-fed SCIMs is generally higher than that of the inverter-fed SCIMs with same rated power. Because the line-fed SCIMs, which need a high self-starting torque, are normally designed with a double cage or deep rotor slots. However, the inverter-fed SCIMs, which no longer need the self-starting torque, normally adopt shallow and wide rotor slots, leading to a lower rotor resistance. Therefore, the next area of research could involve the dedicated comparison and selection among different off-the-shelf SCIMs for the standalone TSCAOI configured generator, using analytical equations derived in Chapter 3. Furthermore, an optimized design of the SCIM for the standalone TSCAOI configured generator could also be performed, based on the known influences of machine parameters on its behaviour.

Chapter 6 proposed a topological modification to the TSCAOI winding configuration. The modified winding configuration, named as NPC-TSCAOI, provides an additional control degree of freedom, thus enabling the vector control of the generator. There are two major strategies for the vector control of the generator, namely direct flux control (DFC) and field oriented control (FOC). These two strategies are different in the control principle but identical in nature. In Chapter 6, the direct flux controlled scheme was proposed for the NPC-TSCAOI configured generator. With this control scheme, the generator can provide well-regulated

output voltage at varying rotor speeds under the balanced operation condition. Another area of research therefore could be to implement the field oriented controlled scheme for the NPC-TSCAOI configured generator. The field oriented controlled scheme is expected to be more complex than the direct flux controlled scheme, but it would offer superior performance with reduced the torque ripple and DC-link voltage.

Appendix A

Parameters of the prototype generator

Prototype: A squirrel cage 3-kW TECO four-pole 400-V/50-Hz induction machine, which has the following parameters:

$$R_s = 1.5\Omega$$
$$R_r = 2\Omega$$
$$L_{1s} = 0.011\ \text{H}$$
$$L_{1r} = 0.011\ \text{H}$$
$$L_M = 0.214\ \text{H}$$
$$J = 0.01\ \text{kg} \cdot \text{m}^2$$

References

[1] H. Boogaard, K. Walker, and A. J. Cohen, "Air pollution: the emergence of a major global health risk factor," *International health,* vol. 11, pp. 417-421, 2019.

[2] J. Lelieveld, K. Klingmüller, A. Pozzer, R. Burnett, A. Haines, and V. Ramanathan, "Effects of fossil fuel and total anthropogenic emission removal on public health and climate," *Proceedings of the National Academy of Sciences,* vol. 116, pp. 7192-7197, 2019.

[3] T. Adefarati and R. Bansal, "Integration of renewable distributed generators into the distribution system: a review," *IET Renewable Power Generation,* vol. 10, pp. 873-884, 2016.

[4] A. M. Bouzid, J. M. Guerrero, A. Cheriti, M. Bouhamida, P. Sicard, and M. Benghanem, "A survey on control of electric power distributed generation systems for microgrid applications," *Renewable and Sustainable Energy Reviews,* vol. 44, pp. 751-766, 2015.

[5] REN21, "Renewables 2019: Global status report," *REN21 Secretariat,* 2019.

[6] A. Chatterjee and D. Chatterjee, "An improved excitation control technique of three-phase induction machine operating as dual winding generator for micro-wind domestic application," *Energ. Convers. Manage,* vol. 98, pp. 98-106, 2015.

[7] A. Chatterjee and D. Chatterjee, "Analysis and control of photovoltaic-assisted three-phase induction machine operating as single-phase micro-wind generator," *IET Generation, Transmission & Distribution,* vol. 10, pp. 2165-2176, 2016.

[8] U. K. Madawala, T. Geyer, J. B. Bradshaw, and D. M. Vilathgamuwa, "Modeling and Analysis of a Novel Variable-Speed Cage Induction Generator," *IEEE Trans. Ind. Electron.,* vol. 59, pp. 1020-1028, 2012.

[9] J. Soltani and N. R. Abjadi, "A Novel Stand-Alone Single-Phase Induction Generator Using a Three-Phase Machine and a Single-Phase PWM Inverter," *INTERNATIONAL JOURNAL OF ENGINEERING TRANSACTIONS* vol. A, pp. 259-268, 2003.

[10] Z. Wang, U. K. Madawala, T. H. Liu, and D. J. Thrimawithana, "Steady-state characteristis of 3-phase cage induction generators in TSCAOI configuration," in *2015 IEEE 2nd International Future Energy Electronics Conference (IFEEC)*, 2015, pp. 1-6.

[11] N. Orlando, M. Liserre, V. Monopoli, R. Mastromauro, and A. Dell'Aquila, "Comparison of power converter topologies for permanent magnet small wind turbine system," in *2008 IEEE International Symposium on Industrial Electronics*, 2008, pp. 2359-2364.

[12] N. A. Orlando, M. Liserre, R. A. Mastromauro, and A. Dell'Aquila, "A survey of control issues in PMSG-based small wind-turbine systems," *IEEE transactions on Industrial Informatics,* vol. 9, pp. 1211-1221, 2013.

[13] N. Jiao, W. Liu, Z. Zhang, T. Meng, J. Peng, and Y. Jiang, "Field Current Estimation for Wound-Rotor Synchronous Starter–Generator With Asynchronous Brushless Exciters," *IEEE Transactions on Energy Conversion,* vol. 32, pp. 1554-1561, 2017.

[14] J. Pang, W. Liu, N. Jiao, J. Wang, and P. Ma, "Calculation of Cross-Coupling Inductance and Electromagnetic Torque in Wound-Rotor Synchronous Starter/Generator," *IEEE Transactions on Industrial Electronics,* vol. 66, pp. 5115-5123, 2019.

[15] R. S. Munoz-Aguilar, A. Doria-Cerezo, E. Fossas, and R. Cardoner, "Sliding Mode Control of a Stand-Alone Wound Rotor Synchronous Generator," *IEEE Transactions on Industrial Electronics,* vol. 58, pp. 4888-4897, 2011.
[16] K. Protsenko and D. Xu, "Modeling and Control of Brushless Doubly-Fed Induction Generators in Wind Energy Applications," *IEEE Transactions on Power Electronics,* vol. 23, pp. 1191-1197, 2008.
[17] S. Shao, E. Abdi, F. Barati, and R. McMahon, "Stator-Flux-Oriented Vector Control for Brushless Doubly Fed Induction Generator," *IEEE Transactions on Industrial Electronics,* vol. 56, pp. 4220-4228, 2009.
[18] H. Gorginpour, H. Oraee, and R. A. McMahon, "A Novel Modeling Approach for Design Studies of Brushless Doubly Fed Induction Generator Based on Magnetic Equivalent Circuit," *IEEE Transactions on Energy Conversion,* vol. 28, pp. 902-912, 2013.
[19] M. Chunting, M. Filippa, J. Shen, and N. Natarajan, "Modeling and control of a variable-speed constant-frequency synchronous generator with brushless exciter," *IEEE Transactions on Industry Applications,* vol. 40, pp. 565-573, 2004.
[20] S. Nadarajan, S. K. Panda, B. Bhangu, and A. K. Gupta, "Hybrid Model for Wound-Rotor Synchronous Generator to Detect and Diagnose Turn-to-Turn Short-Circuit Fault in Stator Windings," *IEEE Transactions on Industrial Electronics,* vol. 62, pp. 1888-1900, 2015.
[21] J. A. Baroudi, V. Dinavahi, and A. M. Knight, "A review of power converter topologies for wind generators," *Renewable energy,* vol. 32, pp. 2369-2385, 2007.
[22] V. Yaramasu, A. Dekka, M. J. Durán, S. Kouro, and B. Wu, "PMSG-based wind energy conversion systems: survey on power converters and controls," *IET Electric Power Applications,* vol. 11, pp. 956-968, 2017.
[23] S. Muller, M. Deicke, and R. W. De Doncker, "Doubly fed induction generator systems for wind turbines," *IEEE Industry applications magazine,* vol. 8, pp. 26-33, 2002.
[24] M. Tazil, V. Kumar, R. C. Bansal, S. Kong, Z. Y. Dong, W. Freitas*, et al.*, "Three-phase doubly fed induction generators: an overview," *IET Electric Power Applications,* vol. 4, pp. 75-89, 2010.
[25] T. Ackermann, G. Andersson, and L. Söder, "Distributed generation: a definition," *Electric power systems research,* vol. 57, pp. 195-204, 2001.
[26] G. Pepermans, J. Driesen, D. Haeseldonckx, R. Belmans, and W. D'haeseleer, "Distributed generation: definition, benefits and issues," *Energy policy,* vol. 33, pp. 787-798, 2005.
[27] W. El-Khattam and M. M. Salama, "Distributed generation technologies, definitions and benefits," *Electric power systems research,* vol. 71, pp. 119-128, 2004.
[28] R. C. Dugan and T. E. McDermott, "Distributed generation," *IEEE Industry Applications Magazine,* vol. 8, pp. 19-25, 2002.
[29] B. Chalmers and E. Spooner, "An axial-flux permanent-magnet generator for a gearless wind energy system," *IEEE Transactions on Energy Conversion,* vol. 14, pp. 251-257, 1999.
[30] W. Rong-Jie, M. J. Kamper, K. V. d. Westhuizen, and J. F. Gieras, "Optimal design of a coreless stator axial flux permanent-magnet generator," *IEEE Transactions on Magnetics,* vol. 41, pp. 55-64, 2005.
[31] S. M. Hosseini, M. Agha-Mirsalim, and M. Mirzaei, "Design, Prototyping, and Analysis of a Low Cost Axial-Flux Coreless Permanent-Magnet Generator," *IEEE Transactions on Magnetics,* vol. 44, pp. 75-80, 2008.

[32] J. Bumby and R. Martin, "Axial-flux permanent-magnet air-cored generator for small-scale wind turbines," *IEE Proceedings-Electric Power Applications,* vol. 152, pp. 1065-1075, 2005.
[33] M. Polikarpova, P. Ponomarev, P. Röyttä, S. Semken, Y. Alexandrova, and J. Pyrhönen, "Direct liquid cooling for an outer-rotor direct-drive permanent-magnet synchronous generator for wind farm applications," *IET Electric Power Applications,* vol. 9, pp. 523-532, 2015.
[34] A. A. Pop, F. Jurca, C. Oprea, M. Chirca, S. Breban, and M. M. Radulescu, "Axial-flux vs. radial-flux permanent-magnet synchronous generators for micro-wind turbine application," in *2013 15th European Conference on Power Electronics and Applications (EPE)*, 2013, pp. 1-10.
[35] M. G. Simoes and F. A. Farret, *Renewable energy systems: design and analysis with induction generators*: CRC press, 2004.
[36] I. Boldea, *Variable speed generators*: CRC press, 2018.
[37] Y. K. Chauhan, S. K. Jain, and B. Singh, "A Prospective on Voltage Regulation of Self-Excited Induction Generators for Industry Applications," *IEEE Transactions on Industry Applications,* vol. 46, pp. 720-730, 2010.
[38] B. Singh, M. Singh, and A. K. Tandon, "Transient Performance of Series-Compensated Three-Phase Self-Excited Induction Generator Feeding Dynamic Loads," *IEEE Transactions on Industry Applications,* vol. 46, pp. 1271-1280, 2010.
[39] H. Geng, D. Xu, B. Wu, and W. Huang, "Direct Voltage Control for a Stand-Alone Wind-Driven Self-Excited Induction Generator With Improved Power Quality," *IEEE Transactions on Power Electronics,* vol. 26, pp. 2358-2368, 2011.
[40] R. Karthigaivel, N. Kumaresan, and M. Subbiah, "Analysis and control of self-excited induction generator-converter systems for battery charging applications," *IET Electric Power Applications,* vol. 5, pp. 247-257, 2011.
[41] C. Wagner, "Self-excitation of induction motors," *Electrical Engineering,* vol. 58, pp. 47-51, 1939.
[42] G. K. Kasal and B. Singh, "Decoupled voltage and frequency controller for isolated asynchronous generators feeding three-phase four-wire loads," *IEEE Transactions on power delivery,* vol. 23, pp. 966-973, 2008.
[43] W.-L. Chen, Y.-H. Lin, H.-S. Gau, and C.-H. Yu, "STATCOM controls for a self-excited induction generator feeding random loads," *IEEE transactions on power delivery,* vol. 23, pp. 2207-2215, 2008.
[44] B. Singh, S. S. Murthy, and S. Gupta, "STATCOM-based voltage regulator for self-excited induction generator feeding nonlinear loads," *IEEE transactions on industrial electronics,* vol. 53, pp. 1437-1452, 2006.
[45] S.-C. Kuo and L. Wang, "Analysis of voltage control for a self-excited induction generator using a current-controlled voltage source inverter (CC-VSI)," *IEE Proceedings-Generation, Transmission and Distribution,* vol. 148, pp. 431-438, 2001.
[46] I. Tamrakar, L. Shilpakar, B. Fernandes, and R. Nilsen, "Voltage and frequency control of parallel operated synchronous generator and induction generator with STATCOM in micro hydro scheme," *IET Generation, Transmission & Distribution,* vol. 1, pp. 743-750, 2007.
[47] T. Chan, K. Nigim, and L. Lai, "Voltage and frequency control of self-excited slip-ring induction generators," *IEEE Transactions on Energy Conversion,* vol. 19, pp. 81-87, 2004.
[48] E. G. Marra and J. A. Pomilio, "Induction-generator-based system providing regulated voltage with constant frequency," *IEEE Transactions on Industrial Electronics,* vol. 47, pp. 908-914, 2000.

[49] E. G. Marra and J. A. Pomilio, "Self-excited induction generator controlled by a VS-PWM bidirectional converter for rural applications," *IEEE Transactions on industry applications,* vol. 35, pp. 877-883, 1999.
[50] E. Suarez and G. Bortolotto, "Voltage-frequency control of a self-excited induction generator," *IEEE Transactions on Energy Conversion,* vol. 14, pp. 394-401, 1999.
[51] L. Shilpakar, "Analysis of a novel solid state voltage regulator for a self-excited induction generator," *IEE Proceedings-Generation, Transmission and Distribution,* vol. 145, pp. 647-655, 1998.
[52] M. B. Brennen and A. Abbondanti, "Static exciters for induction generators," *IEEE Transactions on Industry Applications,* pp. 422-428, 1977.
[53] B. Singh, S. Murthy, and S. Gupta, "Analysis and implementation of an electronic load controller for a self-excited induction generator," *IEE Proceedings-Generation, Transmission and Distribution,* vol. 151, pp. 51-60, 2004.
[54] D. Henderson, "An advanced electronic load governor for control of micro hydroelectric generation," *IEEE Transactions on Energy Conversion,* vol. 13, pp. 300-304, 1998.
[55] R. Bonert and S. Rajakaruna, "Self-excited induction generator with excellent voltage and frequency control," *IEE Proceedings-Generation, Transmission and Distribution,* vol. 145, pp. 33-39, 1998.
[56] R. Bonert and G. Hoops, "Stand alone induction generator with terminal impedance controller and no turbine controls," *IEEE Transactions on Energy Conversion,* vol. 5, pp. 28-31, 1990.
[57] M. El-Sharkawi, S. Venkata, T. Williams, and N. Butler, "An adaptive power factor controller for three-phase induction generators," *IEEE Transactions on Power Apparatus and systems,* pp. 1825-1831, 1985.
[58] S. S. Murthy, O. P. Malik, and A. K. Tandon, "Analysis of self-excited induction generators," *IEE Proceedings C - Generation, Transmission and Distribution,* vol. 129, pp. 260-265, 1982.
[59] N. H. Malik and S. E. Haque, "Steady-State Analysis and Performance of an Isolated Self-Excited Induction Generator," *IEEE Power Engineering Review,* vol. PER-6, pp. 38-38, 1986.
[60] T. F. Chan, "Steady-state analysis of self-excited induction generators," *IEEE Transactions on Energy Conversion,* vol. 9, pp. 288-296, 1994.
[61] A. K. A. Jabri and A. I. Alolah, "Capacitance requirement for isolated self-excited induction generator," *IEE Proceedings B - Electric Power Applications,* vol. 137, pp. 154-159, 1990.
[62] L. Ouazenne and G. McPherson, "Analysis of the Isolated Induction Generator," *IEEE Power Engineering Review,* vol. PER-3, pp. 59-59, 1983.
[63] T. F. Chan, "Analysis of self-excited induction generators using an iterative method," *IEEE Transactions on Energy Conversion,* vol. 10, pp. 502-507, 1995.
[64] W. Li and D. Ruey-Yong, "Transient performance of an isolated induction generator under unbalanced excitation capacitors," *IEEE Transactions on Energy Conversion,* vol. 14, pp. 887-893, 1999.
[65] L. S. Singh, CS Jha, Bhim, "Transient analysis of self-excited induction generator supplying dynamic load," *Electric Machines &Power Systems,* vol. 27, pp. 941-954, 1999.
[66] S. K. Jain, J. D. Sharma, and S. P. Singh, "Transient performance of three-phase self-excited induction generator during balanced and unbalanced faults," *IEE Proceedings - Generation, Transmission and Distribution,* vol. 149, pp. 50-57, 2002.

[67] A. Al Jabri and A. Alolah, "Capacitance requirement for isolated self-exicted induction generator," in *IEE Proceedings B (Electric Power Applications)*, 1990, pp. 154-159.
[68] N. H. Malik and A. A. Mazi, "Capacitance Requirements for Isolated Self Excited Induction Generators," *IEEE Transactions on Energy Conversion,* vol. EC-2, pp. 62-69, 1987.
[69] T. F. Chan, "Capacitance requirements of self-excited induction generators," *IEEE Transactions on Energy Conversion,* vol. 8, pp. 304-311, 1993.
[70] T. F. Chan, "Self-excited induction generators driven by regulated and unregulated turbines," *IEEE Transactions on Energy Conversion,* vol. 11, pp. 338-343, 1996.
[71] S. M. Alghuwainem, "Steady-state analysis of an isolated self-excited induction generator driven by regulated and unregulated turbine," *IEEE Transactions on Energy Conversion,* vol. 14, pp. 718-723, 1999.
[72] Y. H. A. Rahim, A. I. Alolah, and R. I. Al-Mudaiheem, "Performance of single phase induction generators," *IEEE Trans. Energy Convers.,* vol. 8, pp. 389-395, 1993.
[73] S. S. Murthy, "A novel self-induced self-regulated single phase induction generator. I. Basic system and theory," *IEEE Trans. Energy Convers.,* vol. 8, pp. 377-382, 1993.
[74] T. F. Chan, "Performance analysis of a three-phase induction generator connected to a single-phase power system," *IEEE Trans. Energy Convers.,* vol. 13, pp. 205-213, 1998.
[75] S. N. Mahato, S. P. Singh, and M. P. Sharma, "Capacitors Required for Maximum Power of a Self-Excited Single-Phase Induction Generator Using a Three-Phase Machine," *IEEE Trans. Energy Convers.,* vol. 23, pp. 372-381, 2008.
[76] L. L. Lai and T. F. Chan, *Distributed generation: Induction and permanent magnet generators*: John Wiley & Sons, 2008.
[77] M. O. Durham and R. Ramakumar, "Power system balancers for an induction generator," *IEEE transactions on industry applications,* pp. 1067-1072, 1987.
[78] O. J. Smith, "Three-phase induction generator for single-phase line," *IEEE transactions on energy conversion,* pp. 382-387, 1987.
[79] T. F. Chan and L. L. Lai, "Single-Phase Operation of a Three-Phase Induction Generator with the Smith Connection," *IEEE Power Engineering Review,* vol. 22, pp. 58-58, 2002.
[80] T. F. Chan and L. L. Lai, "A novel excitation scheme for a stand-alone three-phase induction generator supplying single-phase loads," *IEEE Trans. Energy Convers.,* vol. 19, pp. 136-143, 2004.
[81] T. F. Chan, L. L. Lai, and L. T. Yan, "A coupled circuit and field analysis of a three-phase induction motor with the Smith connection," *IEEE Trans. Magn.,* vol. 42, pp. 1315-1318, 2006.
[82] T. F. Chan, "Performance analysis of a three-phase induction generator self-excited with a single capacitance," *IEEE Transactions on Energy Conversion,* vol. 14, pp. 894-900, 1999.
[83] T. F. Chan and L. Loi Lei, "A novel single-phase self-regulated self-excited induction generator using a three-phase machine," *IEEE Transactions on Energy Conversion,* vol. 16, pp. 204-208, 2001.
[84] W. Li and D. Ruey-Yong, "A novel analysis of an autonomous three-phase delta-connected induction generator with one capacitor," in *2006 IEEE Power Engineering Society General Meeting*, 2006, p. 6 pp.
[85] T. Fukami, Y. Kaburaki, S. Kawahara, and T. Miyamoto, "Performance analysis of a self-regulated self-excited single-phase induction generator using a three-phase machine," *IEEE Trans. Energy Convers.,* vol. 14, pp. 622-627, 1999.
[86] S. N. Mahato, S. P. Singh, and M. P. Sharma, "Dynamic behavior of a single-phase self-excited induction generator using a three-phase machine feeding single-phase

dynamic load," *International Journal of Electrical Power & Energy Systems,* vol. 47, pp. 1-12, 2013/05/01/ 2013.

[87] T. F. Chan and L. L. Lai, "Single-phase operation of a three-phase induction generator using a novel line current injection method," *IEEE Transactions on Energy Conversion,* vol. 20, pp. 308-315, 2005.

[88] S. S. Murthy, B. Singh, S. Gupta, and B. M. Gulati, "General steady-state analysis of three-phase self-excited induction generator feeding three-phase unbalanced load/single-phase load for stand-alone applications," *IEE Proceedings - Generation, Transmission and Distribution,* vol. 150, pp. 49-55, 2003.

[89] T. F. Chan and L. Loi Lei, "Capacitance requirements of a three-phase induction generator self-excited with a single capacitance and supplying a single-phase load," *IEEE Trans. Energy Convers.,* vol. 17, pp. 90-94, 2002.

[90] O. Ojo, "Performance of self-excited single-phase induction generators with shunt, short-shunt and long-shunt excitation connections," *IEEE Trans. Energy Convers.,* vol. 11, pp. 477-482, 1996.

[91] E. Muljadi and T. A. Lipo, "Series compensated PWM inverter with battery supply applied to an isolated induction generator," *IEEE Trans. Ind. Appl.,* vol. 30, pp. 1073-1082, 1994.

[92] I. Boldea and S. A. Nasar, *The Induction Machine Handbook*. Boca Raton: FL: CRC Press, 2002.

[93] S. P. Singh, B. Singh, and M. P. Jain, "Performance characteristics and optimum utilization of a cage machine as capacitance excited induction generator," *IEEE Trans. Energy Convers.,* vol. 5, pp. 679-685, 1990.

[94] T. F. Chan and L. L. Lai, "Phase balancing for a self-excited induction generator," in *DRPT2000. International Conference on Electric Utility Deregulation and Restructuring and Power Technologies. Proceedings (Cat. No.00EX382)*, 2000, pp. 602-607.

[95] T. F. Chan and L. Loi Lei, "Steady-state analysis and performance of a stand-alone three-phase induction generator with asymmetrically connected load impedances and excitation capacitances," *IEEE Transactions on Energy Conversion,* vol. 16, pp. 327-333, 2001.

[96] M. G. Simoes, B. K. Bose, and R. J. Spiegel, "Design and performance evaluation of a fuzzy-logic-based variable-speed wind generation system," *IEEE Trans. Ind. Appl.,* vol. 33, pp. 956-965, 1997.

[97] B. K. Bose, "Energy, environment, and advances in power electronics," in *Industrial Electronics, 2000. ISIE 2000. Proceedings of the 2000 IEEE International Symposium on*, 2000, pp. TU1-T14 vol.1.

[98] R. Bojoi, D. Roiu, G. Griva, and A. Tenconi, "Single-phase grid-connected distributed generation system with Maximum Power Tracking," in *2010 12th International Conference on Optimization of Electrical and Electronic Equipment*, 2010, pp. 1131-1137.

[99] C. P. Ion and C. Marinescu, "Stand-alone micro-hydro power plant with induction generator supplying single phase loads," *Journal of Renewable and Sustainable Energy* vol. 5, 2013.

[100] C. P. Ion, I. Serban, and C. Marinescu, "Single-phase operation of an autonomous three-phase induction generator using a VSI-DL control system," in *2008 11th International Conference on Optimization of Electrical and Electronic Equipment*, 2008, pp. 333-338.

[101] S. S. Murthy, Ramrathnam, M. S. L. Gayathri, K. Naidu, and U. Siva, "A Novel Digital Control Technique of Electronic Load Controller for SEIG Based Micro Hydel Power

Generation," in *2006 International Conference on Power Electronic, Drives and Energy Systems*, 2006, pp. 1-5.
[102] B. Singh, S. S. Murthy, and S. Gupta, "Analysis and design of electronic load controller for self-excited induction Generators," *IEEE Trans. Energy Convers.,* vol. 21, pp. 285-293, 2006.
[103] S. Gao, G. Bhuvaneswari, S. S. Murthy, and U. Kalla, "Efficient voltage regulation scheme for three-phase self-excited induction generator feeding single-phase load in remote locations," *IET Renewable Power Generation,* vol. 8, pp. 100-108, 2014.
[104] T. Fukami, M. Imamura, and T. Miyamoto, "A new self-regulated self-excited single-phase induction generator using a squirrel cage three-phase induction machine," *IEEJ Transactions on Industry Applications,* vol. 115, pp. 867-873, 1995.
[105] S. Mahato, M. Sharma, and S. Singh, "Determination of minimum and maximum capacitances of a self-regulated self-excited single-phase induction generator using a three-phase winding," in *2006 India International Conference on Power Electronics*, 2006, pp. 28-33.
[106] T. Fukami, Y. Kaburaki, S. Kawahara, and T. Miyamoto, "Performance analysis of a self-regulated self-excited single-phase induction generator using a three-phase machine," *IEEE Transactions on Energy Conversion,* vol. 14, pp. 622-627, 1999.
[107] T. Chan, "Performance analysis of a three-phase induction generator self-excited with a single capacitance," *IEEE transactions on energy conversion,* vol. 14, pp. 894-900, 1999.
[108] T. Chan and L. L. Lai, "Steady-state analysis and performance of a stand-alone three-phase induction generator with asymmetrically connected load impedances and excitation capacitances," *IEEE transactions on energy conversion,* vol. 16, pp. 327-333, 2001.
[109] A. Al-Bahrani and N. Malik, "Steady state analysis and performance characteristics of a three-phase induction generator self excited with a single capacitor," *IEEE transactions on energy conversion,* vol. 5, pp. 725-732, 1990.
[110] X. Wei and X. Wu, "No-Load Voltage Buildup of Three-Phase Induction Generator under Single-Phase Operation," in *2010 International Conference on E-Product E-Service and E-Entertainment*, 2010, pp. 1-4.
[111] N. Kumaresan, "Analysis and control of three-phase self-excited induction generators supplying single-phase AC and DC loads," *IEE Proceedings-Electric Power Applications,* vol. 152, pp. 739-747, 2005.
[112] T. Chan, "Performance analysis of a three-phase induction generator connected to a single-phase power system," *IEEE transactions on energy conversion,* vol. 13, pp. 205-213, 1998.
[113] T. Chan and L. L. Lai, "Single-phase operation of a three-phase induction generator with the Smith connection," *IEEE transactions on energy conversion,* vol. 17, pp. 47-54, 2002.
[114] L. Wang and R.-Y. Deng, "A novel analysis of an autonomous three-phase delta-connected induction generator with one capacitor," in *2006 IEEE Power Engineering Society General Meeting*, 2006, p. 6 pp.
[115] L. B. Shilpakar and B. Singh, "Dynamic behavior of a three-phase self-excited induction generator for single-phase power generation," *Electric Power Systems Research,* vol. 48, pp. 37-44, 1998/12/01/ 1998.
[116] T. Chan, L. Lai, and L.-T. Yan, "Finite element analysis of a single-phase grid-connected induction generator with the Steinmetz connection," *IEEE Transactions on Energy Conversion,* vol. 18, pp. 321-329, 2003.

[117] D. Lamabadu and S. Rajakaruna, "Dynamic Analysis of a Novel Single-Phase Induction Generator Using an Improved Machine Model," *IEEE Transactions on Energy Conversion,* vol. 32, pp. 1-11, 2017.
[118] D. Liyanage and S. Rajakaruna, "An improved dynamic model for a single-phase generator based on three-phase cage rotor induction machine," in *2015 IEEE 11th International Conference on Power Electronics and Drive Systems*, 2015, pp. 934-939.
[119] A. Chatterjee, K. Roy, and D. Chatterjee, "A Gravitational Search Algorithm (GSA) based Photo-Voltaic (PV) excitation control strategy for single phase operation of three phase wind-turbine coupled induction generator," *Energy,* vol. 74, pp. 707-718, 2014/09/01/ 2014.
[120] A. Chatterjee and D. Chatterjee, "An improved excitation control technique of three-phase induction machine operating as dual winding generator for micro-wind domestic application," *Energy Conversion and Management,* vol. 98, pp. 98-106, 2015/07/01/ 2015.
[121] A. Chatterjee and D. Chatterjee, "PV-assisted microgeneration scheme with single-phase induction generator suitable for wide speed range application," *IET Power Electronics,* vol. 10, pp. 1859-1869, 2017.
[122] N. L. Schmitz and D. W. Novotny, *Introductory Electromechanics*. New York, NY, USA: Ronald Press, 1965.
[123] O. Ojo, O. Omozusi, A. Ginart, and B. Gonoh, "The operation of a stand-alone, single-phase induction generator using a single-phase, pulse-width modulated inverter with a battery supply," *IEEE Trans. Energy Convers.,* vol. 14, pp. 526-531, 1999.
[124] O. Ojo, O. Omozusi, and A. A. Jimoh, "The operation of an inverter-assisted single-phase induction generator," *IEEE Trans. Ind. Electron.,* vol. 47, pp. 632-640, 2000.
[125] M. Myers, M. Bodson, and F. Khan, "Design of Drives for Inverter-Assisted Induction Generators," *IEEE Trans. Ind. Appl.,* vol. 48, pp. 2147-2156, 2012.
[126] O. Ojo and B. Gonoh, "A controlled stand-alone single-phase induction generator," in *Proceedings of International Conference on Power Electronics, Drives and Energy Systems for Industrial Growth*, 1996, pp. 694-699 vol.2.
[127] A. E. Fitzgerald, C. Kingsley, and S. D. Umans, *Electric machinery*, 6th ed ed. New York, NY, USA: McGraw-Hill, 2003.
[128] C. L. Fortescue, "Method of Symmetrical Co-Ordinates Applied to the Solution of Polyphase Networks," *Transactions of the American Institute of Electrical Engineers,* vol. XXXVII, pp. 1027-1140, 1918.
[129] Z. Wang, U. K. Madawala, T. H. Liu, D. M. Vilathgamuwa, and D. J. Thrimawithana, "Torque characteristics of TSCAOI configured induction generators," in *2016 IEEE 2nd Annual Southern Power Electronics Conference (SPEC)*, 2016, pp. 1-6.
[130] D. W. Novotny and T. A. Lipo, "Vector Control and Dynamics of AC Drives," *Oxford, U.K.: Clarendon,* 1996.